Fall 10-13-2017

SURFACES AND INTERFACES OF MAGNETOELECTRIC OXIDE SYSTEMS

Shi Cao
University of Nebraska - Lincoln, shi.cao@huskers.unl.edu

SURFACES AND INTERFACES OF MAGNETOELECTRIC OXIDE SYSTEMS

by

Shi Cao

A DISSERTATION

Presented to the Faculty of

The Graduate College at the University of Nebraska

In Partial Fulfilment of Requirements

For the Degree of Doctor of Philosophy

Major: Physics and Astronomy

Under the Supervision of Peter A. Dowben

Lincoln, Nebraska

December, 2017

SURFACES AND INTERFACES OF MAGNETOELECTRIC OXIDE SYSTEMS

Shi Cao, Ph.D.

University of Nebraska, 2017

Adviser: Peter A. Dowben

Magnetoelectric materials Cr_2O_3, hexagonal $LuFeO_3$ and $YbFeO_3$ are studied in this thesis. The surface of chromia (Cr_2O_3) has a surface electronic structure distinct from the bulk. Our work shows that placing a Cr_2O_3 single crystal into a single domain state will result in net Cr_2O_3 spin polarization at the boundary, even in the presence of a gold overlayer. From the Cr $2p_{3/2}$ X-ray magnetic circular dichroism signal, there is clear evidence of interface polarization with overlayers of both Pd and Pt on chromia. Cobalt thin films on $Cr_2O_3(0001)$ show larger magnetic contrast in magnetic force microscopy indicating enhancement of perpendicular anisotropy induced by Cr_2O_3.

The interfacial charge transfer between mechanically exfoliated few-layer graphene and $Cr_2O_3(0001)$ surfaces has been investigated showing hole doping of few-layer graphene. Density functional theory calculations furthermore confirm the p-type nature of the graphene on top of chromia, and suggest that the chromia is able to induce a significant carrier spin polarization in the graphene layer.

The surface termination and the nominal valence states for hexagonal $LuFeO_3$ thin films were characterized. The stable surface terminates in a $Fe-O$ layer. This is consistent with the results of density functional calculations. The structural transition at about 1000 °C, from the hexagonal to the orthorhombic phase of $LuFeO_3$, has been investigated in thin films of $LuFeO_3$. The electronic structure for the conduction bands of both hexagonal and orthorhombic $LuFeO_3$ thin films have been measured. Dramatic differences in both the spectral features and the linear dichroism are observed.

We have also studied the ferrimagnetism in h-$YbFeO_3$ by measuring the magnetization of Fe and Yb separately. The results directly show antialignment of magnetization of Yb and Fe ions in h-$YbFeO_3$ at low temperature, with an exchange field on Yb of about 17 kOe. All ferrimagnets, by default, are magnetoelectrics. These findings directly demonstrate that ferrimagnetic order exists in h-$YbFeO_3$.

ACKNOWLEDGMENTS

I am very grateful to my adviser Dr. Peter Dowben who has offered me tremendous support in pursuing my Ph.D. degree. Dr. Dowben's supervision and guidance have made the achievements in this thesis possible. If I divide my Ph.D. education into two aspects, the scientific aspect is what has been written down in this thesis and the human aspect is what is beyond that. In Dr. Dowben's research group, I had great opportunities to collaborate with excellent researchers around the world. I had the chance to visit different national laboratories and operate the delicate experimental apparatuses there. Dr. Dowben also encouraged me to present our work at different conferences. In the past few years, I had many chances to visit different cities around the world and talk to various scientists. I may or may not forget the scientific aspect but the human aspect, which impacts my mind and soul and broadens my horizons, will be with me forever.

I would like to give acknowledgment to Dr. Xiaoshan Xu and all his group members. The last half of my Ph.D. program was finished through collaboration with Dr. Xu. We measured data together at national laboratories several times. I have learned a lot from these experiences working with him. I am impressed and inspired by his expertise, diligence and tireless effort.

I wish to give acknowledgment to Dr. Christan Binek who is also my committee member and all his group members, especially Michael Street. I have learned a lot through collaboration with Dr. Binek's group, who provided many high quality samples and great support for me.

I am grateful that I obtained endless help from our former and current group members, especially Dr. Takashi Komesu and Dr. Ning Wu.

I wish to thank Dr. Jian Wang at the Canadian Light Source and Dr. Andreas Schmid and his group members at Lawrence Berkeley National Laboratory for offering me great

opportunities to work with them on-site and their help with collecting data.

I would like to give acknowledgment to Dr. Evgeny Tsymbal who is also my committee member and all his group members, especially Dr. Tula Paudel for their theoretical support. I wish to acknowledge Dr. Alexei Gruverman and Dr. Haidong Lu. I would like to give acknowledgment to the support from Dr. Xia Hong and Zhiyong Xiao. I also wish to acknowledge Dr. Axel Enders and all his group members.

I wish to acknowledge the support of all my collaborators for providing data, insightful discussions and other help. I also would like to thank all the colleagues, classmates and friends I met at Lincoln and at conferences.

I would like to thank Dr. Christan Binek, Dr. Li Tan and Dr. Evgeny Tsymbal for being my committee members as well as their suggestions and advice in this work.

I appreciate the policy of the graduate school of the University of Nebraska-Lincoln allowing students to participate in two graduate programs at the same time. When I started participating in a Master's program in Computer Science, I could still keep going towards completing this thesis.

There are so many people I have to express my gratitude to, and I may or may not mention all the names, but you all have my deepest appreciation.

Last but not least, I am grateful that I received unconditional support from my family, especially from my wife Zhuoying Xie, during these years. With their love, I will keep going forward.

Table of Contents **vi**

Chapter 1

Introduction

1.1 Magnetoelectric coupling and applications

Fundamental solid state and material research work changes the world profoundly through devices. The charge and spin of electrons are the keystones for applications in semiconductor or electronic devices. In this, condensed matter physicists and material scientists devote themselves to study and predict the behavior and properties of electrons in crystals, nanostructures, and so on. We would like to explore the potential of new magnetoelectric devices for spintronic applications. The key question in this regard is, ”Can we control the spin polarization by applying an electric field?”, which can be generalized as, ”Is there any magnetoelectric coupling in a material?”.

Fortunately, the electric charge and magnetic interacts. The magnetoelectric coupling may be expected in some crystals. As early as 1894, Pierre Curie predicted a magnetoelectric coupling based on a lattice symmetry argument. However, not until 1960, was the first real magnetoelectric material Cr_2O_3 demonstrated. Magnetoelectric materials were rare and the observed magnetoelectric perfomance was poor until 2003 when the room temperature multiferroicity was discoved in $BiFeO_3$ thin films [1].

The term multiferroic originally was used to define a material with both ferromagnetism and feroelectricity and nowadays extended to define the coexistence of any ferroicities.

It is intuitive that when the ferroelectric order and magnetic order coexist, there will be magnetoelectricity.

Unfortunately, in one material, the order parameters for ferroelectric and magnetic order are mutually exclusive [2]. Since the empty d shell in transition ions is the key for ferrolectric order but the magnetic order typically requires partially filled d shells. However, if the ferroelectric is from a structural transition, then the requirement of an empty d shell can be relaxed and multiferroicity may be expected in these materials [2].

In this thesis, we study the magnetoelectric Cr_2O_3 and multiferroic hexagonal $ReFeO_3$. Through these studies, we explore the magnetoelectric properties of these materials through the fundamental research on the surface and interface that might shed light on potential applications. "The interface is the device" as stated by the Nobel Prize winner Herb Kroemer [3].

1.2 Magnetoelectric Cr_2O_3

The surface of $Cr_2O_3(0001)$ (chromia) has recently drawn considerable attention because of the phenomenon of roughness insensitive boundary magnetization [4]. The boundary magnetization plays an important role in the development of isothermal voltage control of exchange bias in ferromagnetic-magnetoelectric heterostructures [4-7].

Because of potential applications in voltage controlled spintronics, perpendicular exchange-bias structures, based on the magnetoelectric $Cr_2O_3(0001)$, are more interesting. This interest in chromia is in part because of the higher Neel temperature of chromia than other magneto-electrics and in part because of the perpendicular magnetization and high boundary polarization of $Cr_2O_3(0001)$ surfaces. The boundary spin polarization at the surface of the magnetoelectric $Cr_2O_3(0001)$, can be isothermally voltage-controlled to provide perpendicular voltage-controlled exchange-bias in an adjacent ferromagnet [4-7]. This means that the adjacent ferromagnet is typically chosen with perpendicular magnetic anisotropy,

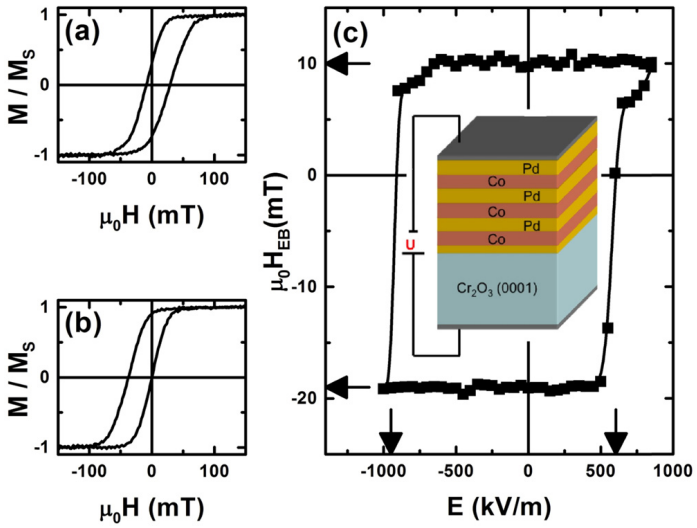

Figure 1.1: The hysteresis loop of pinned CoPd multilayer thin film on chromia (Cr_2O_3), as schematically shown in the insert, measured at T = 303 K (a) in the positive exchange bias saturation state and (b) the negative exchange bias saturation state. (c) Hysteretic behavior of equilibrium exchange bias measured after the system has been initialized by applying an electric field, E, and a constant magnetic field of 400 mT. Asymmetry relative to $H_{EB} = 0$ and $E = 0$ are indicated by horizontal and vertical arrows. Figure courtesy of William Echtenkamp of Dr. Christian Binek's group.

e.g. Co-Pd or Co-Pt multilayers. A typical hysteresis loop of Co-Pd multilayer on Cr_2O_3 are shown in figure 1.1

Boundary magnetization is a symmetry allowed roughness-insensitive equilibrium magnetic property of all magnetoelectric antiferromagnets [7-8]. While the high-level boundary spin polarization is roughness insensitive, questions remain as to the structural stability of the surface of magnetoelectric chromia. For example, depolarization due to thermal effects is more likely if the surface is soft, a tendency that could be exacerbated if the surface is rough and dominated by defects. A starting point to reconciling any controversy about the surface stability of $Cr_2O_3(0001)$ is to assess the surface density and surface Debye temperature, and, if either of these is unusually low, to look for a very heterogeneous surface, characterized by multiple chemical states. The surface stability of Cr_2O_3 will be introduced in section 3.1.

The exchange bias field, H_{EB}, in a bilayer of chromia and an adjacent exchange coupled ferromagnetic thin film (as seen in figure 1.1), observed after isothermal switching through

an applied electric field, E, in the simultaneous presence of a constant magnetic field, was found to differ in magnitude between the $Cr_2O_3(0001)$ single domain states of opposite surface/interface magnetization. In addition to asymmetry in the magnitude of the exchange bias field on switching, there is an asymmetry in the magnitude of the electric switching fields required to switch from positive to negative exchange bias and vice versa. Is there an asymmetry in the boundary spin polarization at the surface of chromia ? This issue of asymmetry in the boundary spin polarization may affect adlayers. In the latter case, the adlayers can be magnetic layers, such as cobalt, or non-magnetic layers, such as Cu, Au, Pt, Pd and even graphene. The studies of surface spin polarization asymmetry and the heterostructure consisting of metal adlayers and chromia are systematically discussed in Chapter 3.

Because of the boundary polarization, chromia is also a promising magnetoelectric dielectric gate substrate, and can be expected to give rise to induced spin polarization in any 2D narrow band materials on chromia. For this reason, the graphene/$Cr_2O_3(0001)$ system could offer a route to a nonvolatile magnetoelectric spin valve or spin FET. Effective spin polarized carrier injection into graphene is a challenging problem, and an alternative is the use a magnetic insulator substrate such as Cr_2O_3 that can induce spin polarization in the graphene. The study of graphene/$Cr_2O_3(0001)$ system will be introduced in section 3.3.1.

1.3 Multiferroic hexagonal $ReFeO_3$

$ReFeO_3$, where Re stands for rare-earth element, *i.e.* Re = Ho-Lu, Y and Sc, is a rare example of a material that exists in both orthorhombic and stabilized hexagonal structures [9-14], which are different both in the symmetry of the lattice and in the symmetry of the local environment of the metal (Fe and Re) sites (as shown in figures 1.2(a) and (b)). These differences in structure, give rise to the dramatic differences in properties such as ferroelectricity and magnetism [9-14].

Particularly interesting is the effect of the crystal structure on the magnetic structure, including the relative alignment between the spins and the preferred overall orientation of the spins (magnetocrystalline anisotropy). While the exchange interactions determine the relative alignment of the spins, their effect on the magnetocrystalline anisotropy is indirect, because the exchange interactions are isotropic. Single-ion magnetic anisotropy is a critical factor for the overall magnetocrystalline anisotropy, although the latter is also affected by the topological arrangements of the spins. The crystal structure, particularly the local environments of the magnetic ions, is expected to influence the single-ion magnetic anisotropy, by changing their orbital states and affecting spin orientations via the spin−orbit coupling. The crystal structure of $ReFeO_3$ motives the comprehensive studies of $LuFeO_3$ both in orthorhombic (o-$LuFeO_3$) and hexagonal (h-$LuFeO_3$) structures. We will introduce the surface stability of h-$LuFeO_3$ in section 4.1. The two phase coexistence will be introduced in section 4.3.

In hexagonal $ReFeO_3$ (h-$ReFeO_3$), the inversion symmetry of the lattice structure is broken by the rotation of the FeO_5 trigonal bipyramids, generating ferroelectricity below 1050 K (for h-$LuFeO_3$) with a polarization on the order of 10 μC cm^2 [11, 12, 15]. The spins on the Fe sites, in h-$LuFeO_3$, order in a 120-degree antiferromagnetic fashion in the $a-b$ plane (figure 1.2(a)); a canting of the spins out of the $a-b$ plane results in a weak ferromagnetism [9-11].

In orthorhombic $LuFeO_3$ (o-$LuFeO_3$), ferroelectricity is not expected due to the symmetric arrangement of the atoms. The spins on the Fe sites in o-$LuFeO_3$ order antiferromagnetically in a chain-like fashion in the $a-b$ plane below 620 K (figure 1(b)); a canting toward the c axis generates a weak ferromagnetism. The single-ion magnetic anisotropy is critical for the magnetic ordering in $LuFeO_3$. In o-$LuFeO_3$ the single-ion magnetic anisotropy is the prerequisite for the magnetocrystalline anisotropy; in h-$LuFeO_3$, the weak ferromagnetism is not allowed unless the spins are along the a axis [11, 12]. Therefore, elu-

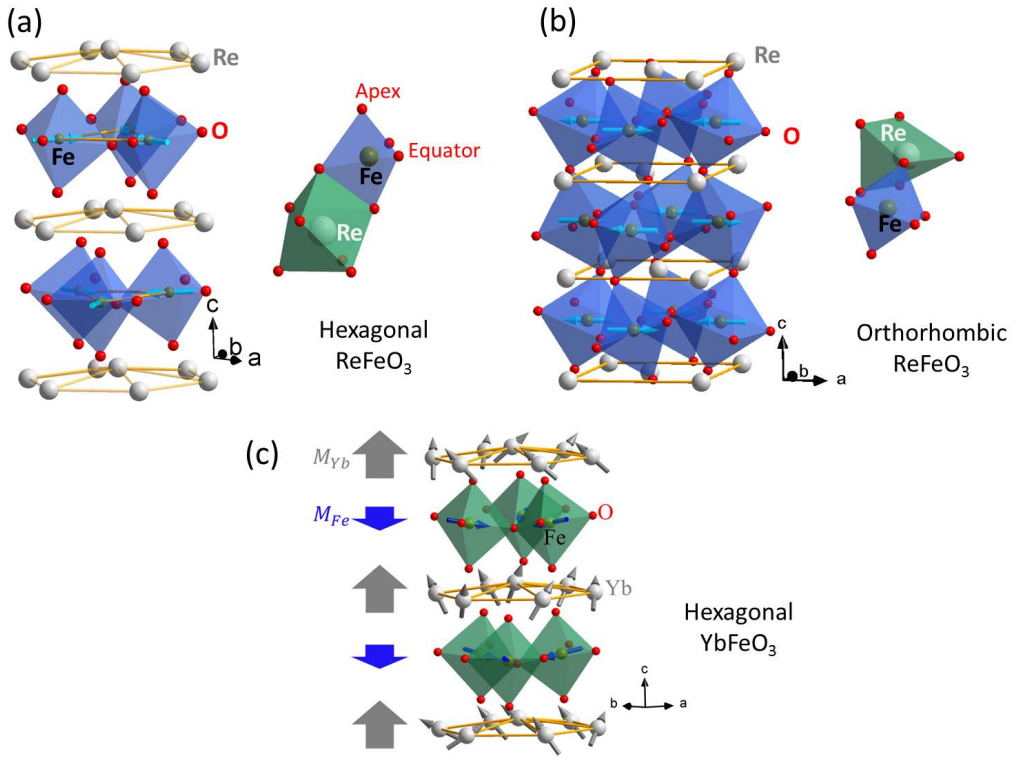

Figure 1.2: Lattice structures of hexagonal (a) and orthorhombic (b) $LuFeO_3$ as well as the local environments of the Lu and Fe sites. The thick arrows in (a) and (b) indicate the orientations of the spins. (c)The crystal structure of h-$YbFeO_3$ and a schematic of the magnetic structure. The arrows on the atoms indicate the atomic magnetic moments. M_{Fe} and M_{Yb} are the magnetization of Fe and Yb along the c axis, respectively, which are antialigned at low temperature. Figure courtesy of Dr. Xiaoshan Xu.

cidating the origin of the single-ion magnetic anisotropy is important to understanding and tuning the magnetism in $LuFeO_3$. This study will be discussed in section 4.2.

The diverse magnetic properties of rare-earth (RE) transition-metal (TM) oxides are due to the interplay between the distinct magnetism of rare-earth and transitionmetal ions. For the transition-metal ions, the magnetic moments come from 3d electrons, which are well exposed to the local environment. In contrast, for rare-earth ions, the major contribution for the magnetic moments often come from 4f electrons and provide significant contributions from both spin and orbital angular momentum. While stronger interactions between the transition-metal ions determines the framework of the magnetic order in RE-TM oxides [16-18], the weaker interaction between the rareearth and transition-metal ions,

on the other hand, generates interesting phenomena such as spin reorientation and moment compensation [19, 20]. Despite the importance of the RE-TM interactions, a comprehensive understanding of its underpinnings and implications is still lacking for many material systems.

Since in h-$LuFeO_3$, the 4f is fully occupied so Lu^{3+} is nonmagnetic. By way of comparison, we also studied hexagonal $YbFeO_3$, which is aslo a member of hexagonal rare-earth ferrites (h-$ReFeO_3$,Re = Ho-Lu,Y, and Sc). Hexagonal h-$YbFeO_3$ have a layered crystal structure in which both RE and Fe atoms adopt a two-dimensional triangular lattice, as shown in figure 1.2 (c).

The multiferroic properties of h-$YbFeO_3$ are from the same scenario of h-$LuFeO_3$. Below about 1000 K, the h-$YbFeO_3$ crystal structure undergoes a distortion, corresponding to a rotation of the FeO_5 local structure and a buckling of the rare-earth layer, which induces improper ferroelectricity. The rotation of FeO_5 also cants the moment on Fe, via the Dzyaloshinskii- Moriya interaction, generating weak ferromagnetism on top of a 120° antiferromagnetic order below about 120 K, as illustrated in figure 1.2. The spontaneous magnetization is along the *c* axis.

In h-$YbFeO_3$, the Fe-Fe interaction is expected to dominate the framework of themagnetic ordering, The Yb-Fe interaction is weaker but sufficient enough to partially align the moment on Yb and contribute to the total magnetization. It is an ideal system for us to study the magnetic interaction between rare-earth and transition-metal ions by measuring the magnetization of the rare-earth and transition-metal ions separately using an element-specific method. These studies are discussed in section 4.4.

References

[1] Dong S, Liu J M, Cheong S W and Ren Z 2015 *Adv. Phys.* **64** 519-626

[2] Cheong S W and Mostovoy M 2007 *Nature Mater.* **6** 13

[3] Kroemer H 2001 *Rev. Mod. Phys.* **73** 783

[4] He X, Wang Y, Wu N, Caruso A N, Vescovo E, Belashchenko K D, Dowben P A and Binek C 2010 *Nature Mater.* **9** 57985

[5] Wu N, He X, Wysocki A, Lanke U, Komesu T, Belashchenko K D, Binek C and Dowben P A 2011 *Phys. Rev. Lett.* **106** 087202

[6] Echtenkamp W and Binek C 2013 *Phys. Rev. Lett.* **111** 187204

[7] Belashchenko K D 2010 *Phys. Rev. Lett.* **105** 147204

[8] Andreev A F 1996 *JETP Lett.* **63** 758

[9] Akbashev A R, Semisalova A S, Perov N S and Kaul A R 2011 *Appl. Phys. Lett.* **99** 122502

[10] Moyer J A, Misra R, Mundy J A, Brooks C M, Heron J T, Muller D A, Schlom D G and Schiffer P 2014 *Appl. Phys. Lett. Mater.* **2** 012106

[11] Wang W, Zhao J, Wang W, Gai Z, Balke N, Chi M, Lee H N, Tian W, Zhu L, Cheng X, Keavney D J, Yi J, Ward T Z, Snijders P C, Christen H M, Wu W, Shen J and Xu X 2013 *Phys. Rev. Lett.* **110** 237601

[12] Xu X and Wang W B 2014 *Mod. Phys. Lett.* **B** 28 1430008

[13] Wang W B et al 2012 *Appl. Phys. Lett.* **101** 241907

[14] Das H, Wysocki A L, Geng Y N, Wu W D and Fennie C J 2014 *Nature Commun.* **5** 2998

[15] Wang H W, Solovyev I V., Wang W, Wang X, Ryan P J, Keavney D J, Kim J-W, Ward T Z, Zhu L, Shen J, Cheng X M, He L, Xu X and Wu X 2014 *Phys. Rev. B* **90** 014436

[16] Bozorth R M 1958 *Phys. Rev. Lett.* **1** 362

[17] Treves D 1965 *J. Appl. Phys.* **36** 1033-1039

[18] Treves D 1962 *Phys. Rev.* **125** 18431853

[19] Fabreges X, Petit S, Mirebeau I, Pailhes S, Pinsard L, Forget A, Fernandez-Diaz M T and Porcher F 2009 *Phys. Rev. Lett.* **103** 67204

[20] Vajk O P, Kenzelmann M, Lynn J W, Kim S B and Cheong S-W 2005 *Phys. Rev. Lett.* **94** 87601

Chapter 2

Experimental Techniques

In this chapter, some surface science experimental techniques are briefly reviewed. These techniques mainly focus on probing the electron states that influences the properties of the materials of interest. The electrons generated from a photoemission process are referred as photoelectrons [1]. Those electrons, described by a perturbation Hamiltonian, contain a lot of information about the initial state. From the study of the photoelectrons, the band structure information of a solid material can be obtained.

On the other hand, the reflected and diffracted electrons from a crystal surface contains surface information for a crystal. The diffracted electron contains the information of a crystal structure. Both the band structure and diffraction patterns study the reciprocal space of a crystal, however, the real space morphology can also be studied if the electrons are used to form an image through an electron microscope. If the incoming electrons are spin polarized, the surface magnetic properties can be obtained.

A challenge, and sometimes an advantage in exploiting photoelectron or diffracted electrons is from the short mean free path of electrons. This means the surface must be kept pristine. As a result, the ultra high vacuum (UHV) ($< 10^{-10}$ Torr is prefered) is necessary to conduct the research. In the following sections, the X-ray photoelectron spectroscopy (XPS), X-ray absorption spectroscopy (XAS) and low energy electron diffraction (LEED) are introduced. The electron imaging from electron microscope know as photoemission

electron (PEEM) or low energy electron microscopy (LEEM) is also reviewed.

2.1 X-ray photoelectron spectroscopy (XPS)

2.1.1 X-ray photoelectron spectroscopy (XPS) and angle-resolved X-ray photoelectron spectroscopy (ARXPS)

X-ray photoelectron spectroscopy (XPS) is based upon the photoelectric effect. The binding energy can be determined by the XPS process through the following equation [1]:

$$E_B = h\nu - E_{Kin} - \phi \tag{2.1}$$

where $h\nu$ is monochromatized light of energy, ϕ is work function which is the energy to release the electron from the solid. E_{Kin} is the outgoing electron kinetic energy which is usually measure by a hemi-sphere energy analyzer. Since the X-ray photon energy is high, XPS leads to ionization of core level electrons. As a result, XPS is often used as a chemical analysis technique since the elemental specified information and the chemical states such as the valence states can be obtained by XPS, due to the fact that the binding energy changes with the valence state [1]. In general, higher binding energy of an element is corresponding to a higher valence state. XPS is sensitive to the change of binding energy, therefore the surface-to-bulk shift can also be detected [1].

When the photoemission take-off angle varies, the effective penetration depth also changes. The intensities of XPS from distinct elements at different depth with respect to surface vary with the take-off angle. By making use of this fact, the angle-resolved XPS, known as ARXPS can be used to estimate the surface composition of complex compounds. The effective penetration depth is correlated to the electron mean free path λ in the following equation:

$$\lambda_{eff} = \lambda * cos(\theta) \tag{2.2}$$

where θ is the take-off angle.

According to the Beer-Lambert law, the photoelectron intensity from atom at depth t can be expressed as:

$$I_t = I_0 exp(-t/\lambda cos(\theta)) = I_0 exp(-t/\lambda_{eff}) \tag{2.3}$$

where I_0 is the intensity from the surface atoms. It is clear to see from equation 2.3 that X-ray photoemission spectroscopy (ARXPS) can perform nondestructive depth-profiling.

2.2 X-ray absorption spectroscopy (XAS) and photoemission electron microscopy (PEEM)

2.2.1 X-ray absorption spectroscopy (XAS)

X-ray absorption spectroscopy (XAS) is also based upon the photoexcitations, but depends on core to bound state excitations. The X-rays photon energy in XPS is fixed and the outgoing electron energy is measured, whereas XAS requirs intense tunable X-rays to generate a continuous energy spectrum. As a result, XAS experiments are performed at synchrotron sources. In XAS, the radiation X-ray energy is scanned and the absorption is observed. The absorption of X-ray is element specific, so XAS has broad-ranging applications. XAS measures the energy-dependent fine structure of the X-ray absorption coefficient near the absorption edge. The element, valance, crystal structure as well as magnetism characters can be obtained by XAS [2].

The X-ray absorption coefficient and the intensity change after the absorption process can also be described with the Beer-Lambert law in the form similar to equation 2.3:

$$I_{out} = I_0 exp[-\mu(E)t] \tag{2.4}$$

where $\mu(E)$ is the energy-dependent X-ray absorption coefficient. The $\mu(E)$ varies ap-

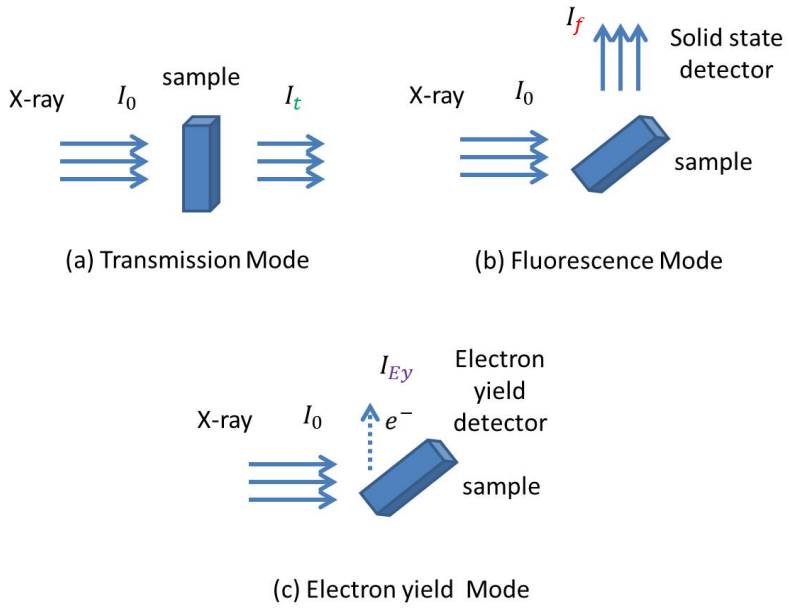

Figure 2.1: Schematic of the experimental setup for three XAS detection modes

proximately as $\mu(E) \sim dZ^4/mE^3$, where d is the target density and Z and m are the atomic number and mass, respectively. I_{out} is the outcome intensity measured by different modes.

In general, three main modes are used to detect XAS absorption coefficient [2], as shown in figure 2.1.

1. Transmission mode
2. Fluorescence mode
3. Electron yield mode

The transmission mode measures both the incoming and the transmitted beam, i.e. I_0 and I_t. In this mode, sample must be highly homogeneous. The pinholes or variations in the thickness of sample may introduce noise to XAS intensity measurement.

Comparing with transmission mode, other two modes are indirect measurements which exam the intensity of the incoming beam and of the decay products. The decay product can be fluorescent X-ray which is measured in fluorescence mode typically by an energy-

dispersive Si or Ge solid state detector. Another decay product after a X-ray absorption process is emitted photoelectrons, secondary electrons and Auger electrons.

The so-called "self-absorption" effects occur in fluorescent mode for thick or concentrated samples. However, the big advantage of the fluorescence mode is the ability to measure the insulating sample where the photoelectron suffers from "surface charging" in electron yield mode. In addition, fluorescence mode is useful for the non-homogeneous samples that are not suitable in transmission mode.

The electron yield mode measures the photolectron. The photoelectron can not only give the XAS information but with the electron microscope, it also can be used for imaging, known as X-ray photoemission electron microscopy (X-PEEM). The X-PEEM will be introduced in section 2.2.4

The XAS process can be described by Fermi's Golden Rule and where the absorption coefficient μ satisfies the following equation:

$$\mu \propto |\langle f|e\vec{r}|i\rangle|^2 \rho \propto |M|^2 \rho \tag{2.5}$$

where $|i\rangle$ and $|f\rangle$ denote the initial and final state, respectively. ρ is the density of state. $|\langle e\vec{r}\rangle|$ is the dipole matrix element coupling initial and final state. It can be rewritten as a single matrix element M. The combination of 2.4 and 2.4 with the one-electron approximation leads to a simple relation between XAS intensity I_{XAS} (which can be measured by any of three modes shown in figure 2.1) and electron matrix element M:

$$I_{XAS} \propto M^2 \rho \tag{2.6}$$

The matrix element M plays key role in interpreting the dichroism of X-ray absorption. Usually, synchrotron radiation is polarized linearly or circularly. Then the matrix element M depends on the orientation of the line connecting absorber and scattering atoms with

respect to the X-ray polarization. The orientation and polarization dependence give the rich dichrosim phenomena such as X-ray natural linear dichroism (XNLD), X-ray magnetic linear dichroism (XMLD), X-ray natural circular dichroism (XNCD) and X-ray magnetic circular dichroism (XMCD). In section 2.2.2 and 2.2.3, XNLD and XMCD will be briefly reviewed, respectively.

The dipole term $|\langle e\vec{r}\rangle|$ in equation 2.5 indicates that the well-known selection rules for transitions induced by electromagnetic interaction will apply. The allowed transition in a XAS process must satisfy the following selection rules:

- $\Delta l = \pm 1$
- $\Delta m_l = 0, \ \pm 1$
- $\Delta s = 0$
- $\Delta m_s = 0$

where l and s are orbital and spin angular momentum quantum number, respectively. m_l and m_s are the corresponding projections on the quantization axes.

It can also be concluded from equation 2.6 that the transition is forbidden if M equals zero. It is not necessary to evaluate M by integral of $|\langle f|e\vec{r}|i\rangle|^2$ if the group theory analysis can be done. In group theory there are two key rules to determine the nonzero value of ρ or I_{XAS} in equation 2.5 and 2.6. The two rules show $|\langle f|e\vec{r}|i\rangle|^2$ may be nonzero [3]

- If and only if $|i\rangle$ and $|f\rangle$ belong to the same irreducible representation of the point group respective of the crystal surface investigated.
- If the direct product of the representations of $|i\rangle$ and $|f\rangle$ with x, y, or z polarization is or contains the irreducible representation to which, x, y, or z, respectively, belongs.

It clear that the initial and final states of a XAS process need to be carefully analyzed. The initial state of XAS is from an occupied state. The created core-hole then is filled by an electron a higher energy state. The irradiated electron from initial state may be excited to an unoccupied state. This lead to a strong increase of the XAS intensity at particular X-ray energies corresponding to the energy difference between the occupied state and the unoccupied state. This type of XAS process reflects on a region of XAS which is referred as X-ray near edge structure (XANES). XANES probes local enviroment of an atom or the unoccupied density of the states.

With the higher X-ray photon energy, the XAS final state could no longer be a bound state, rather could be promoted to a free or continuum state. This type of XAS process reflects on a different region of XAS referred as extended X-ray absorption fine structure (EXAFS) which is about $\sim$ 30 eV above the absorption edge. In this dissertation, the XAS work focuses on the XANES study since XANES is more sensitive to the chemical bonding. XANES is influenced by the multiple scattering effects which can reveal the three-dimensional geometry of the crystal structure.

2.2.2 X-ray natural linear dichroism (XNLD)

The fact that matrix element M in equation 2.6 depends of X-ray polarization and sample orientation gives the dichroism signal in XAS. Linear dichroism describes angle dependent effects when the direction of the linear polarized $\mathbf{E}$ vector changes with respect to sample. If this dependence is from magnetic anisotropy, then the XAS is relative to the the magnetization direction of the sample, known as X-ray magnetic linear dichroism (XMLD). However, in nonmagnetic systems, the anisotropy may arise from the crystal field splitting of atoms or from the direction dependency of orbital moment distributions. The atom bonding caused dichroism is known as X-ray natural linear dichroism (XNLD) which measures the difference of two XAS with different linearly polarized X-ray beams.

The s polarized X-ray has **E** vector in the $a-b$ plane of a crystal and the p polarized X-ray has **E** vector along the c axis. The transition matrix element $|\langle f|e\vec{r}|i\rangle|^2$ may result in different values with polarized X-ray. If the local environment for an atom induces a large structural anisotropy, then XNLD may exist. This XNLD can also be used to distinguished different structure phases of a crystal. If the electron yield mode is used to measure the dichorism, then the imaging from photoeletrons can show the spatial phase separations of two structure phases by utilizing PEEM.

2.2.3 X-ray magnetic circular dichroism (XMCD)

Circular dichorism refers to absorption difference for left and right circularly polarized X-rays. XMCD measures the difference of two XAS with different circularly polarized X-ray beams. The dichorism is from the magnetic anisotropy of a sample. XMCD gives experimental access not only to the spin moment but also the orbital moment due to the spin-orbital coupling of atoms. XMCD assumes the difference between number of spin up and spin down holes of the occupied band gives the magnetic moment. Both the orbital and spin moments can be theoretically calculated from XMCD, known as the *XMCD sum rules*. For example, a 2p $\rightarrow$ 3d transition *sum rules* follows the equations [4]:

$$m_{orb} = -\frac{4\int_{L_3+L_2}(\mu_+ - \mu_-)dw}{3\int_{L_3+L_2}(\mu_+ + \mu_-)dw}(10 - n_3d) \tag{2.7}$$

$$m_{spin} = -\frac{6\int_{L_3}(\mu_+ - \mu_-)dw - 4\int_{L_3+L_2}(\mu_+ - \mu_-)dw}{\int_{L_3+L_2}(\mu_+ + \mu_-)dw}(10 - n_3d)(1 + \frac{7 < T_z >}{2 < S_z >}) \tag{2.8}$$

where the m_{orb} and m_{spin} are the orbital magnetic moment and spin magnetic moment in units of $\mu_B/atom$, respectively. The indices L_2 and L_3 refer to the X-ray absorption L edge with spin-orbital splitting. $(\mu_+ - \mu_-)$ is the XMCD spectrum and $(\mu_+ + \mu_-)$ is the sum of the XAS spectra. n_{3d} is the number of 3d electrons. $< T_z >$ is the ground state expectations value of the magnetic dipole term and $< S_z >$ is the corresponding spin operator.

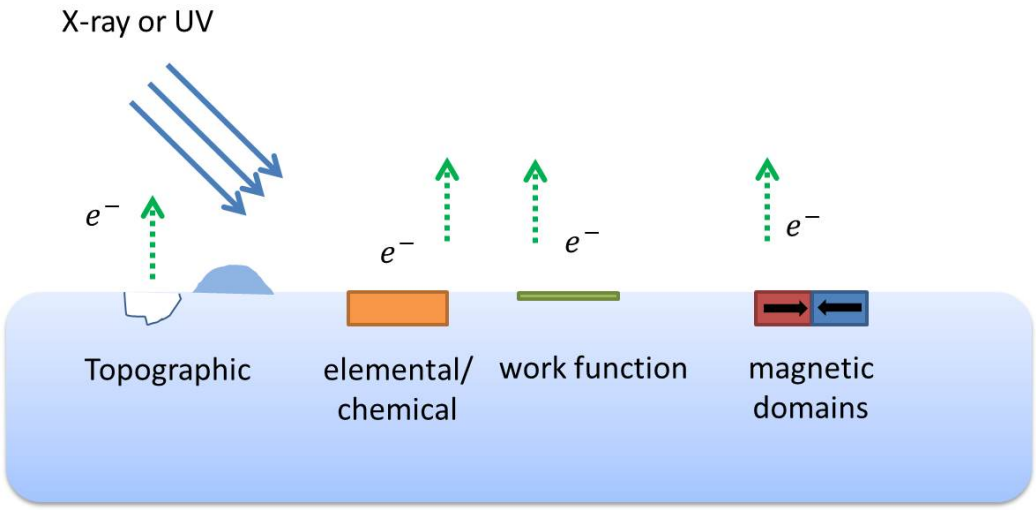

Figure 2.2: Contrast mechanisms in photoelectron emission microscopy (PEEM)

In the experiment, in order to get XMCD spectrum, the X-ray polarization can be fixed and the magnetization of sample with different direction is applied. An alternate way changes the polarization of X-ray but leave the sample unchanged. One of the major applications of XMCD is imaging the magnetic domain by utilizing the photoelectron imaging resulting in XMCD-PEEM.

2.2.4 X-ray photoemission electron microscopy (X-PEEM)

In the section 2.2.1, electron yield mode was introduced as a detection mode for XAS experiments. The outgoing photoelectron can pass electron optics (apertures, magnetic focus lens, etc.) similar to that found in a scanning electron microscopy to image the electron distribution illuminated by X-ray. This gives the X-ray photoemission electron microscopy (X-PEEM). If the ultra-violet light is used, it is referred as UV-PEEM. X-PEEM with X-ray from a synchrotron combines XAS spectroscopy and electron microscopy, which makes the XAS analysis, including XANES, XNLD, XMLD, XNCD, XMCD introduced in the previous sections, can be achieved with high spatial resolution. It is possible to identify the XAS spectral from a particular micro-region from a sample. The PEEM images are taken at

different incident X-ray energy. The image contrast usually changes with the X-ray energy indicating the interest regions at sample surface with rich features. The contrast mechanism in PEEM is summarized in figure 2.2

2.3 Low energy electron diffraction (LEED) and low energy electron microscopy (LEEM)

2.3.1 Low energy electron diffraction (LEED)

Low energy electron diffraction (LEED) is an ideal experimental technique for identifing the surface structure of the crystals [5]. The diffraction patterns are from the interaction between incident low energy electron beams (with energy range ~ 20 eV to ~ 400 eV) with the crystal atoms. Since the low energy electrons are used, LEED is a surface sensitive technique and surface region (< 1 nm) of a sample dominates. If the surface relaxation or reconstruction happens, this results in a change of LEED pattern or intensity. LEED diffraction follows the Laue condition, however, the energy dependent intensity is not only a result of Bragg scattering but also dynamical scattering [5].

Usually, LEED images are taken with the change of different incident electron energies. For a given diffraction spot, the intensities from images can be obtained with respect to different energies. This intensity vs energy plot is known as LEED I(V) curve. From the LEED I(V) curve, the surface symmetry and surface relaxation can be studied. It also possible to calculate the LEED I(V) curve through the multiple-scattering calculations. The LEED intensity decays exponentially with increasing temperature due to the Debye-Waller scattering [5]. By the temperature dependence study of LEED, the effect Debye temperature can be obtained by fitting the LEED intensity vs temperature plot.

2.3.2 Low energy electron microscopy (LEEM) and spin-polarized low energy electron microscopy (SPLEEM)

The diffracted electron beams in LEED can be used for imaging. If the diffraction center beam (i.e. the backscattered electrons undergoing no momentum transfer parallel to the surface) is selected to pass the electron optics, the so-called "bright field" image is formed. The low-energy electron microscopy (LEEM) characterization has wide range applications [6] and is one of the *in situ* techniques that are able to monitor the growth during the growth process [7]. The optics (apertures, focus lens, etc.) for LEEM imaging are also used for PEEM imaging with the UV or X-ray illumination source as introduced in section 2.2.4. LEEM forms the image from reflected electron beams from a sample surface while PEEM uses the photoelectron outgoing from a sample surface. From the experimental apparatus point of view, the PEEM and LEEM measurments are done in the same system, an integrated PEEM/LEEM system [6, 7].

Spin-polarized electron sources rely on GaAs photocathodes can be used as the electron source to make LEEM more powerful. The LEEM with spin-polarized electron gun, known as SPLEEM, is an ideal technique to study magnetic domain configurations and magnetic couplings in layered systems [7]. SPLEEM measures the spin-dependent electron reflectivity of sample surface. The spin-dependent reflectivity difference is expressed as an asymmetry signal $A = (I_+ - I_-)/(I_+ + I_-)$, where I_+ and I_- stand for the reflectivity for the different spin orientations. The origin of magnetic contrast is from the fact that the number of electrons backscattered elastically from the surface depends on the relative orientation of the spin polarization of the incident electrons and the surface magnetization [7].

References

[1] Hufner S 2003 Photoelectron Spectroscopy 3rd edn (Berlin: Springer)

[2] Schnohr C S and Ridgway M C 2015 X-ray absorption spectroscopy of semiconductors (Berlin:Springer)

[3] Cotton, F A 2008 Chemical applications of group theory (New Jersey: John Wiley & Sons)

[4] Chen C T, Idzerda Y U, Lin H J, Smith N V, Meigs G, Chaban E, Ho G H, Pellegrin E and Sette F 1995 *Phys. Rev. Lett.* **75** 152

[5] Clarke L J 1985 Surface Crystallography-An Introduction to Low Energy Electron Diffraction (New York: Wiley)

[6] Bauer E 2012 *Ultramicroscopy* **119** 18-23

[7] Rougemaille N and Schmid A K 2010 *Eur. Phys. J. Appl. Phys.* **50** 20101

Chapter 3

Surface and Interface Studies of Magnetoelectric Cr_2O_3

3.1 The surface stability of Cr_2O_3(0001)

3.1.1 Introduction

Previous studies, including low-energy electron diffraction (LEED) [1-3], X-ray diffraction [4, 5] and *ab initio* calculations [6, 7], have shown that there is a significant surface interlayer relaxation for the surface of Cr_2O_3(0001). Yet, not only has there been disagreement regarding the variation in layer spacing or relaxation for both the surface oxygen and chromium layers, but there fails to be agreement as to the surface termination of Cr_2O_3(0001)[1-7]. The general consensus is that the lattice parameter c of the first unit cell, the surface in fact, is compressed, with the consequence that steric hindrances should make the surface stiff. However, a recent LEED study on single-crystal Cr_2O_3 indicated that the first surface unit cell expanded with some missing chromium and oxygen atoms resulting in a softer surface [1].

In reality, the surface structure of oxides can be quite complex. Inward compression and underlayer expansion outwards can coexist, i.e. in the surface region, oscillatory variations in the lattice spacing are a common occurrence at oxide surfaces. Variation in surface composition and surface structure could also occur because of the different surface preparation conditions, as a result of changes in the surface stoichiometry and defect density. Further

complications arise when comparing thin films and bulk single crystals: structural deviations may exist in the thin-film system due to the interfacial strain caused by a mismatch with the substrate. A starting point to reconciling any controversy about the surface stability of Cr_2O_3(0001) is to assess the surface density and surface Debye temperature, and, if either of these is unusually low, to look for a very heterogeneous surface, characterized by multiple chemical states.

Several single crystals of Cr_2O_3(0001) were investigated to obtain the surface Debye temperature. In order to clean the surface contaminations for X-ray photoemission spectroscopy (XPS) and LEED measurements, the single crystals were sputtered by 1.5 keV Ar^+ ions, typically for 30 min at a sample emission current of about 5μA, and the crystals subsequently flash annealed to 1000 K. The temperature dependence of the LEED intensities were extracted over the range from 350 to 520 K in the electron kinetic energy range of 180-300 eV, and from 520 to 740 K at electron kinetic energies in the range 110-150 eV. Higher electron kinetic energies, for the LEED measurements at lower temperature, were adopted to reduce surface charging effects, the result of the well-established dielectric properties of Cr_2O_3(0001) single crystals. The samples were also investigated by core-level XPS, both to ensure surfaces free of contamination, and to establish the surface-to-bulk core-level shift. The XPS was obtained using Al Kα edge (photon energy 1486.6 eV). The calibrated core-level binding energies are reported with respect to the Fermi-level gold surface, in contact with the chromia, in terms of $E_F - E$. The effect of annealing in oxygen upon the oxygen vacancy density was variously explored by annealing the crystals in 1.5×10^{-7} Torr oxygen for 1 min at a sample temperature of 640 K or annealing 5×10^{-7} Torr oxygen for 10 min at 1000K (see text). The neutron reflectometry experiment was performed on highly (0001) textured thin films of Cr_2O_3 using the timeof- flight magnetism reflectometer at the Spallation Neutron Source at Oak Ridge National Laboratory [8]. The molecular beam epitaxy (MBE) grown thin films, on Al_2O_3 sapphire substrates, were used

instead of single crystal because such chromia thin films, even absent surface preparation, were observed to generally be more flat than polished bulk single crystal. The thin-film samples also provided a larger surface area available for the neutron reflectometry experiments as compared to the single crystals. Surface preparation of these samples was avoided so as to diminish possible complications resulting from any surface modification that might result from polishing. Neutrons with wavelength within the band of 2-8 $\AA$ were used in the experiments. Measurements were performed at room temperature on a Cr_2O_3(0001) thin film, with a thickness of 100 nm, grown by MBE on Al_2O_3 sapphire substrate. The experimental reflectivity profiles were fitted to the model scattering length density (SLD) layers, wherein the thickness of each layer, SLD and Gaussian roughness were optimized to minimize the χ^2 parameter between the measured and calculated reflectivity curves.

3.1.2 The imperfect Cr_2O_3(0001) surface

Neutron reflectometry is a depth-sensitive technique, with a resolution of 0.5 nm. This provides depth profile information on the scattering-length density (SLD or atomic number density). The SLD depends on the density and the composition of the material and there is an established relationship between the SLD and the lattice parameter [9]:

$$SLD \propto M/V \propto M/C \tag{3.1}$$

where M is the mass of Cr_2O_3 in atomic mass units for one unit cell, V is the volume of the unit cell, and C is the lattice parameter. The expected value for chromia scattering-length density (SLD) is $5.10 \times 10^{-6} \AA^{-2}$.

For a 100 nm thickness Cr_2O_3(0001) thin film grown on sapphire Al_2O_3, the neutron reflectivity data are shown in figure 3.1. Our best fit to the experimental data used a two-layer model for Cr_2O_3 thin film, one for surface, the other for the bulk of the Cr_2O_3(0001)

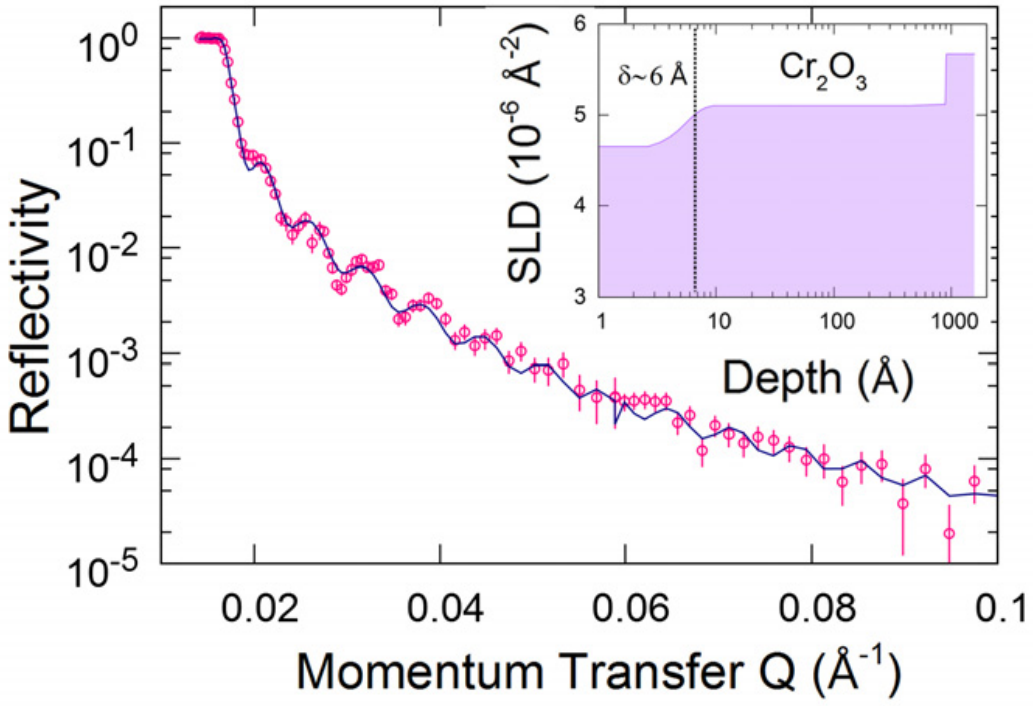

Figure 3.1: Unpolarized neutron reflectivity data for a 100 nm thick Cr_2O_3(0001) thin film grown on Al_2O_3. The experimental data (red) are overlaid by the best fit (blue curve). The error bars are indicated by the vertical lines. The inset shows the SLD versus the distance from the surface. The surface layer of 6 $\AA$ has a reduced scattering-length density of $4.64 \pm 0.3 \times 10^{-6} \AA^{-2}$. which increases to $5.10 \pm 0.02 \times 10^{-6} \AA^{-2}$ in the Cr_2O_3(0001) thin-film bulk (note that the depth, in the insert, is presented on a log scale).

thin film. With this fit, the neutron reflectivity reveals that there is a surface region of 6 thickness with a reduced SLD of $4.64 \pm 0.3 \times 10^{-6} \AA^{-2}$. The bulk volume of the Cr_2O_3 film has SLD of $5.10 \pm 0.02 \times 10^{-6} \AA^{-2}$, or basically very close to the expected value for chromia, based on equation 3.1. This suggests a surface with some surface roughness, but with a bulk density close to expectation. Thus the bulk of the thin film has few defects, vacancies, or voids so that the pristine Cr_2O_3 thin film system is close to ideal, within the resolution of neutron reflectometry.

Generally if the surface occupancy is perfect, then the measured surface layer reconstruction, leading to compression of the surface region, leads to an increased density in the surface region of the film. There is an inverse relationship between the SLD and lattice parameter, which permits us to estimate changes in SLD (compared with the expected SLD

value of chromia of $5.10 \pm 0.02 \times 10^{-6} \AA^{-2}$ noted above). The surfaces are observed to have only partial chromium or oxygen atoms occupancy [1, 4, 5] leading to a diminished surface-region scattering-length density, in spite of the surface-compression lattice parameter c. These lower surface densities due to the partial site occupancy, with typically only about 2/3 of the chromium sites occupied, while only 1/3 of the chromium atom sites are occupied in the subsurface (the underlayer or selvedge layer).

The observed partial chromium or oxygen occupancy are thought to be intrinsic to the Cr_2O_3(0001) surface [1, 4, 5]. Since surface defects abound and the surface is seen to have only partial density, a surface scattering density significantly less than the expected SLD value of chromia of $5.10 \times 10^{-6} \AA^{-2}$, is expected for the surface region (the top unit cell only).The resulting estimated lower surface region scattering length densities are in agreement with our neutron reflectivity data. But this cannot exclude further surface defects as a result of surface preparation. Oxide surface are fragile and almost any surface preparation, including a surface prepared by Ar^+ sputtering and higher temperature annealing, can introduce even more defects. This is explored here by X-ray photoemission in the next section.

3.1.3 Surface-to-bulk core-level shifts and defects

Angle-resolved x-ray photoemission can provide signatures of the expected distinct surface electronic structure but also provide indications of surface defects. Multiple O 1s corelevel features are evident in (XPS) taken for chromia following several different surface treatments, as seen in figure 3.2. The XPS spectra taken of Cr_2O_3(0001) single-crystal surfaces at first exhibit only a single O 1s core-level feature (figure 3.2(a)), in the vicinity of 530.7 $\pm$ 0.2 eVand ranging between 530.7 and 531.3 eV depending on surface preparation. This is generally consistent with most prior x-ray photoemission studies of chromia [10]. Yet after just a single Ar^+ ion sputtering treatment, to free the surface of contamination, a sec-

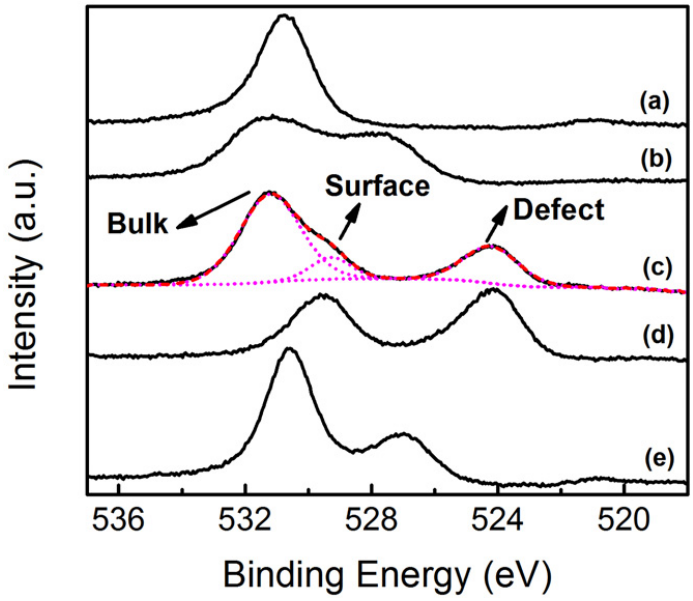

Figure 3.2: Angle-resolved x-ray photoemission spectra (ARXPS) curves of the chromia oxygen 1s peak for a selection of emission angles and various surface preparation: (a) normal emission (0°) spectrum for as-received $Cr_2O_3(0001)$ single-crystal surface; (b) normal emission (0°) spectrum after a simple Ar^+ ion sputtering treatment to remove surface contamination; (c) and (d) normal emission (0°) and an emission angle of 45° with respect to the surface normal spectrum after a simple Ar^+ ion sputtering and annealing in UHV respectively. To aid in the identification of the surface, the bulk and the defect oxygen 1s core level features (as indicated), spectrum (c) has been combined with a peak-fitting (dotted lines) to the various spectral components. (e) Normal emission (0°) spectrum after annealing the $Cr_2O_3(0001)$ single crystal surface in O_2 (5×10^{-7} Torr).

ond O 1s core-level feature is evident at much smaller binding energies. This second O 1s core-level feature has a binding energy that varies extensively with sputtering, ranging from 528 $\pm$ 0.3 to 524.2 $\pm$ 0.3 eV and suggests an oxygen species in the environment of a reduced chromium oxide.

With Ar^+ sputtering and annealing cycles, a surface peak and a 'defect' peak are evident in the O 1s core level spectra at 529.3 $\pm$ 0.2 and 524.2 $\pm$ 0.3 eV, respectively. Given the known structural readjustments at the surface [1,2, 4-7], combined with knowledge a distinct surface electronic structure, a surface to bulk core-level shift is not surprising. The surface component can be identified by the emission angle dependence of the photoelectron spectra: the larger take-off angle, with respect to the surface normal, increases surface sensitivity. With a photoelectron emission angle of 0°, with respect to the surface normal, the bulk O 1s component at 531.2 $\pm$ 0.3 eV dominates (figure 3.2(c)). For a take-off

angle of 45° (figure 3.2(d)), the surface component at 529.3 ± 0.2 eV and a defect peak now at 524.2 ± 0.3 eV have significantly increased intensity relative to the XPS O 1s core level component representative of the chromia bulk. Although it is not generally observed for the oxygen 1s core level of chromia, a surface-to-bulk core-level shift may explain the multiplicity of Cr 2p core level features frequently observed in the XPS spectra for chromia [10]. Since larger photoemission take-off angles, with respect to the surface normal, increase surface sensitivity, we may safely conclude that the defects are localized at the surface. The smaller binding energies for the surface defect component of the O 1s spectra, ranging from 528 ± 0.3 to 524.2 ± 0.3 eV, are consistent with oxygen vacancies in a locally reduced chromium environments. Since the defect peak was introduced by sputtering and high-temperature annealing, this feature in the O 1s core level spectra, with a binding energy very dependent on surface preparation, may well be related to the density of oxygen vacancies. After annealing the Cr_2O_3(0001) crystal surface in 5×10^{-7} Torr oxygen (O_2) for 10 min at 1000 K, the O 1s defect peak is reduced in both intensity but increases in binding energy (figure 3.2(e)), again consistent with removed oxygen vacancies. Note that the increase in the binding energy of the feature associated with defects indicates a more fully oxidized chromium in the vicinity of the defect sites. The reduction in the number or volume of the surface defects with oxygen exposure, as indicated by the XPS, is consistent with the LEED intensity versus electron energy curves.

Figure 3 shows that there are changes in the LEED beam intensities as a function of electron kinetic energy (i.e. I(V) curve) after annealing the Cr_2O_3(0001) surface in oxygen. At incident electron kinetic energies of 45 eV and 75 eV, the LEED scattering intensities increased by up to 27.8% and 10.5% respectively, after annealing the Cr_2O_3(0001) surface in 1.5×10^{-7} Torr oxygen for 1 min at sample temperature of 640 K. These changes in the LEED I(V) curves are indicative of improved structural surface order and consistent with the reduction of oxygen surface vacancies at or near the surface because of the very limited

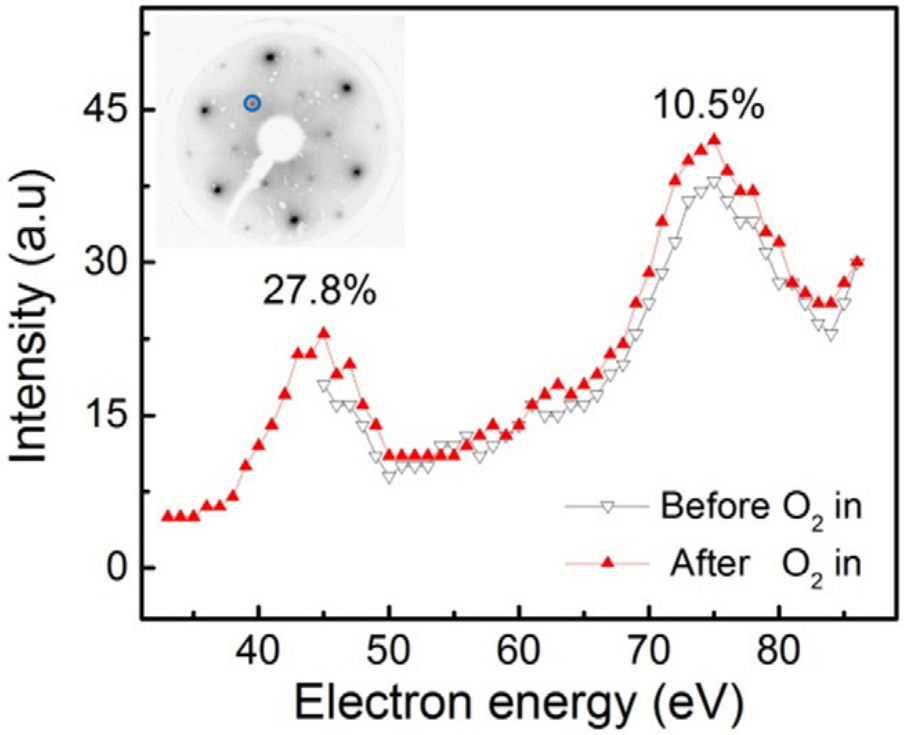

Figure 3.3: Low-energy electron diffraction (LEED) I(V) curves before (gray, inverted triangle in gray) and after (triangle in red) annealing the Cr_2O_3(0001) surface in 1.5×10^{-7}Torr oxygen for 1 min at 40 K. The incident electron kinetic energy was varied from 35 to 85 eV. The diffraction spot used to obtain the I(V) curves is indicated by the circle in the inset. Both I(V) curves were acquired at a sample temperature of 650 K, to reduce the surface charging.

electron mean free path of about 1 nm or less [11]. Our LEED I(V) curves support the argument [1-5] that different surface preparation conditions, in ultra-high vacuum (UHV), may lead to different termination, relaxation, reconstruction, and occupation of atoms.

3.1.4 The effective surface Debye temperature

The different chemical environments between surface and bulk atoms have the potential to profoundly influence the effective Debye temperature, related to the dynamic motion of atoms. The effective Debye temperature obtained by LEED is dominated by the vibration modes normal to the surface and parallel to the scattering vector Δk, and rarely includes anharmonic effects or in-plane motion. Due to Debye-Waller scattering, the LEED intensity decays exponentially with increasing temperature, as described by [11]: $I = I_0 \exp(-2W)$

and $W = 3\hbar^2 T(\Delta k)^2/(2mk_B\Theta_D^2)$ where W is the Debye-Waller factor, T is the sample temperature, $\hbar k$ is the electron momentum transfer in LEED, generally taken for incident and emission vectors close to the surface normal, m is the mass of the scattering center, k_B is the Boltzmann constant and Θ_D is the effective Debye temperature.

Typical LEED logarithm intensities, obtained from the single-crystal Cr_2O_3(0001) surface, change with the temperature, after the background subtraction, as illustrated in figure 3.4(a). From a linear fit to the logarithm of the intensity, the corresponding Debye temperature was obtained and plotted in figure 3.4(b) for various incident electron kinetic energies. The Debye temperature, for incident electron kinetic energies of 110 to 130 eV, varies from 483 $\pm$ 91 to 491 $\pm$ 12 K. For the higher incident electron kinetic energies of 180 to 300 eV, the effective Debye temperature varies from 729 $\pm$ 67 and 742 $\pm$ 204 to 53 6$\pm$ 48 K, with more weight toward the higher Debye temperatures, with an overall mean Debye temperatures of about 645 K (figure 3.4(b)). It is clear that at lower incident electron kinetic energies the effective Debye temperature is generally smaller. This is the result of greater surface sensitivity at lower electron kinetic energies. The electron mean free path, plotted in figure 3.3(b), is as follows:

$$\lambda = A/E^2 + B \times \sqrt{E} \tag{3.2}$$

where E is the incident electron kinetic energy in eV, with coefficients A and B discussed elsewhere [12]. The Debye temperatures obtained with LEED incident electron energies below 150 eV can be considered strongly weighted by surface components, while at incident electron kinetic energies larger than 180 eV, the effective Debye temperatures are more weighted by bulk contributions. For incident electron kinetic energies from 110 to 150 eV, where the effective Debye temperatures is around 490 K, which is very likely to be representative of the surface, as the penetration depth of the incident electron, plotted in figure 3.4(b), is around one unit cell of Cr_2O_3 at 150 eV (13.72 $\AA$) [6, 7]. This effective

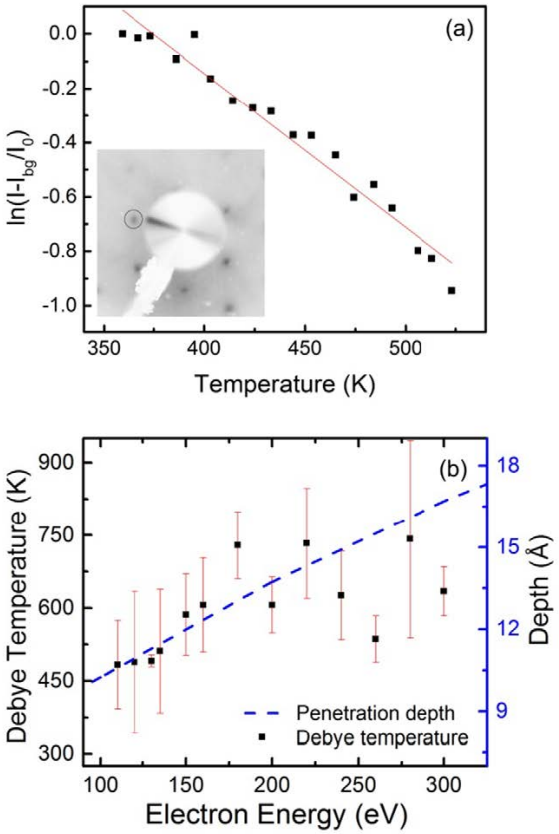

Figure 3.4: An exemplar low-energy electron diffraction (LEED) diffraction beam intensity plot, relative to the maximum intensity, from the surface of a $Cr_2O_3(0001)$ single crystal, obtained at an incident electron kinetic energy of 260 eV. The inset shows the LEED pattern and the diffraction beam, used for the data in the plot in (a), which is indicated by the circle. (b) Debye temperatures (black squares with the error bars shown with red vertical lines) extracted from the LEED beam intensities, as a function of temperature, at different incident electron kinetic energies. The dashed line corresponds to the expected electron mean free path or effective penetration depth versus the electron kinetic energy.

surface Debye temperature, around 490 K, is a significantly larger value than the 370K reported on the basis of the x-ray photoemission core-level signal, but much less than the 593K Debye temperature obtained from the low-temperature heat capacity of CrO_2 [13].

If we assume the surface atoms only have half the number of nearest neighbors that surround the bulk atoms, then the vibrational amplitudes are greater and treating the vibrational motion of atoms as harmonic oscillators, the force constant affecting an atom at the surface is 1/2 that of an atom in the bulk. This leads to an expectation that the surface effective Debye temperature has a value reduced from the effective bulk Debye temperature, and close to $\sqrt{2}$ of the bulk value [11]. On this basis, the LEED results for the effective

surface Debye temperature, as seen here for chromia, indicate that a reduced surface coordination (due to the presence of oxygen vacancies and increased surface roughness) does not lead to an unusually soft surface for $Cr_2O_3(0001)$, based on an effective surface Debye temperature close to $\sqrt{2}$ of the bulk value.

3.2 Metal adlayers on Cr_2O_3

Once chromia is in a heterojunction structure with a ferromagnetic metal, or any conductor, a permanent interface dipole results from the breaking of translation symmetry of the electronic potential. The electric field associated with this dipole does not switch on reversal of the antiferromagnetic domain state. It therefore breaks the symmetry by favoring one domain state over the other when it superimposes with the applied positive or negative electric field to form the local field which determines via magnetoelectric response the magnitude of the boundary magnetization. Certainly results [14] obtained for chromia in contact with a ferromagnetic metal do not exclude the interface static electric dipole as a contributing factor to the asymmetry in the switching field and/or in the magnitude of the exchange bias of one domain state over the other, so the interface must therefore be considered as a possible contributor to the asymmetry. The interface is likely important as a solely bulk measurement may exhibit no asymmetry in the switched magnetization.

3.2.1 Au on $Cr_2O_3(0001)$

3.2.1.1 Introduction

It is the objective of this investigation to provide evidence for the asymmetry in the boundary magnetization through surface sensitive spectroscopy. To better characterize the net Cr_2O_3 spin polarization at the boundary, we want to observe differences in the absolute magnitude for the spin polarization for the two domain states for a chromia single crys-

tal under a thin conducting overlayer and for a chromia thin film on top of a conducting substrate.

Cr_2O_3(0001) single crystal surfaces were prepared under ultrahigh vacuum conditions by Ar ion sputtering at 2 keV for a half hour followed by annealing. To place the Cr_2O_3(0001) single crystal in a single domain state [14-15], the sample was field cooled through the Neel temperature of 308K in the presence of both an electric field ($\sim$5 kV mm^{-1} and magnetic field ($\sim$50 Gauss). The magnetic field was applied either parallel or anti-parallel to the applied electric field.

SPLEEM [16] was used to measure the spin-dependent electron reflectivity of the Cr_2O_3(0001) surface. To supply an interface to a conductor, four atomic monolayers of gold were deposited from an e-beam heated crucible evaporator onto the surface of the Cr_2O_3(0001) single crystal at the rate of about 7 min per monolayer. Adding this chromia/metal interface has the added benefit of suppressing surface charging.

3.2.1.2 Polarization asymmetry

The SPLEEM measurements were performed after cooling the chromia crystal through the Neel temperature. The SPLEEM asymmetry signal was found to be particularly pronounced at electron kinetic energies of about 10.2 eV, where relatively high electron reflectivity coincides with a strong (negative) asymmetry signal. Figure 3.5(a) shows a time-averaged SPLEEM image of the Cr_2O_3(0001) surface (pixel-by-pixel average of 60 individual images), after the application of a $\sim$50 Gauss magnetic switching field applied on cooling from above the Neel temperature to below T_N. The uniform and featureless bright image indicates that the chromia surface is in a single domain state with spin-up boundary polarization. Figure 3.5(b) shows the same area of the surface prior to application of the switching field (again 60 frames were averaged): uniform dark field of the image indicates a boundary polarization switched into a spin-down single domain state. As

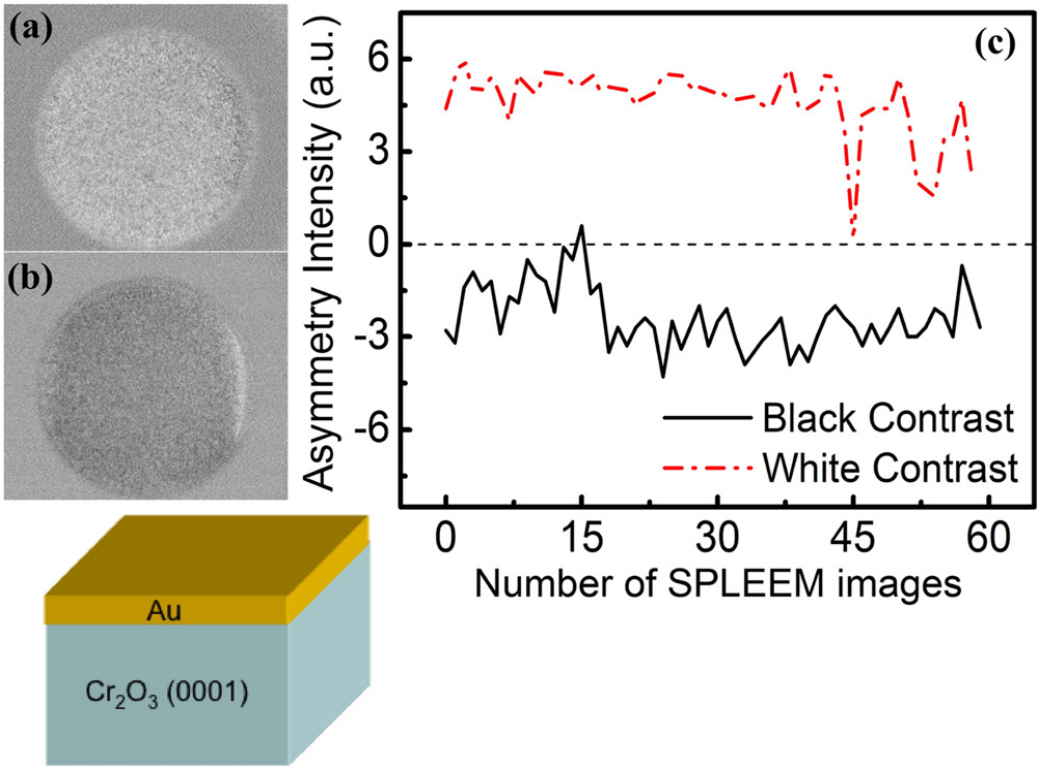

Figure 3.5: SPLEEM images of an area on the Cr_2O_3 surface, covered with a thin gold layer as shown in the schematic. The field of view is $\sim$14 μm and the electron energy is 10.2 eV. Panels (a) and (b) show long-time exposures (pixel-by-pixel averages of 60 frames), after application of a switching magnetic field ($\sim$ 50 Gauss) and prior to application of the switching field. Brightness and darkness in the images indicate magnetic single domain states with spin up and down boundary polarization, respectively. (c) Time traces of the asymmetry signal: the black solid line corresponds to negative asymmetry before application of the switching field, and the dashed red line corresponds to positive asymmetry after the field pulse, indicating the switch of the spin orientation at the Cr_2O_3 surface.

evident from the uniform images and uniform contrast indicated by figures 3.5(a), (b), any unreversed seed domains at the chromia surface, i.e. the chromia gold overlayer interface, present must be smaller than roughly 100 nm.

The average asymmetry signal of individual SPLEEM images is plotted as a function of time in figure 3.5(c), where the black/solid and red/dashed lines show the asymmetry signal prior to and after the application of the switching field. These measurements show that the magnetoelectric reversal of the chromia domain state is accompanied with a reversal of the surface polarization. The switching process also occurs isothermally below the Neel temperature, consistent with previous studies [14, 15].

The most striking observation is that the magnitude of asymmetry intensities is different for the opposite domain states and hence opposite surface polarizations (figure 3.5(c)). As noted at the outset, previous studies [14] have indicated that the surface boundary magnetization states produce a different magnitude of the exchange bias field in the (Co/Pd)n/Cr_2O_3 system. A spin-up surface boundary domain state results in a two-fold larger exchange bias than a spin-down boundary domain state. The domain state dependence of the exchange bias coincides with the SPLEEM spin polarization asymmetry measurements which are roughly twofold larger in the spin up domain state than the spin down domain state polarization of the Cr_2O_3(0001) surface, as seen in figure 3.5(c). If the variation in the magnitude of the spin polarization depends on the electrostatic interface dipole formed at the Cr_2O_3/metal boundary, then thickness variations in chromia films grown on a conducting metal substrate should matter as well. In the thin film limit, there should be thickness dependent variations in the magnitude of the surface magnetization on the vacuum interface of a Cr_2O_3(0001) thin film deposited on a conducting substrate, as screening of the electric interface dipole by the dielectric chromia is limited.

3.2.2 Cu on Cr_2O_3(0001)

3.2.2.1 Variations in surface magnetization with chromia film thickness

The experiments on the chromia thin films grown on Cu(111) were performed in ultra-high vacuum. The Cu(111) single crystal of purity $> 99.999\%$ was prepared by repeated cycles of Ar ion sputtering and annealing at a temperature of 850 K. The chromia thin film on the Cu(111) substrate was prepared by evaporation of two monolayers of metallic chromium onto the clean Cu(111) surface from an e-beam heated crucible evaporator, followed by annealing to 920K for 1 min in a partial oxygen pressure at 5×10^{-7} Torr. This leads to a very flat chromia thin film with pronounced texture along (0001) and little or no mosaic spread [17]. Samples were imaged with a low-temperature scanning tunneling

microscope (Omicron Nanotechnology). Topography images and spectroscopy maps were obtained under constant current mode at 77 K. Electrochemically etched polycrystalline W tips were cleaned in vacuo by annealing them at temperatures T $>$ 2200 K. The tunneling spectroscopy maps were obtained by adding a modulation voltage V_{mod} = 20mV rms to the applied bias voltage and recording the dI/dV signal by lock-in techniques. STM images were obtained at high bias voltages, typically 5.5 V, to overcome the significant 2.7 to 3.2 eV band gap of the films and low density of states at the valence band maximum and especially the conduction band minimum to tunnel out of the conduction band of the chromia films.

STM images of very thin chromium oxide Cr_2O_3(0001) films on Cu(111) are shown in figure 3.6. The island sizes are quite large [17], typically several micrometers, and the islands usually extend over several substrate terraces. The Cu substrate is also visible between the islands. Also shown in figures 3.6(b), (d) are dI/dV spectroscopy maps, which were recorded simultaneously with the STM images. The conductivity of the oxidized Cu substrate is higher than the conductivity of the Cr_2O_3 islands so that they appear brightest in the spectroscopy maps. Importantly, the spectroscopy maps reveal contrast across the Cr_2O_3(0001) islands on Cu(111), which corresponds to domains of different local conductivity within those islands. These domains can in some instances be correlated with the morphology of the islands, as in figures 3.6(a), (b), and in other cases these domains exist without corresponding features in the island morphology, as in figures 3.6(c), (d) and in the highlighted area in figure 3.6(b). The terrace step heights in a selected island of Cr_2O_3 are indicated in figure 3.6(a), where it appears that two types of step heights exist, which are $2\mathring{A} \pm 0.1\ \mathring{A}$, and $0.9\mathring{A} \pm 0.1\ \mathring{A}$. Careful comparison with the local conductivity map in figure 3.6(b) suggests that terraces of different local conductivity are separated by the smaller steps, while terraces of similar local conductivity are separated by larger steps.

The observation of two types of step heights and local conductivities suggests that two

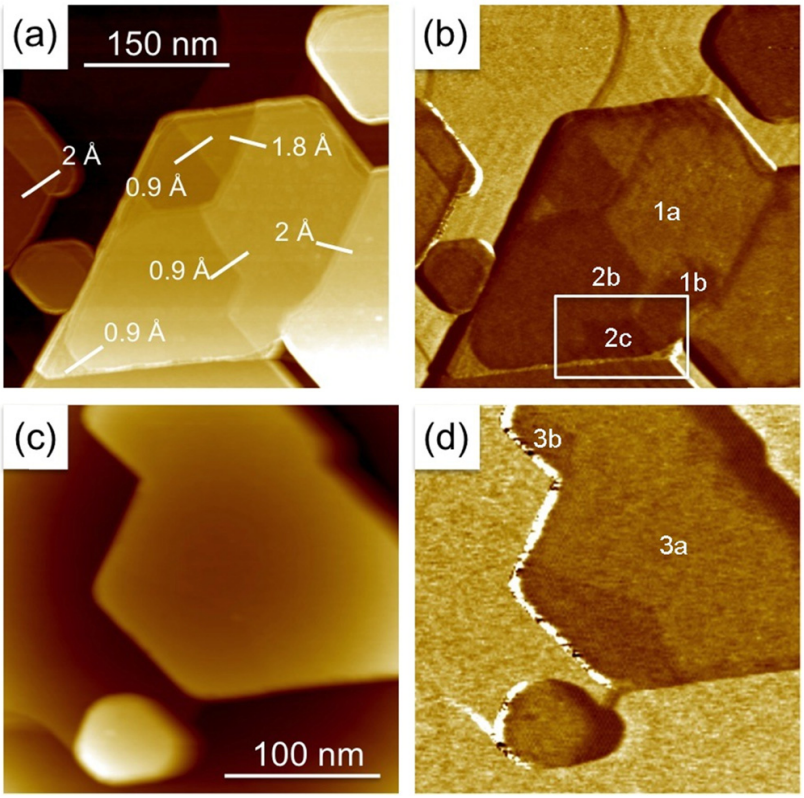

Figure 3.6: Scanning tunneling microscopy images (a), (c) and corresponding dI/dV tunneling spectroscopy maps (b), (d), of selected chromia islands on Cu(111). The oxidized Cu surface appears to have the highest local conductivity and appears brightest in the spectroscopy maps. There appears to be a strong correlation between the morphology of the chromia islands and the local conductivity in (a), (b), but not in (c), (d). Likewise, the contrast highlighted by a rectangle in (b) does not have a corresponding morphological feature in the island in (a); that is to say that (b)s regions of contrast 1(a) and 1(b) or 2(b) and 2(c) have unequivocally no corresponding morphological features in (a) and the different contrasting areas 3(a) and 3 in (d) have unequivocally no corresponding morphological features in (c). In (b), 1(b) and 2(b) share the same conductivity but are separated in (a) by what appears to be a small step. Tunnel parameters: UB = 5.5 V, I_T = 0.2 nA. Figure courtesy of Dr. Xumin Chen.

characteristic surface terminations corresponding to different cuts through the Cr_2O_3 unit cell coexist. For instance, for the typical termination of Cr_2O_3, layer distances of Cr−O and O−Cr are about 0.94 $\AA$. A complete layer of chromium atoms is actually rumpled a bit, so might be regarded as two layers, with the Cr−Cr layer spacing about 0.3 $\AA$ [18].

Two chemically equivalent (0001) surface terminations should occur in multiples of 2.3 $\AA$, which is the dimensions of the first four surface layers as Cr−O−Cr−Cr. The Cr−O layer spacing and the Cr−O−Cr−Cr layer spacing both seem to correspond reasonably well with the coexistence with both types of surface terminations. It should be noted, how-

ever, that the termination of the surface of Cr_2O_3 is much debated. Recent first principles calculations [19] suggest that the surface of Cr_2O_3 is Cr-terminated and thermodynamically stable in a broad temperature range between 165 K and well above room temperature, although detailed models invoking fractional Cr-layer occupancy have also been discussed [18]. The predicted stability of Cr termination [19] clearly speaks against the coexistence of Cr- and O-terminated surfaces, consistent with experimental results [17]. Moreover, our frequent experimental observation of conductivity domains that do not correlate with steps in the film, such as those in figures 3.6(c), (d), as well as the highlighted region in figure 3.6(b), are also inconsistent with the assumption of variations in the surface termination. As an alternative explanation, we suggest that there is a link between the two observed domains of local conductivity and the electrostatic surface dipole in the chromia film. This surface dipole effectively modulates the tunneling current and can explain the two types of conductivity domains observed here. Such a link between the orientation of electric polarization in a tunnel junction and the tunneling conductivity has been established in theory and experiment, and this is the fundamental contrast mechanism in the conductivity maps of the Cr_2O_3 islands here. Importantly here, the total dipole moment of the Cr_2O_3 islands is directly coupled to its surface magnetization, so that the dI/dV maps shown in figures 3.6(b), (d) include information about both the intrinsic dipole and the surface spin polarization. The Cr_2O_3 islands show typically two to three different conductivities, which we believe correspond to the dipole of the film (up or down), modulated by the dipole associated with the interface magnetization (up or down).

We note that STM measurements cannot be used to easily separate the dipole contributions at the surface and the buried copper-chromia interface, yet three out of the four possible expected contrast values expected are visible in figure 3.6(b). An interpretation that needs to be explored further is the possibility of partial/incomplete antiferromagnetic domain reversal, as has been suggested [20] based on observations of multiple energy

thresholds for domain reversal. While the antiferromagnetic domain reversal can occur uniformly under applied electric E and magnetic B fields, an interface dipole might lead to a diminished boundary polarization as a result of magneto-electric polarization of opposite sign from the static interface dipole, so that there is a type of frustrated ferroelectric domain reversal as a result of the interface dipole. This effect may be especially pronounced in the thin film limit. Partial domain reversal was suggested in [20], however, the influence of boundary polarization and interface dipoles was not considered. Interestingly enough, the magnetoeletric coefficients obtained through the measurement of single crystal magnetization also showed a factor two in the magnitude of the asymmetry, after magnetoeletric switching from one state to the other. Although the asymmetry in the magneto-electric susceptibility does not survive application of sufficiently high external fields, this is still evident as a metastable state or intermediate state for single crystal Cr_2O_3 without any adlayers. In light of the measurements reported here, this asymmetry in the switching field and/or in the magnitude of the exchange bias one domain state over the other may now safely be assumed to have a significant contribution from the surface magnetization once the boundary polarization is considered [14].

3.2.3 Pt and Pd on Cr_2O_3(0001)

3.2.3.1 Introduction

Previous sections 3.2.1 and 3.2.2 introduce the spin polarization asymmetry at the surface of chromia. The metal layers of Au and Cu are studied. To explain the observed exchange bias, not only must there be preservation of the interface spin polarization of chromia, but there must be induced spin polarization in the Pt or Pd spacer layer [14, 15], expected to be proportional to the Stoner susceptibility of the paramagnetic films.

Induced spin polarization in both Pt and Pd is certainly expected, based on a Landau-Ginzburg mean field approximation [21-23], and has been generally found to be consistent

with experiment, indeed now seen for Pt on a ferromagnetic oxide yttrium iron garnet (YIG) [24, 25], and chromia [25]. While inferred from the induced magnetization and anomalous Hall effect [25], and voltage controlled exchange bias [14, 15], confirmation of persistence of chromia boundary polarization, with a nonmagnetic layer has so far only been demonstrated for Au as introduced in section 3.2.1. In this study we investigate the effects of Pt and Pd thin film overlayers on the boundary magnetization of the (0001) surface of chromia and the converse effect, i.e. the induced spin polarization in the noble metals. Enhanced spin polarization in the Pt or Pd spacer layer will occur with an additional interface with a ferromagnetic layer, that is to say, when the paramagnetic Pt or Pd is bounded top and bottom with uncompensated spin polarization. This would be akin to a paramagnet with a magnetically ”live” surface [21-23]. Such a condition explains the successful exchange bias coupling between ferromagnetic Co/Pt and Co/Pd films via spacer layers of Pt and Pd as thick as a few nm [14]. As a starting point, one seeks insights into the spin polarization at the Pt or Pd to chromia interface. In this regard, XMCD has the probing depth to interrogate the buried Pt or Pd to chromia interface, as has been done with the Co chromia interface [26-29].

In the section, principally three types of samples were investigated: Pt/Cr_2O_3/Al_2O_3, Pd/Cr_2O_3/Al_2O_3, and Pt/Bulk (single crystal) Cr_2O_3. The Pt or Pd layer has thickness of $\sim$0.5 nm. The chromia thin films (with thickness of $\sim$65 nm) were deposited via pulsed laser deposition on $c-$plane (basal face) of sapphire single crystals. Half of the film was masked to leave a bare chromia surface. A very thin adlayer of Pd was deposited at 650 $^{\circ}$C followed by further Pd deposition to a total of 0.5 nm Pd, mostly deposited at $\sim$50 $^{\circ}$C. The Pd was then annealed at 650 $^{\circ}$C to smooth the surface. Pt was deposited on both chromia films and chromia single crystals by sputtering. The substrate was again masked as described above. Deposition was done at room temperature and then post annealed at 600 $^{\circ}$C. X-ray diffraction confirms the chromia and Pt/Pd films are crystalline with (0001)

and (111) orientations, respectively.

3.2.3.2 PEEM images and XMCD of Pt and Pd on Cr_2O_3

X-ray magnetic circular dichroism-photoemission electron microscopy (XMCD-PEEM) studies, utilizing a x-ray photoemission electron microscope (X-PEEM), have been carried out at the SM beamline of the Canadian Light Source, as previously applied to the investigation of chromia surfaces [15]. The PEEM images were taken at room temperature under zero magnetic fields. The antiferromagnetic magneto-electric chromia was placed into the single domain state by magneto-electric field cooling in a very large electric field, through the Neel temperature, as has proved, both here and previously [14, 15], quite successful in producing surface with high net spin polarization. While for an antiferromagnet, the XMCD contrast is generally expected to be negligible, due to the net boundary magnetization of Cr_2O_3, in the single domain state, there is a significant XMCD signal for chromia [15]. As schematically indicated in the figure 3.7(a) shows the X-PEEM and UV-PEEM images in the region of the boundary between the bare Cr_2O_3 surface and Pt or Pd (capping) overlayer. Ultra-violet light PEEM images for Pd/Cr_2O_3 (figure 3.7(b)) and Pt/Cr_2O_3 (figure 3.7(c)) were generated using a mercury-vapor lamp. The work function and valence band density of state variations for the metal overlayer versus the insulating Cr_2O_3 results in a notable contrast. For the x-ray PEEM, there is also contrast as seen in figure 3.7(d), taken at the photon energy of 570 eV (the Cr $2p_{3/2}$ pre-edge) and at 577 eV (the Cr $2p_{3/2}$ core), as seen in figure 3.7(e). In the latter case, contrast is dominated by the total electron yield, which is attenuated through the Pd or Pt overlayer, at the Cr $2p_{3/2}$ (L_3) absorption edge. Both UV-PEEM and X-PEEM show the clear boundary between the metal overlayer and bare chromia.

Both bare chromia surface and the interface with between chromia and the Pt or Pd overlayer exhibit a nonzero XMCD signal at the Cr $2p_{3/2}$ (L_3) edge, as extracted from

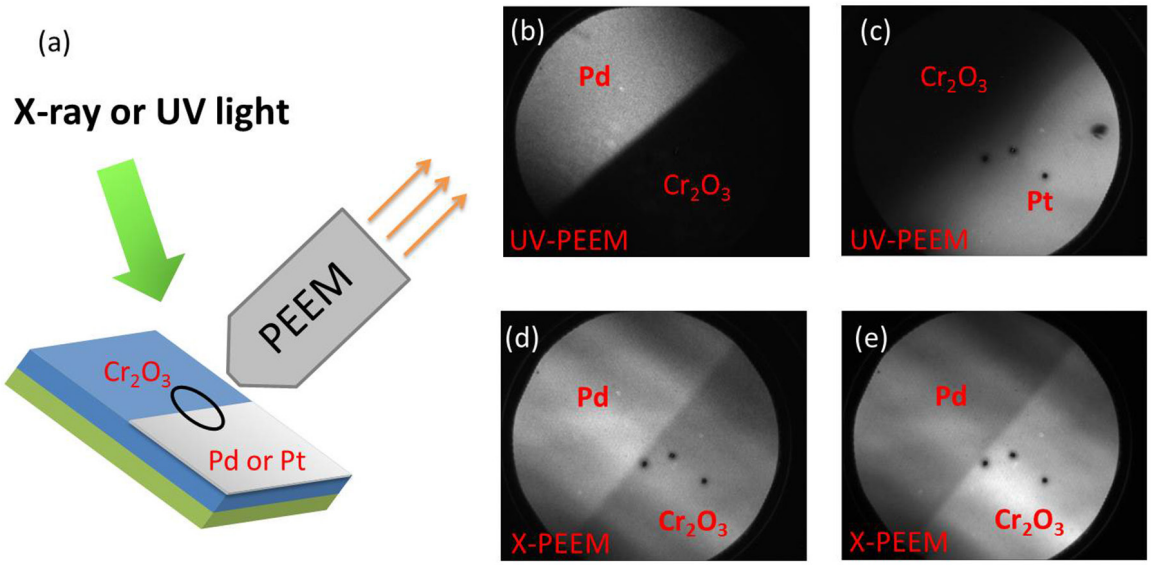

Figure 3.7: The schematic of PEEM geometry (a) and the mercury-vapor lamp ultra-violet PEEM images (the field of view is 75 nm) at the boundary between bare chromia (Cr_2O_3) with Pd on the Cr_2O_3 (b) and between bare chromia (Cr_2O_3) with Pt on Cr_2O_3 (c). For Pd on Cr_2O_3, The X-PEEM images have been taken at a number of different photon energies, as shown for Pd on Cr_2O_3 at the (d) pre-edge (570 eV) and (e) at the Cr $2p_{3/2}$ core edge (577 eV).

the difference between left and right circularly polarized light XAS spectra, as shown in figure 3.8. The advantage of XMCD-PEEM technique in our study over pure XMCD is that the XMCD intensity from metal layer and Cr_2O_3 can be obtained under exactly the same measurement conditions for the same sample. In each of the XMCD-PEEM images, one half of the image contributes the XMCD from bare Cr_2O_3 and other half from Cr_2O_3 with the metal layer. The bare Cr_2O_3 serves as a reference to compare intensity directly for XMCD signal. The XAS spectral intensities, at both Cr L_3 edge and L_2 edge, are attenuated through the Pd (figure 3.8(a)) or Pt (figure 3.8(b)) capping metal layer, when compared to the bare Cr_2O_3 surface for both Cr L_3, L_2 edges. The obtained XMCD signal on both the L_3 and L_2 edge is consistent with prior work [15, 26-29]. Based on the Cr $2p_{3/2}$ XMCD spectra, the chromia boundary spin moment is retained with both the Pd (figure 3.8(a)) and Pt (figure 3.8(b)) overlayers. The apparent suppression of the Cr $2p_{3/2}$ XMCD signal is greater with the Pd overlayer than with the Pt overlayer, as seen in figure 3.8. This could result from the expected decreased in boundary moment, as an adjacent paramagnet

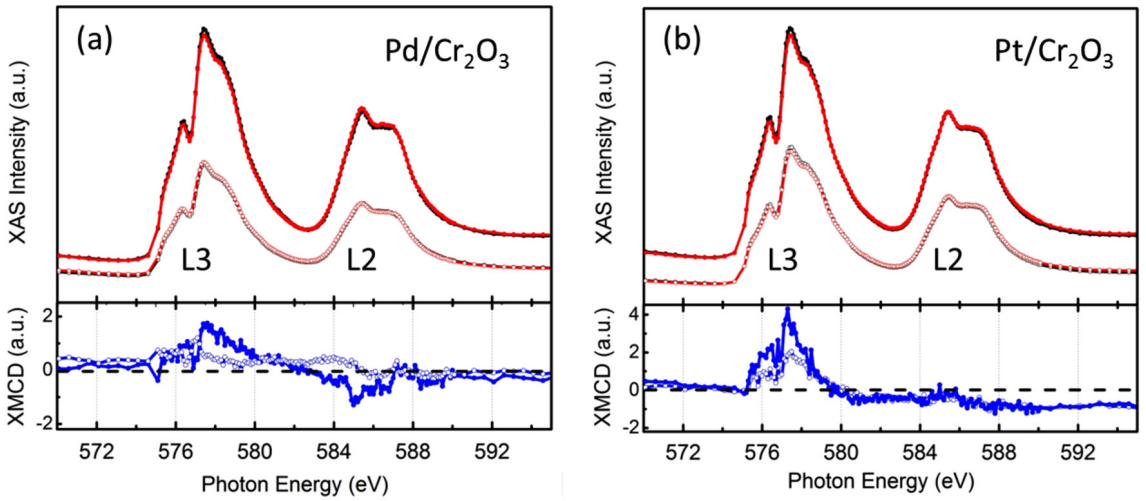

Figure 3.8: The XAS (red or black for μ^+ and μ^- right and left circularly polarized light respectively) and XMCD (blue) with metal on Cr_2O_3. The XAS and XMCD are shown by the solid circle for the Cr 2p edge of the bare Cr_2O_3 surface and by the hollow circles for the chromia interface with (a) Pd or (b) Pt capping layer.

is polarized [21-23], and is consistent with the larger molar magnetic susceptibility of Pd compared to Pt. In the context of a mean field theory, like the magnetization profiles obtained from the nonlinear Landau-Ginzburg equation, as the induced magnetization in the paramagnet increases, the boundary polarization in chromia (or an adjacent ferromagnet) decreases [22], especially if there is no reservoir of magnetization away from the interface. In the case of the live magnetic surface of the paramagnetic layer, as would occur with a ferromagnet on top (as occurs in the exchange bias systems of Cr_2O_3/Pd/$[Pd/Co]_n$ [14, 30] and Cr_2O_3/ Pt/$[Pt/Co]_n$ [31, 32]), the magnetization generally is expected to increase at both interfaces, and while decreased well within the paramagnetic layer, would be generally increased overall in the Pd or Pt layer taken as a whole [22, 23]. The XMCD results would also be influenced if the magnetization orientation is increasingly orthogonal to the XMCD geometry.

In the XMCD geometry used here, and the range of soft x-ray photoemission energies available, the induced polarization in Pd and Pt was difficult to detect directly. An induced moment has been observed, however, for Pt on YIG [24] and for Pt on cobalt [33]. There

are slight differences in the XMCD spectra, from one chromia, Cr_2O_3, sample to the next, as seen in the small difference for the bare chromia spectra in figure 3.8(a) compared to figure 3.8(b). The major problem in retaining signal fidelity is that Cr_2O_3 is a good dielectric and charging effects upon the photoemission signal degrade signal to noise, especially on weaker L_2 edge of Cr, and vary significantly from sample to sample. The circularly polarized light intensity at L_3 and L_2 edge of XMCD is consistent, with the sign of the signal reversed, to the left-right circularly polarized light intensities of previous work [15, 26-29] and not artifacts of two circularly polarized beam intensities. The sign change of the XMCD signal used here comes from a reversal of the single antiferromagnetic domain state, and hence results in a polarization reversal to that used in prior work. Nonetheless, it is clear that with a Pd or Pt overlayer, the Cr L_3 edge XMCD signal is suppressed relative to the Cr L_3 XMCD signal from bare Cr_2O_3.

3.2.3.3 MOKE of Pt on Cr_2O_3

We used polar magneto-optical Kerr effect (MOKE) to investigate the apparent magnetization, induced in an adjacent non-magnetic layer with high Stoner susceptibility via a pronounced proximity effect [21-25, 33] by the spin polarized surface of chromia [25]. The polar MOKE corresponds to a change in polarization of the reflected light under the presence of an out-of-plane magnetization. We conducted the polar MOKE using a photoelastic modulator to achieve high sensitivity. Here the Cr_2O_3 (0001) sample was magnetoelectrically annealed into an antiferromagnetic single domain state, with the help of a 5 nm thick Pt overlayer serving also as electrode. The annealing fields are turned off at temperature T = 290 K $<$ T_N, and temperature dependent polar Kerr measurement is conducted in zero-field heating using a 633 nm (red) laser, corresponding to an energy (roughly 2 eV) less than the band gap of chromia (2.7 eV). The wavelength was chosen with consideration for the crystal field theory where the magnetooptical effects are maximized.

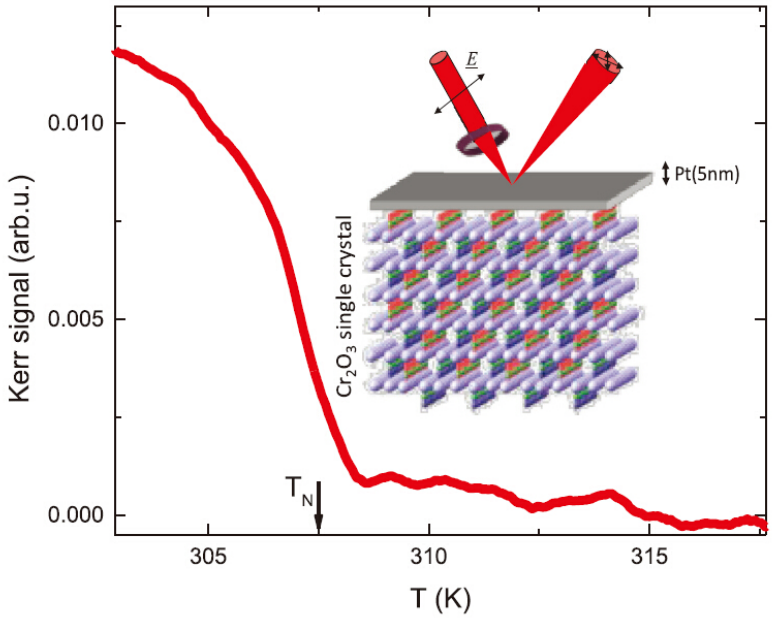

Figure 3.9: Temperature dependence of the polar Kerr signal of a 5 nm Pt film overlayer on the (0001) surface of a chromia single crystal. The Kerr signal reflects temperature dependence of the boundary magnetization of chromia. Inset: sketch of the sample and experimental geometry. Figure courtesy of Junlei Wang of Dr. Christian Binek's group.

Figure 3.9 shows the result of the temperature dependent polar Kerr measurement, where the signal originates from the induced magnetization of the 5 nm Pt overlayer film, adjacent to the $Cr_2O_3(0001)$ surface of a bulk chromia single crystal. The inset depicts the sample structure with a sketch of the polar MOKE experiment. Here, instead of being blocked by the non-magnetic Pt overlayer in zero applied field, the MOKE data indicate that the Pt overlayer acquires a sizable polarization from the exchange field created by chromia boundary magnetization. Evidence for this mechanism comes from the fact that the temperature dependence of the Kerr signal reflects the temperature dependence of the boundary magnetization of chromia. This is consistent with the induced magnetization within the 2 nm-thick conductive Pt layer on chromia, as measured by anomalous spin Hall magnetometry [25].

3.2.4 Low temperature growth of Co on Cr_2O_3(0001)

3.2.4.1 Introduction

The metal adlayers do not necessarily obscure the boundary spin polarization. The sections 3.2.1, 3.2.2 and 3.2.3 supports the contention that the chromia interface polarization can be preserved at a buried interface. This applied even to the Co/Cr_2O_3(0001) interface . The interaction of a ferromagnetic film, with a tendency for in-plane magnetization, with a surface with perpendicular spin polarization (like chromia), can be complex. The cobalt film morphology will profoundly affect its magnetic anisotropy [34], and thus is an important consideration when seeking understanding of the complex temperature dependence of the exchange bias in a Co/Cr_2O_3(0001) heterostructure. On metal substrates, the growth of cobalt is strongly related to the growth temperature [35, 36]. While cobalt thin film growth tends to form islands, following a Volmer-Weber growth mode on oxide substrates at room temperature [34], cobalt growth on magnetically ordered oxide substrates, such as Cr_2O_3(0001), has been very sparsely investigated for substrate temperatures below room temperature and thus below the antiferromagnetic ordering temperature. To add some clarity to the issues surrounding cobalt growth on an antiferromagnetic oxide substrate with high boundary polarization, we have investigated the temperature dependent growth and the magnetism of Co on Cr_2O_3(0001).

Before deposition of the cobalt film, the Cr_2O_3(00 0 1) single crystal substrate surfaces were prepared under ultrahigh vacuum conditions by Ar^+ ion sputtering at 1 kV for half an hour and then annealed. The surface order was established by low energy electron diffraction (LEED). The cobalt adlayer was deposited through e-beam thermal deposition at rate of $\sim$2 min per monolayer on Cr_2O_3(0001) at various chromia substrate temperatures. The cobalt growth rate was calibrated against growth of cobalt on copper substrates.

The low-energy electron microscopy (LEEM) characterization is one of the in situ tech-

niques that are able to monitor the growth during the growth process. The base pressure of the LEEM chamber was in 10^{-11} torr range, suppressing oxidization of the Co adlayer during growth and the LEEM measurements. All the LEEM measurements (LEEM Image or LEEM I/V spectra) were done at the corresponding growth temperature.

The MFM images acquired by a Bruker-ICON magnetic force microscopy using high-performance MFM Probes (MESP-RC-V2, Bruker) with a magnetic Cobalt-Chromium coating. The Co/Cr hard magnetic coated MFM tips are tailored for high-sensitivity and magnetic contrast. The magnetization of the MFM tip is perpendicular to the sample surface and points downward, in the geometry of our experiment. All the MFM images were obtained using the phase modulation detection mode due to its ease of use, better signal-to-noise ratio, and reduced artifacts content. The magnetic tip was kept at a lift height of 20 nm over the sample surface and was oscillated at resonance frequency (tapping/lift mode). As the MFM tip was scanned across the sample surface, the strength of the magnetic interaction between the tip and the magnetic stray fields of the sample results in a phase shift in the oscillation, the basis for the MFM mapping shown here. The MFM phase images here are a measure of the phase lag between the drive voltage and the cantilever response, and illustrative of the magnetic force gradient distribution on a samples surface. The $\sim$16 monolayer thick cobalt adlayer film on chromia, with a native CoO surface, was selected for further magneto-optic Kerr effect (MOKE) and magnetic force microscopy (MFM) measurements.

As a check the magnetic anisotropy and cobalt film morphology, CoO/Co/Cr_2O_3(0001) and CoO/Co/Al_2O_3(0001) heterostructures were compared both above and below the Neel temperature (307 K) of chromia. The cobalt films on Al_2O_3(0001) were deposited by thermal evaporation under ultrahigh vacuum conditions at 0.1 $\AA$ min^{-1}. To investigate the magnetic anisotropy of Co/Cr_2O_3(0001), we performed the measurement of the magneto-optic kerr effect (MOKE).

To ascertain the film purity and composition, angleresolved x-ray photoemission spectra were obtained using SPECS PHOIBOS 150 energy analyzer. The angle-resolved x-ray photoemission spectra (ARXPS) was used to establish that the CoO layer for the $CoO/Co/Cr_2O_3$ heterostructure was limited to a surface oxide and that the subsurface cobalt was largely free of oxidation, thus making the observed CoO largely a passivation layer. A non-monochromatized Al Kα X-ray source, with photon energy 1486.6 eV, was used with various emission angles. The LEED, MFM, MOKE and ARXPS measurements were done at room temperature.

3.2.4.2 The dependence of the cobalt adlayer morphology on growth temperature

In general, with cobalt film growth on chromia, the cobalt adlayers were seen to form a more uniform film on chromia with a growth temperature below room temperature than with cobalt film growth at room temperature, the latter being the more typical substrate temperature. For the cobalt films grown on chromia with substrate temperatures of 100 K, the LEEM intensity versus energy spectra (LEEM I(V)) indicate dynamical and kinematic scattering characteristics of an ordered film with improved flatness compared to the cobalt films grown on chromia at room temperature. In figure 3.10(a), kinematic scattering characteristics of an ordered film (the peak at around 14 eV in the LEEM I(V) curve) are seen in (1) but not in (2) or (3). The latter show a simple decaying LEEM I(V) intensity with increased electron energy and little evidence of dynamic and kinematic (Bragg) scattering in the very low energy intensity versus voltage curves. The LEEM images also show the films to be flatter or smoother for the cobalt films grown on chromia with substrate temperatures of 100 K (figure 3.10(b)) as compared to the cobalt films grown on chromia at room temperature (figure 3.10(c)). The LEEM did not show significant differences in crystallographic order or morphology for cobalt films grown at the low temperature 100 K and those grown at the low temperature and then annealing to room temperature.

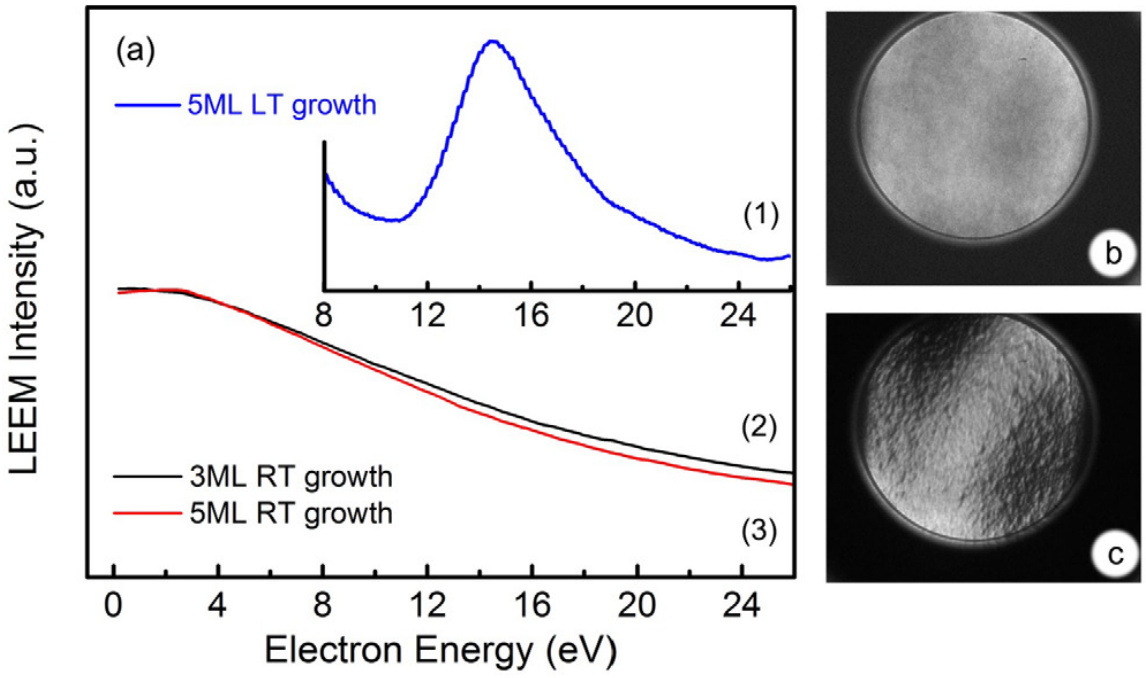

Figure 3.10: The low-energy electron microscopy intensity versus incident electron energy (LEEM I(V)) curves. The spectra (1) is for 5 monolayer (ML) Co grown on $Cr_2O_3(0001)$ at about 100 K i.e. low temperature. The spectra (2) is for 3 ML and (3) is for 5 ML Co films grown on $Cr_2O_3(0001)$ at room temperature (RT), respectively. The LEEM images, taken at an electron energy of $\sim$15 eV, of a 5 monolayer Co grown on $Cr_2O_3(0001)$, are shown for films grown at (b) at low temperature (100 K) and (c) at room temperature.

The cobalt films grown on chromia at room temperature are still not uniformly metallic as a 5 monolayer Co film grown at room temperature exhibits strong charging effects. This means that the cobalt films grown at room temperature and above show a degree of roughness which prevents the cobalt islands in the surface film from exhibiting complete percolation. The charging effect, resulting in deformed LEEM images (figure 3.10(c)), indicates that the dielectric properties of the chromia single crystal substrate dominate and neither a conducting surface nor a metallic thin cobalt film, with percolation, exists uniformly across the surface. The cobalt films, grown on chromia at room temperature, probably follow Volmer-Weber or island growth mode, as reported for other cobalt films [34].

For cobalt films grown on chromia at substrate temperatures of 100 K, the charging effects in LEEM imaging are minimal (figure 3.10(b)). The low energy electron diffraction (LEED) pattern/ images were taken after the gentle annealing of film to room temperature

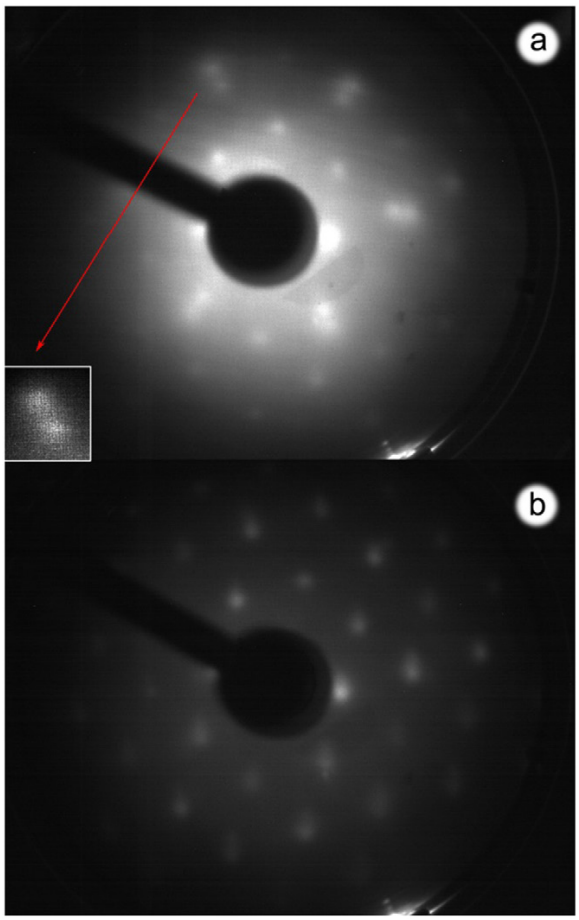

Figure 3.11: (a) The low energy electron diffraction (LEED) of thin Co adlayers grown on $Cr_2O_3(0001)$ at ∼100 K, and for comparison, (b) a LEED image of a clean $Cr_2O_3(0001)$ single crystal, prior to cobalt deposition. The diffraction spot-splitting is highlighted in the inset of (a) and clearly shows the Co adlayer crystallography follows the $Cr_2O_3(0001)$ substrate crystal orientation, but is not lattice matched, as there exist two closely spaced diffraction beams. The incident electron energy is 159 eV

and are characteristic of cobalt adlayers with a high degree of crystallographic order, as seen in figure 3.11(a). The six-fold diffraction pattern from the cobalt adlayer (figure 3.11(a)) has the same angular orientation as the chromia substrate (figure 3.11(b)), even if not lattice matched. This means that likely there are multiple C_{3v} symmetry domains of cobalt (111), where each domain maintains crystallographic registry with the C_{3v} symmetric chromia surface, so in combination, the LEED has 6-fold symmetry.

Figure 3.12 illustrates the thickness dependence of the LEEM I(V) spectra for Co adlayers growth at 100 K ranging from ∼5 monolayers to ∼16 monolayers. The LEEM I(V)

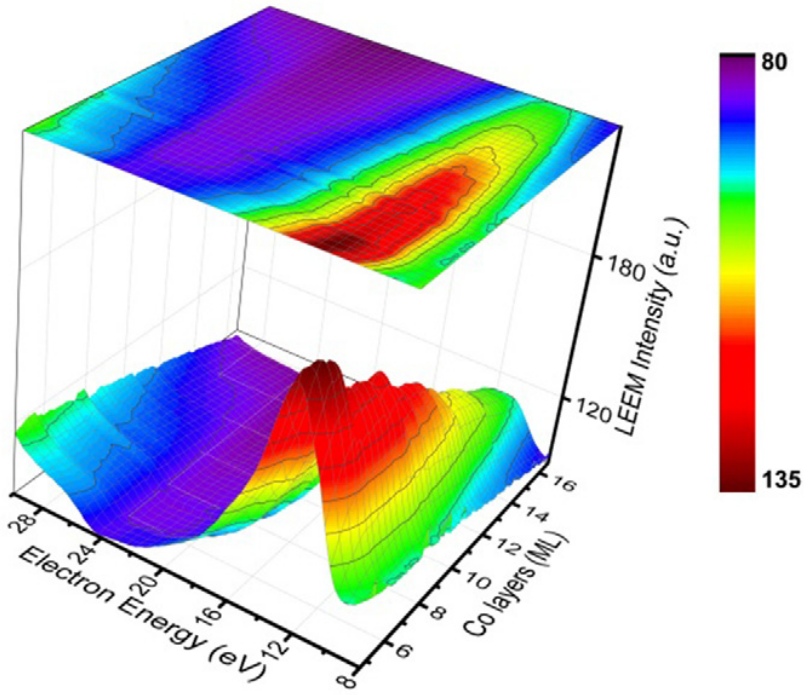

Figure 3.12: The cobalt thickness dependence of LEEM I(V) spectra up to a cobalt adlayer thickness of roughly ∼16 monolayers. The LEEM I(V) intensities shows a scattering peak around 12-16 eV, characteristic of a crystalline cobalt adlayer, that varies with the thickness of the Co adlayers.

intensity decreases and shifts in energy with the increasing of Co thin film thickness. This indicates that not only are the thinner films more crystalline, but the thinner films tend to grow uniform layers as indicated by the plateaus and sharp drops in the 15 eV LEEM I(V) peak at nominally 6 and 8 monolayers of cobalt (figure 3.12). The diminished LEED diffraction beam intensities measured for thicker cobalt adlayers (some 14 to 16 monolayers) on chromia indicate that such films contain more disorder than the thinner (5 to 6 monolayers), more crystalline, cobalt films grown on chromia with substrate temperatures of 100 K. This is consistent with the greater roughness (6.37 nm to 8.24 nm root mean square roughness) seen in atomic force microscopy (AFM) (figures 3.13(a) and (c)), as well as with the LEEM results of figure 3.12. By way of comparison, Co grown on $Al_2O_3(0001)$ single crystals, at room temperature, results in cobalt adlayer films that are very flat and uniform (root mean square roughness of about 0.16 nm), preserving the ter-

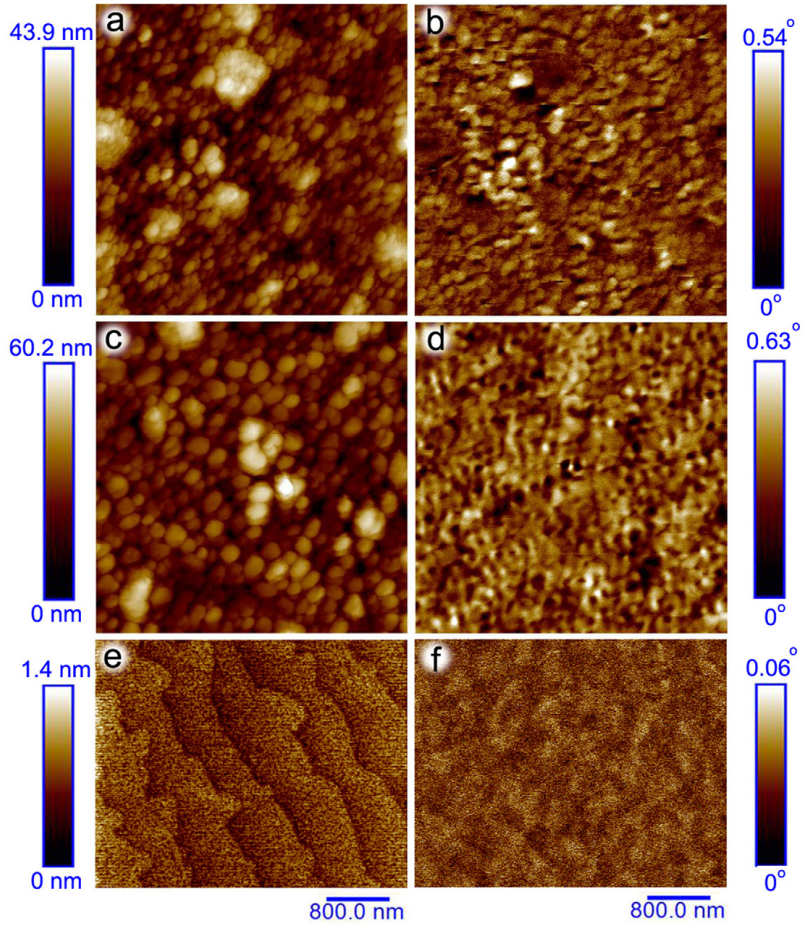

Figure 3.13: The AFM (a, c and e) and MFM (b, d, and f) images of 16 monolayer (a, b) and 25 monolayer (c, d) cobalt adlayer thin films grown on a $Cr_2O_3(0001)$ single crystal at 100 K compared with a 16 monolayer cobalt film grown on an $Al_2O_3(0001)$ single crystal at room temperature (e, f).

race and step structure of the $Al_2O_3(0001)$ single crystal surface, as seen in figure 3.13(e). This indicates a tendency towards layer-by-layer growths or the Frankvan der Merwe (FM) growth mode for Co grown on $Al_2O_3(0001)$ single crystals. So roughness of cobalt adlayers, when grown at room temperature, is dependent upon the dielectric oxide surface chosen.

3.2.4.3 In-plane magnetic anisotropy of the cobalt adlayer

Consistent with most studies of cobalt thin films [37], the easy magnetization axis resides in-plane, as is evident in magneto-optic Kerr effect MOKE studies of figure 3.14. The lon-

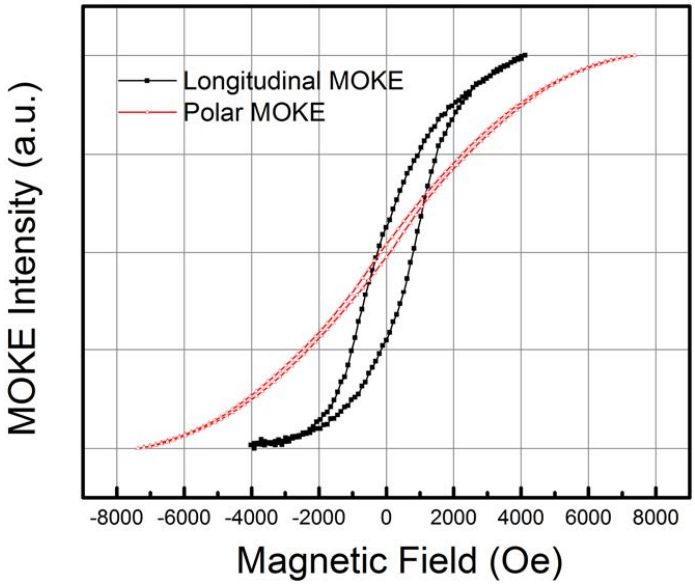

Figure 3.14: The MOKE derived magnetic (relative M(H)) hysteresis loop of a 16 monolayer Co adlayers grown on $Cr_2O_3(0001)$ at $\sim$100 K, accompanied by a CoO oxidation capping layer.

gitudinal MOKE results, illustrated in figure 3.14, clearly indicates that the easy axis of the 16 monolayer cobalt film, grown on $Cr_2O_3(0001)$ at $\sim$100 K, is preferentially in-plane. The magnetic hysteresis loops indicate that the remanent magnetization of our cobalt adlayer films is small, which may reduce the sensitivity of spin-polarized low-energy electron microscopy (SPLEEM) to the cobalt surface polarization. Indeed, we found that SPLEEM was insensitive to cobalt grown on chromia, providing no indication of a significant spin asymmetry intensity.

A cobalt adlayer domain structure was observed in the MFM images (figures 3.13(b) and (d)), and evident in the sharp bright-dark contrast. This $Co/Cr_2O_3(0001)$ MFM contrast is indicative of a large out-of-plane component of magnetization associated with each magnetic domain. MFM tip is most sensitive to variations of magnetic structure near sample surface: the magnetic moment of the tip interact with the stray fields from the sample and is sensitive to the repulsive and attractive force gradients normal to the surface. This out-of-plane magnetic contrast for $Co/Cr_2O_3(0001)$ is especially evident when comparing

the images with figure 3.13(f), which shows the MFM of Co grown on a $Al_2O_3(0001)$ single crystal. The MFM scale for the $Co/Al_2O_3(0001)$ image is increased 10 times in (f)on the same scale as (b) and (d), the MFM images for $Co/Cr_2O_3(0001)$, the image (f) would show no contrast. We again note that these magnetic attractive/repulsive forces cause shifts of both the resonance frequency and the phase. Many magnetic grains participate in the formation of an interaction domain in which the grains exhibit the similar orientation of magnetization (up and/or down domains), yet the MFM phase image contrast represents magnetic-forcegradient mapping largely normal to the surface. In this case, the bright domain indicates the tip is repulsive to the spot, while the black domain indicates it is attractive. So the out-of plane component of magnetization is far more significant for cobalt on chromia, than cobalt on sapphire (Al_2O_3). The corresponding AFM images (a) and (c) show increasing grain size within the Co adlayer with increasing Co thin film thickness following growth on $Cr_2O_3(0001)$ single crystal at 100 K. The AFM image of cobalt thin film on Al_2O_3 shows atomic terraces (e), induced by the substrate, while the AFM images for $Co/Cr_2O_3(0001)$ do not, due to the cobalt adlayer roughness.

Figure 3.15 shows the differences in the x-ray photoemission (XPS) spectra before and after Ar^+ ion sputtering. After Ar^+ sputtering, the oxide XPS peaks characteristic of the oxidized cobalt (denoted by the arrows) are absent, indicating that the presence of oxygen evident in these XPS spectra is associated with a CoO capping layer. After removing the CoO capping layer, the cobalt adlayer is seen to be very close to pure Co metal in these XPS spectra. So the signature of CoO that appears in the XPS is dominantly the result of surface oxidation. Yet a possible role of interfacial oxidation cannot be excluded a priori. Interfacial oxidation of cobalt adlayer films has been implicated as a possible origin of perpendicular magnetization [37], as have other interfacial effects [34]. In addition, the perpendicular magnetization, resulting from the boundary magnetization of Cr_2O_3, provides a mechanism for strong contrast in MFM [14, 15]. Due to the interfacial collinear cou-

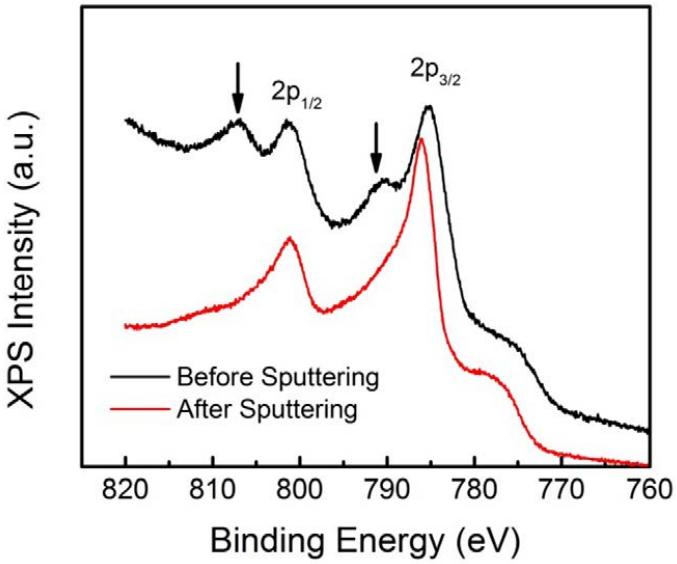

Figure 3.15: The cobalt 2p core level XPS spectra for 16 monolayer Co adlayers grown on Cr_2O_3(0001) at ∼100 K before and after Ar^+ sputtering. The Ar^+ sputtering was done to diminish or remove a surface (but not interface) CoO oxidation capping layer. The oxidization peaks characteristic of the oxidized cobalt (shown by the arrows) are absent, indicating that the existence of oxidized cobalt is restricted to a capping layer.

pling between Co and Cr of Cr_2O_3, the cobalt adlayer film may show a large perpendicular magnetic moment despite the tendency for cobalt to exhibit in-plane magnetic anisotropy.

3.3 Graphene on Cr_2O_3

The surface study of Cr_2O_3 and the interface study of Cr_2O_3 with metal layers are motived by the application of magnetoelectric magnetic tunnel junction (ME-MTJ) [38]. The noble metal cap layer or buffer layer such as Au, Pt or Pd and ferromagnetic metal layer such as Co consist of the functional cell of a magnetoelectric magnetic tunnel junction. It is also possible to make a magnetoelectric spin field effect transistor (ME-spinFET) [38, 39] from an interface system which is constructed by 2D channel conductors (graphene, MoS_2, WS_2, $MoSe_2$, etc.) and magnetoelectric materials such as Cr_2O_3. In the following section, the graphene/Cr_2O_3 interface is studied to shed some light on magnetoelectric spin FET [38, 39].

3.3.1 Moving towards the magnetoelectric graphene transistor

The graphene/Cr_2O_3(0001) system could offer a route to a nonvolatile magnetoelectric spin valve or spin FET [38, 39]. In this work, we report a systematic study of interfacial charge transfer in graphene/Cr_2O_3(0001) heterostructures. Scanning probe microscopy and Raman studies reveal an interfacial charge transfer between these materials, and point to p-type doping of the graphene with up to a 150 meV shift in the Fermi level. The charge transfer effect and the induced spin polarization of the graphene are investigated using density-functional theory (DFT). These calculations show that the charge transfer is relatively small, while the induced spin polarization is extremely high in the vicinity of the Fermi level of graphene, implying that a large magnetoelectrically driven magnetoresistance can be expected for this system. This magnetoelectric interface may therefore be important for developing spintronic applications.

Figure 3.16(a) shows a tapping-mode AFM topography image of a few layer graphene (FLG) flake on Cr_2O_3(0001). The majority of the graphene surface is flat, with isolated puddle areas with lower height signals. These features cannot be directly correlated with the morphology of the chromia surface and are not observed in the contact mode image (figure 3.17(a)), suggesting different types of graphene/chromia interface interaction, which may originate from a variation in the interfacial adsorbate layer. Similar puddles can also be resolved in the EFM measurements. Figures 3.16(b)-(d) show the EFM phase mapping of the same region for DC tip voltages of 0 V, +10 V and -10 V, respectively. We compared the signal profiles along the same line at different bias voltages (figure 3.16(e)). For consistency, we chose a region where no puddle features are present. At zero tip bias, there is no apparent difference in the EFM phase signal between the graphene and chromia surfaces, except at the graphene boundaries. In contrast, a clear negative phase shift is observed on graphene at a non-zero tip bias, suggesting an enhanced tip-sample interaction. This is un-

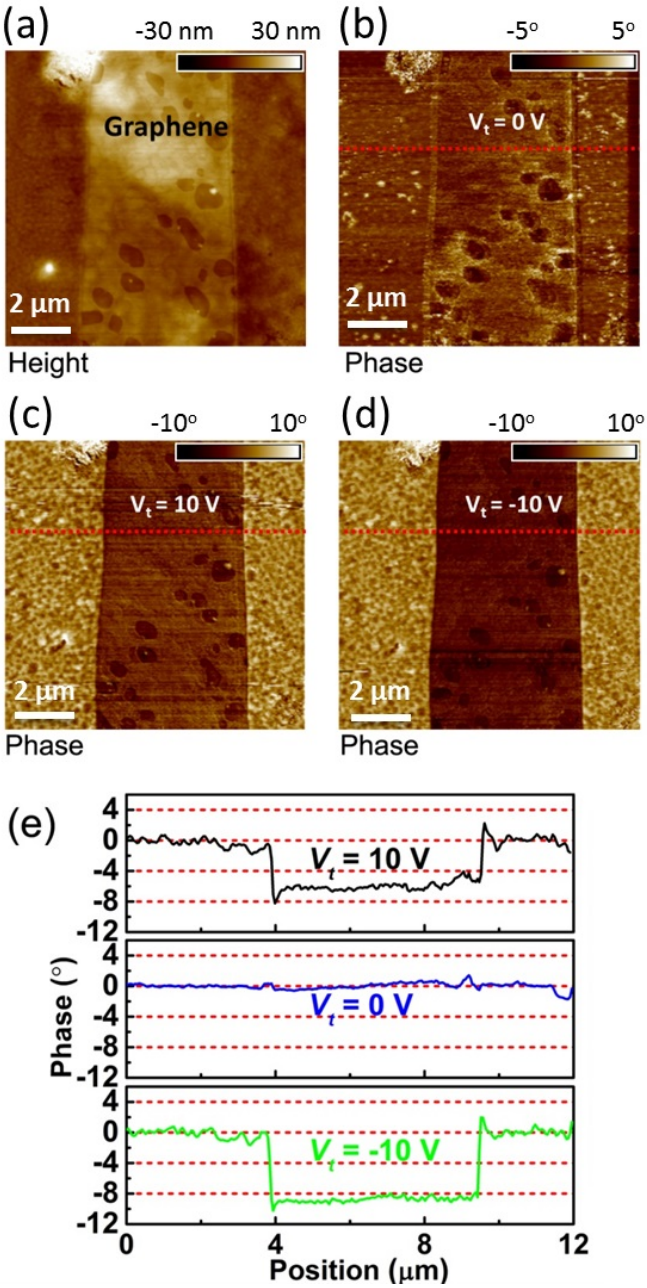

Figure 3.16: (a) Tapping-mode AFM, and (b) (d) EFM images of a few layer graphene on Cr_2O_3, for tip voltages of: (b) 0 V; (c) +10 V, and; (d) -10 V, respectively. (e) EFM phase plots along the red dashed lines in (b)-(c). Figure courtesy of Zhiyong Xiao of Dr. Xia Hong's group

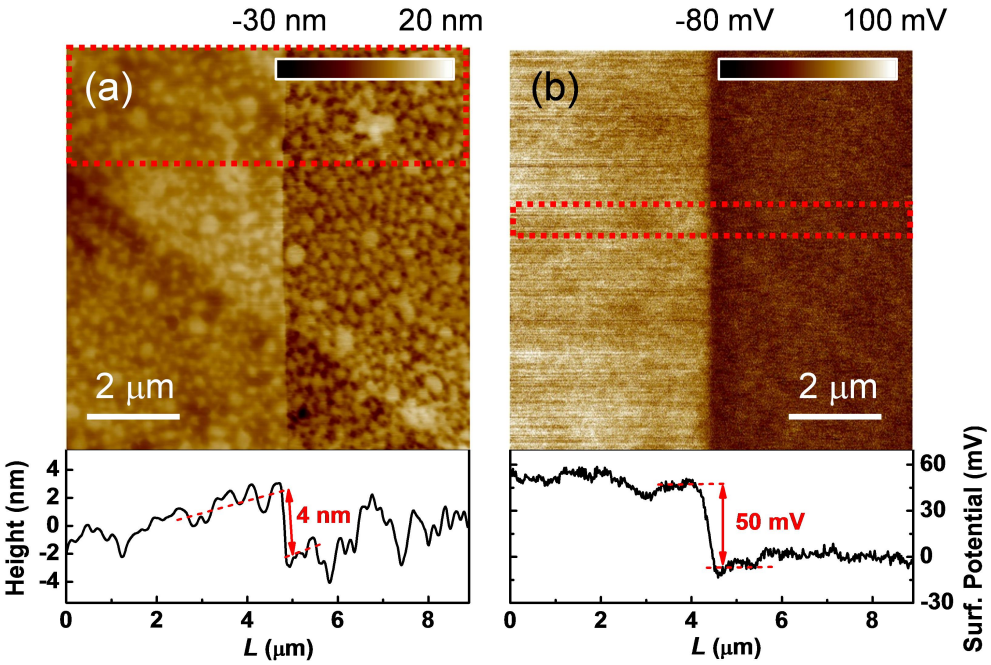

Figure 3.17: (a) Contact-mode AFM and (b) KPFM images of an expanded region in figure 3.16. The lower panels show the line profiles averaged in the red square regions. The graphene surface follows the morphology of the substrate but is much smoother. Figure courtesy of Zhiyong Xiao of Dr. Xia Hong's group

derstandable as the mobile carriers in graphene can respond to the AC modulation of the tip bias, while the chromia surface is insulating. A notable asymmetry in the EFM response of graphene has been observed between the tip biases of +10 V and -10 V, which indicates the presence of a non-zero doping for the graphene sample on $Cr_2O_3(0001)$. The larger shift (by $\sim$3 degrees) observed at -10 V suggests that the electrostatic interaction between the biased tip and graphene is enhanced at negative bias. This observation is consistent with a p-type doping of the graphene on $Cr_2O_3(0001)$ surface, where a negative (positive) tip bias would increase (suppress) local hole density. Similar asymmetry in the EFM phase shift is also observed for the puddled areas.

In figure 3.17(a), we show the contact-mode AFM of a close-up view of the area in figure 3.16(a). The RMS roughness of the few layer graphene is 2.1 nm, much smoother than the chromia surface (RMS roughness of 3.5 nm). By averaging a large area, we extracted an average height of 4 nm for the few layer graphene flake. We expect the actual sample thick-

ness to be much lower, as the graphene sheet does not fully conform to the rough Cr_2O_3 surface, which is evident from the signal line profile (figure 3.17(a)) and consistent with the different surface roughness extracted from the graphene and Cr_2O_3 surfaces. We then performed Kelvin probe force microscopy (KPFM) measurement in the same area. Figure 3.17(b) shows that the surface potential of the few layer graphene flake on Cr_2O_3(0001) is about 50 mV higher than that of the pristine Cr_2O_3. As KPFM probes the work function difference, we expect the surface potential of undoped graphene (work function of 4.6 eV [40]) should be 200 meV higher than Cr_2O_3 (work function of 4.8 eV [41]). The much lower surface potential difference confirms that the doping of the graphene is indeed p type, which decreases the Fermi level placement by 150 meV. The positive charge character in graphene is consistent, also, with what is predicted in a band-based model [42]. Using an effective hole mass of 0.1 m_e [43], where m_e is the free electron mass, we estimated the doping level to be $1.2 \times 10^{13}/cm^2$. Such a doping level is significantly higher than what is expected from ambient water or oxygen adsorbates [44], and can only originate from the interface interaction.

The induced doping in the few layer graphene is also reflected in the Raman spectra of this sample, as shown in figure 3.18. Figure 3.18 inset shows the fits to both G and 2D band. The G band peak position is about 1583.8 cm^{-1} and the full-width-half-maximum is about 15.7 cm^{-1}. The 2D band shape can be well described by two peaks, $2D_1$ and $2D_2$, which is the characteristic spectrum of few layer graphene [45, 46]. The corresponding peak positions of $2D_1$ and $2D_2$ are 2692.6 cm^{-1} and 2727.3 cm^{-1}, respectively. Both of the 2D peaks of the sample exhibit significant blue shift (by $5-10$ cm^{-1}) compared with few layer graphene on weakly interacting substrates [46]. Such a blue shift can only originate from a doping effect [44], and further confirms the interfacial charge transfer.

The p-doped charge transfer inferred above is moreover consistent with the results of our DFT calculations of monolayer graphene/chromia heterostructures (figure 3.19), which

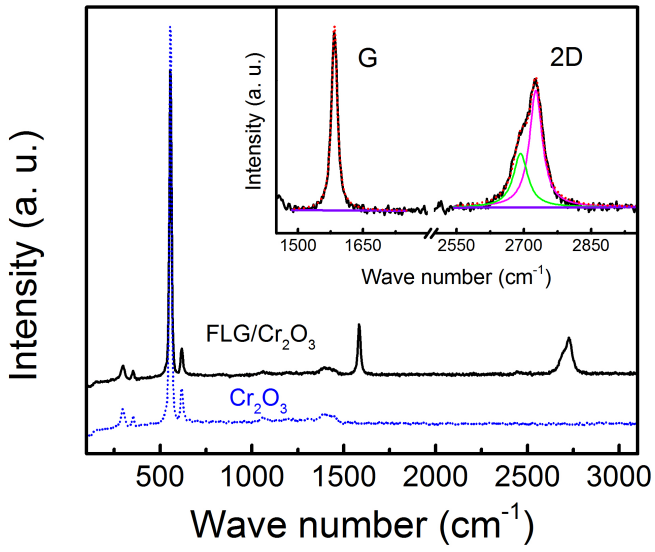

Figure 3.18: Raman spectra of pristine Cr_2O_3 and a few-layer graphene flake on Cr_2O_3. Inset: Lorenztian fits to the G and 2D bands of the FLG.

reveal a transfer of 0.0008 electrons per carbon atom, or a 2D density of $3 \times 10^{12}/cm^2$, from graphene to chromia. For monolayer graphene, this doping level corresponds to a Fermi level of 200 meV, which is comparable with that extracted from KPFM on few layer graphene. Several different trials, with different registrations of the graphene with respect to the chromia, have been considered, but do not significantly affect the result of the calculations. Although the charge transfer varies from carbon atom to carbon atom (figure 3.19), the band structure of the chromia is n-type, while the graphene adlayer is p-type, in the calculated band structure.

In spite of the relatively small charge transfer inferred above, the DFT calculations reveal that the boundary polarization of $Cr_2O_3(0001)$ induces a very high level of spin polarization in graphene. Figure 3.20 plots the density of states (DOS) of pristine chromia surface and chromia with a graphene overlayer. It is clear that the spin density is predominately determined by the Cr atoms in the chromia surface layer, and that the outmost Cr-layer retains spin-up ordering that leads to the graphene developing a net spin-up density.

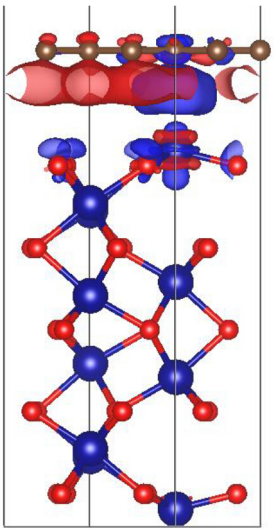

Figure 3.19: Charge densities difference for graphene/Cr_2O_3(0001). Electron loss is displayed in blue, and electron enrichment is displayed in red. The graphene layer, at the top, is indicated by the brown spheres. The small red spheres represent O atoms, large blue spheres represent Cr atoms, and brown spheres represent C atoms. The topmost Cr atoms (large blue spheres) are not clearly illustrated since they are surrounded by "clouds" of charge density differences. Figure courtesy of Dr. Lu Wang and Dr. Wai-Ning Mei.

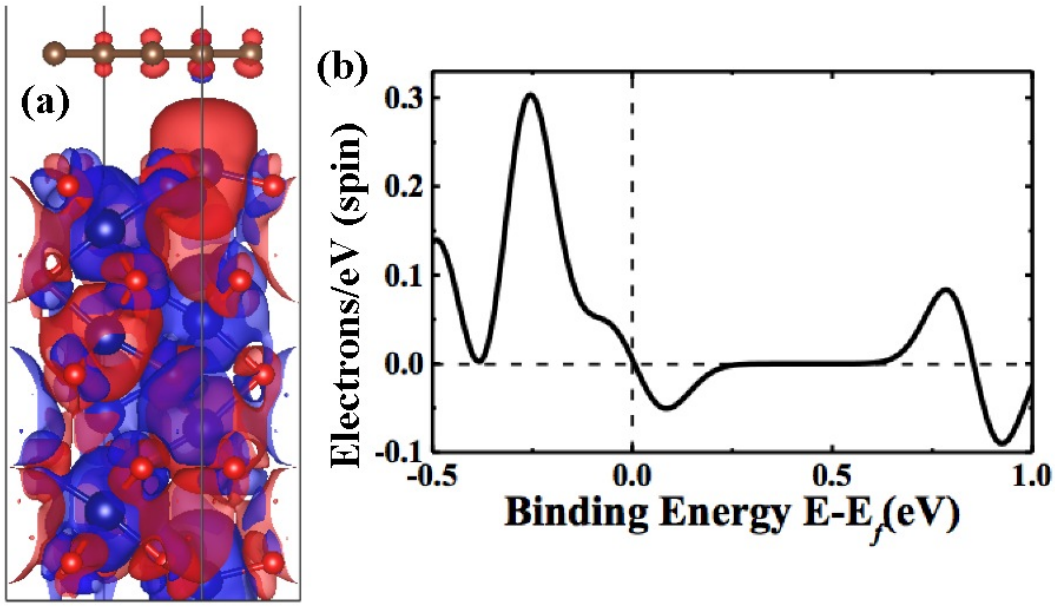

Figure 3.20: (a) the iso-surface plots of the spin density of graphene on Cr_2O_3(0001). Spin up and down density are displayed in red and blue, respectively. (b) Spin density of states differences around the Fermi level of graphene/Cr_2O_3(0001), respectively. The small red spheres represent O atoms, large blue spheres represent Cr atoms, and brown spheres represent C atoms. The topmost Cr atoms (large blue spheres) are not clearly illustrated since they are surrounded by "clouds" of spin densities. Figure courtesy of Dr. Lu Wang and Dr. Wai-Ning Mei.

This is further confirmed by plotting the density of states difference, and the band structure around the Fermi level for the system. This large carrier spin polarization makes graphene-on-chromia a promising material candidate for constructing magnetoelectric transistors.

In conclusion, the presence of induced p-type doping in graphene/few-layer graphene on Cr_2O_3(0001) has been confirmed by EFM and KPFM, and shown to be consistent with a band model of the doping polarity based on DFT. These results suggest that a large magnetoelectrically controlled magneto-resistance can be anticipated in transistor structures based on the graphene/Cr_2O_3(0001) system, a discovery that could be important for developing graphene-based spintronic applications.

References

[1] Lubbe M and Moritz W 2009 *J. Phys.: Condens. Matter* **21** 134010

[2] Rohr F, Baumer M, Freund H J, Mejias J A, Staemmler V, Muller S, Hammer L and Heinz K 1997 *Surf. Sci.* **372** L2917

[3] Rohr F, Baumer M, Freund H-J, Mejias J A, Staemmler V, Muller S, Hammer L and Heinz K 1997 *Surf. Sci.* **389** 391

[4] Gloege T, Meyerheim H L, Moritz W and Wolf D 1999 *Surf. Sci.* **441** L91723

[5] Bikondoa O, Moritz W, Torrelles X, Kim H J, Thornton G and Lindsay R 2010 *Phys. Rev. B* **81** 205439

[6] Rehbein C, Harrison N M and Wander A 1996 *Phys. Rev. B* **54** 1406670

[7] Rohrbach A, Hafner J and Kresse G 2004 *Phys. Rev. B* **70** 125426

[8] Lauter V, Ambaye H, Goyette R, Lee W-T H and Parizzi A 2009 *Physica B* **404** 2543

[9] Sears V F 1992 *Neutron News* **3** 2637

[10] Chen X et al 2015 *Mater. Chem. Phys.* **149150** 11323

[11] Clarke L J 1985 Surface CrystallographyAn Introduction to Low Energy Electron Diffraction (New York: Wiley)

[12] Tanuma S, Shiratori T, Kimura T, Goto K, Ichimura S and Powell C J 2005 *Surf. Interface Anal.* **37** 83345

[13] Coey J M D and Venkatesan M 2002 *J. Appl. Phys.* **91** 8345

[14] He X, Wang Y, Wu N, Caruso A N, Vescovo E, Belashchenko K D, Dowben P A and Binek C 2010 *Nature Mater.* **9** 57985

[15] Wu N, He X, Wysocki A, Lanke U, Komesu T, Belashchenko K D, Binek C and Dowben P A 2011 *Phys. Rev. Lett.* **106** 087202

[16] Rougemaille N and Schmid A K 2010 *Eur. Phys. J. Appl. Phys.* **50** 20101

[17] Chen X, Kazi H, Cao Y, Dong B, Pasquale F L, Colon Santana J A, Cao S, Welch R, Binek Ch, Enders A, Kelber J A and Dowben P A 2015 *Mater. Chem. Phys.* **14950** 11323

[18] Bikondoa O, Moritz W, Torrelles X, Kim H J, Thornton G and Lindsay R 2010 *Phys. Rev. B* **81** 205439

[19] Wysocki A L, Shi S and Belashchenko K D 2012 *Phys. Rev. B* **86** 165443

[20] Martin T J and Anderson J C 1966 *IEEE Trans. Magn.* **2** 446

[21] Mathon J and Bergmann G 1986 *J. Phys. F: Met. Phys.* **16** 887

[22] Mathon J 1986 *J. Phys. F: Met. Phys.* **16** L217

[23] Mathon J 1986 *J. Phys. F: Met. Phys.* **16** 669

[24] Lu Y M, Choi Y, Ortega C M, Cheng X M, Cai J W, Huang S Y, Sun L and Chien C L 2013 *Phys. Rev. Lett.* **110** 147207

[25] Kosub T, Kopte M, Radu F, Schmidt G and Makarov D 2015 *Phys. Rev. Lett.* **115** 097201

[26] Borisov P, Eimuller T, Fraile-Rodrguez A, Hochstrat A, Chen X and Kleemann W 2007 *J. Magn. Magn. Mater.* **310** 23135

[27] Toyoki K, Shiratsuchi Y, Nakamura T, Mitsumata C, Harimoto S, Takechi Y, Nishimura T, Nomural H and Nakatani R 2014 *Appl. Phys. Express* **7** 114201

[28] Shiratsuchi Y, Kotani Y, Yoshida S, Yoshikawa Y, Toyoki K, Kobane A, Nakatani R and Nakamura T 2015 *AIMS Mater. Sci.* **2** 48496

[29] Shiratsuchi Y. et al 2012 *Phys. Rev. Lett.* **109** 077202

[30] Echtenkamp W and Binek C 2013 *Phys. Rev. Lett.* **111** 187204

[31] Toyoki K, Shiratsuchi Y, Kobane A, Harimoto S, Onoue S, Nomura H and Nakatani R 2015 *J. Appl. Phys.* **117** 17D902

[32] Nozaki T, Oida M, Ashida T, Shimomura N, Shibata T and Sahashi M 2014 *Appl. Phys. Lett.* **105** 212406

[33] Suzuki M, Muraoka H, Inaba Y, Miyagawa H, Kawamura N, Shimatsu T, Maruyama H, Ishimatsu N, Isohama Y and Sonobe Y 2005 *Phys. Rev. B* **72** 054430

[34] Shiratsuchi Y, Murakami T, Endo Y and Yamamoto M 2005 *Japan. J. Appl. Phys.* **44** 8456

[35] Negulyaev N N, Stepanyuk V S, Bruno P, Diekhoner L, Wahl P and Kern K 2008 *Phys. Rev. B* **77** 125437

[36] Dastoor P C and Allison W 2001 *Phys. Rev. B* **64** 085414

[37] Bi C, Liu Y, Newhouse-Illige T, Xu M, Rosales M, Freeland J W, Mryasov O, Zhang S, te Velthuis S G E and Wang W G 2014 *Phys. Rev. Lett.* **113** 267202

[38] Dowben P A, Binek C and Nikonov D E 2016 The potential of nonvolatile magnetoelectric devices for spintronic applications Nanoscale Silicon Devices 2nd; edited by S Oda and D Ferry (London: Taylor and Francis) ch 11

[39] Kelber Jeffry, Binek Christian, Dowben Peter, Belashchenko Kirill, Magneto-electric voltage controlled spin transistors, U.S. Patent 9,379,232 B2; issued June 28, 2016.

[40] Matsumoto K, Frontiers of graphene and carbon nanotubes: devices and applications (Springer, 2015)

[41] Wilde M, Beauport I, Stuhl F, Al-Shamery K, and Freund H J 1999 *Phys. Rev. B* **59** 13401

[42] Shearer C J, Slattery A D, Stapleton A J, Shapter J G, and Gibson C T 2016 *Nanotechnology* **27** 125704

[43] Hong X, Posadas A, Zou K, Ahn C H, and Zhu J 2009 *Phys. Rev. Lett.* **102** 136808

[44] Ryu S, Liu L, Berciaud S, Yu Y J, Liu H, Kim P, Flynn G W, and Brus L E 2010 *Nano Lett.* **10** 4944

[45] Ferrari A C, Meyer J C, Scardaci V, Casiraghi C, Lazzeri M, Mauri F, Piscanec S, Jiang D, Novoselov K S, Roth S, and Geim A K 2006 *Phys. Rev. Lett.* **97** 187401

[46] Das A, Chakraborty B, and Sood A K 2008 *Bull Mater. Sci.* **31** 579

Chapter 4

Surface and Magnetism of Multiferroic Hexagonal $ReFeO_3$

4.1 The stability and surface termination of hexagonal $LuFeO_3$

From the point of view of applications, the surface termination and surface stability is of paramount importance in hexagonal $LuFeO_3$ (h-$LuFeO_3$). The surface termination affects the polarization of the surface and of the interface with other materials, which will have a significant influence on the voltage control of magnetization for magnetoelectric logic and memory device applications. Yet, the detailed structural and electronic properties at the interface between h-$LuFeO_3$ and the substrates or at the surface (the interface with vacuum) of the h-$LuFeO_3$ have been given little attention thus far [1-10].

We have investigated the structural and electronic properties of the surface and the stability of h-$LuFeO_3$ using angle-resolved X-ray photoemission spectroscopy (ARXPS), complemented by X-ray diffraction (XRD) and density functional theory (DFT). Given the surface sensitivity due to the short mean free path of the photoelectron, ARXPS has proven to be an effective approach to characterizing the surfaces of complex oxides. Based on the Lu 4f, Fe 2p and O 1s core level electronic structure, as well as DFT, we are able to show that the favored surface termination of h-$LuFeO_3$ is $Fe-O$ instead of $Lu-O_2$.

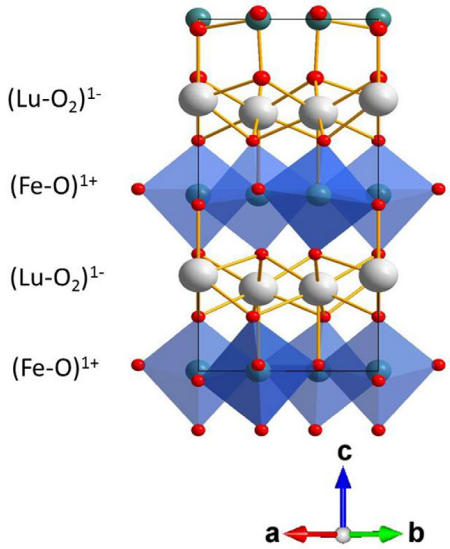

Figure 4.1: Unit cell of h-$LuFeO_3$ showing the charged Fe−O and Lu−O_2 layers. Figure courtesy of Dr. Xiaoshan Xu.

4.1.1 The nominal oxidation state of h-$LuFeO_3$

The structure of the h-$LuFeO_3$, stacking in the (0001) direction, is shown in figure 4.1. The surface of hexagonal lutetium ferrite (h-$LuFeO_3$) is fragile with respect to low-energy argon ion sputtering, and the surface composition and nominal valence state of the surface and near surface (selvage region) can be modified. The X-ray photoemission spectra for the Fe 2p, O 1s and Lu 4f core levels show significant differences after argon ion sputtering compared to as grown (pristine) sample, as seen in figure 4.2. These changes are particularly evident in the Fe 2p satellite photoemission features and Lu 4f shallow core level. The Fe 2p core level photoemission spectra not only contain the $2p_{3/2}$ and $2p_{1/2}$ but also three satellite peaks (labeled by the dashed lines A, B and C in figure 4.2 (a)) and excellent signatures of the nominal valence state of the iron in $LuFeO_3$. The peak position of the Fe 2p core level photoemission satellite features have been well studied for Fe^{2+}, Fe^{3+} and mixed valance state compounds [11-13]. In comparing our data with these prior studies, it is clear that for pristine h-$LuFeO_3$ thin films, the Fe 2p and satellite peaks are characteristic of a nominal Fe^{3+} valance, and as the features do not vary with emission angle, both

surface and bulk are in the nominal Fe^{3+} valance state. This changes after the sputtering or after the sputtering and annealing (to 400K in ultra-high vacuum) combination.

With sputtering, and even with post-annealing, the XPS spectra of Fe 2p and associated satellite peaks characteristic of a nominal Fe^{3+} valance develop the signatures of the characteristics of a nominal Fe^{2+} valance, as seen in figure 4.2 (a). In the transition from the nominal Fe^{3+} valence to Fe^{2+}, the relative binding energies of the Fe 2p satellite features move to the lower (smaller) binding energies, as do the main 2p core level photoemission features, as noted in prior studies of iron oxides [12, 13]. Accompanying the general shift to lower binding energies, the energy separation between the satellite peaks and the main Fe $2p_{3/2}$ core level photoemission peak also decreases. The XPS satellite peaks (labeled by C in figure 4.2 (a)) move closer, in apparent binding energy, to the Fe $2p_{3/2}$ core level feature. This energy separation between the multiplet features and the main Fe $2p_{3/2}$ and Fe $2p_{2/2}$ features, in XPS, is a signature of a change in the nominal valence of the iron [11-13]. These changes to the core level photoemission spectra indicate that the Fe local environment changes with Ar ion sputtering and annealing, and indeed is expected, since the oxygen deficiencies (oxygen depletion) can occur [12, 13]. The electron density around the Fe ion decreases so the binding energies for both the Fe 2p satellite and the main core level peak also decrease.

The experimental XPS Fe $2p_{3/2}$ core level line shape for h-$LuFeO_3$ may be even further fitted with the multiplet peaks of Gupta and Sen [14, 15] for both pristine surface of a nominal Fe^{3+} valence and the surface where defects were introduced by Ar^+ ion sputtering and annealed in ultra-high vacuum (UHV). This fitting of the $2p_{3/2}$ envelope by a detailed assignment of multiplets, as applied by Gupta and Sen to high spin Fe^{3+} compound [14, 15] is a tertiary indicator of the nominal Fe valence state. If the pristine h-$LuFeO_3$ is entirely Fe^{3+} in the surface region, then the multiplet fitting of Gupta and Sen should be consistent results with other iron compounds [11, 16]. In the spirit of multiplet fitting of Gupta and

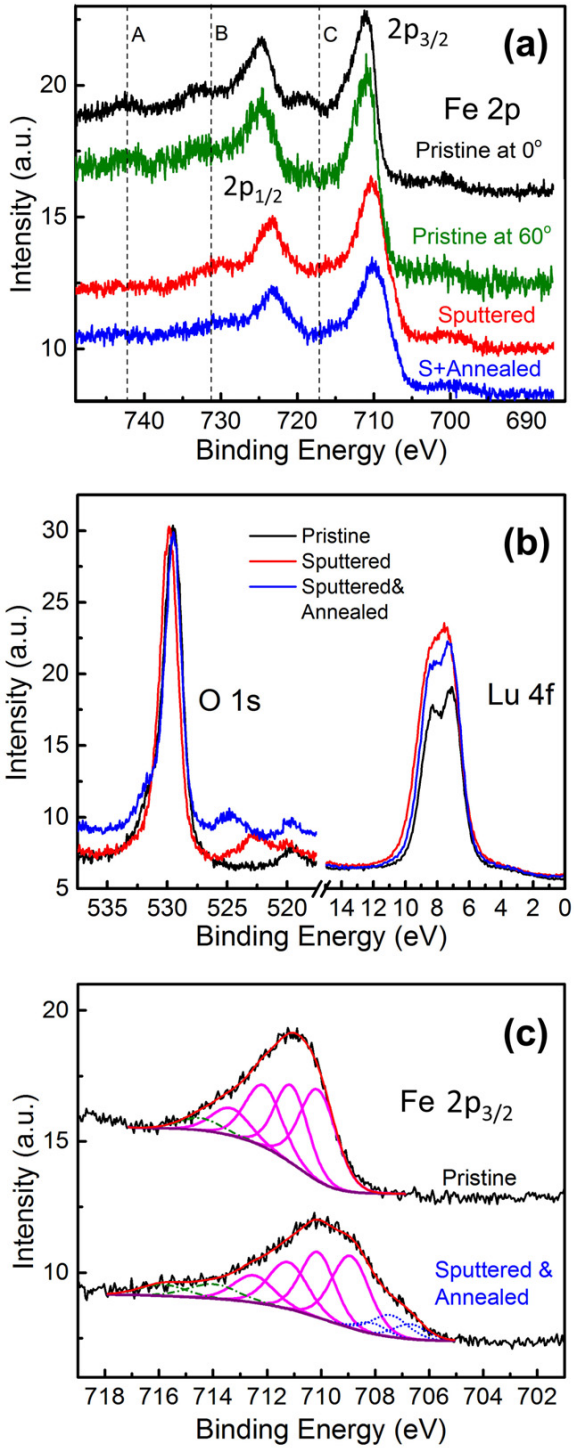

Figure 4.2: The core level electron structure of h-$LuFeO_3$ for pristine (both at 0° and 60° take-off angle), sputtered-only and sputtered and annealed samples taken at 0° take-off angle. (a) Fe 2p peaks with three satellite peaks labeled by A, B and C. (b) Lu 4f and O 1s core lines. (c) Gupta and Sen (GS) multiplets fittings for Fe $2p_{3/2}$ peaks with Shirley background indicated. The four multiplets from Fe^{3+} and three multiplets from Fe^{2+} were shown by bold (magenta) line and (blue) dot respectively. The (green) dashed line indicates the possible surface contribution. The fitting parameters were labeled in table 4.1. Binding energies are in terms of $E_F - E$.

Table 4.1: Comparison of the Gupta and Sen (GS) multiplet peak parameters (Fe $2p_{3/2}$) used to fit the Fe^{3+} and Fe^{2+} nominal valence core level spectra obtained in the compound h-$LuFeO_3$ (h-LFO) and other Fe (III, II) compounds.

Compound	Peak 1 (eV) [FWHM]	%	Peak 2 (eV) [FWHM]	%	ΔE (Peak2-Peak1) (eV)	Peak 3 (eV) [FWHM]	%	ΔE (Peak3-Peak2) (eV)	Peak 4 (eV) [FWHM]	%	ΔE (Peak4-Peak3) (eV)	Ref.
h-LFO(Fe^{3+})[a]	710.1[1.6d[b]]	36.4	711.1[1.4]	27.8	1.0	712.2[1.6]	24.4	1.1	713.4[1.7]	11.4	1.2	This work
h-LFO(Fe^{3+})[c]	708.9[1.6]	34.4	710.1[1.5[b]]	28.5	1.2	711.2[1.7]	23.2	1.1	712.5[1.7]	13.8	1.3	This work
Ave. Fe_2O_3[d]	709.8[1.1]	33.2	710.8[1.0]	30.6	1.0	711.6[0.8]	23.4	0.8	712.7[1.1]	12.9	1.1	[16]
Fe^{3+} GS multiplets		39.9		30.4	1.6		19.6	1.3		10.1	0.6	[11, 15]
h-LFO(Fe^{3+})[c]	706.7[1.4d]	30.3	707.5[1.6]	49.5	0.8	708.1[1.3[b]]	20.1	0.6				This work
FeO	708.4[1.4]	35.2	709.7[1.6]	43.7	1.3	710.9[1.6]	21.1	1.2				[11]
Fe^{2+} GS multiplets		36.1		46.4	1.4		17.5	1.6				[11, 15]

[a]The pristine sample which means as grown without any sputtering or annealing treatment.
[b]The full width at half maximum (FWHM) was constrained to the number indicated and for other features, the FWHM was obtained by fitting.
[c]Sample was sputtered and annealed and then Fe^{2+} peaks shown. The ratios for Fe^{2+} and Fe^{3+} were normalized to the corresponding GS multiplets, which means, for Fe^{3+} the area sum of peak $1-4$ was 100% and for Fe^{2+} the area sum of peak $1-3$ was 100%.
[d]In the original reference, the ratio was calculated for GS multiplets and also satellites. For the comparison, the area ratio was normalized for peak $1-4$, the GS multiplets only.

Sen [14, 15], the fittings of the peak positions and intensity contributions to the various multiplets, for the pristine sample, agrees with the expected Fe (III) compound multiplet configuration, as summarized in figure 4.2 (c) with the key fitting parameters listed in table 4.1. The only deviation from expectation is that the photoemission full width at half maximum (FWHM) for the various multiplet features is slightly larger than the typical values [11, 16]. Taken as a whole, the multiplet fine structure is a further reliable indicator that the iron of pristine surface is in the nominally pristine Fe^{3+} state. In a similar vein, for the surface following sputtering and annealing treatments, the fittings of the peak positions and intensity contributions to the various multiplets (figure 4.2 (c)) and the fit of the $2p_{3/2}$ envelope (figure 4.3 (a)) must include a Fe^{2+} component to agree with the multiplet fitting of Gupta and Sen (figure 4.2 (c) and table1).

The iron 2+, introduced by argon ion sputtering and annealing, is a result of defect creation. With more significant sputtering and higher annealing temperatures, the Fe 2p photoemission features peaks show increasingly stronger characteristic signatures of Fe^{2+} (labeled by Fe^{2+} dashed line in figure 4.3 (b)). While the characteristic signatures of Fe^{2+} in the photoemission spectra of h-$LuFeO_3$ are increasingly resolvable after annealing at 1000 K, the creation of oxygen vacancies is partially reversible. The intensity of the char-

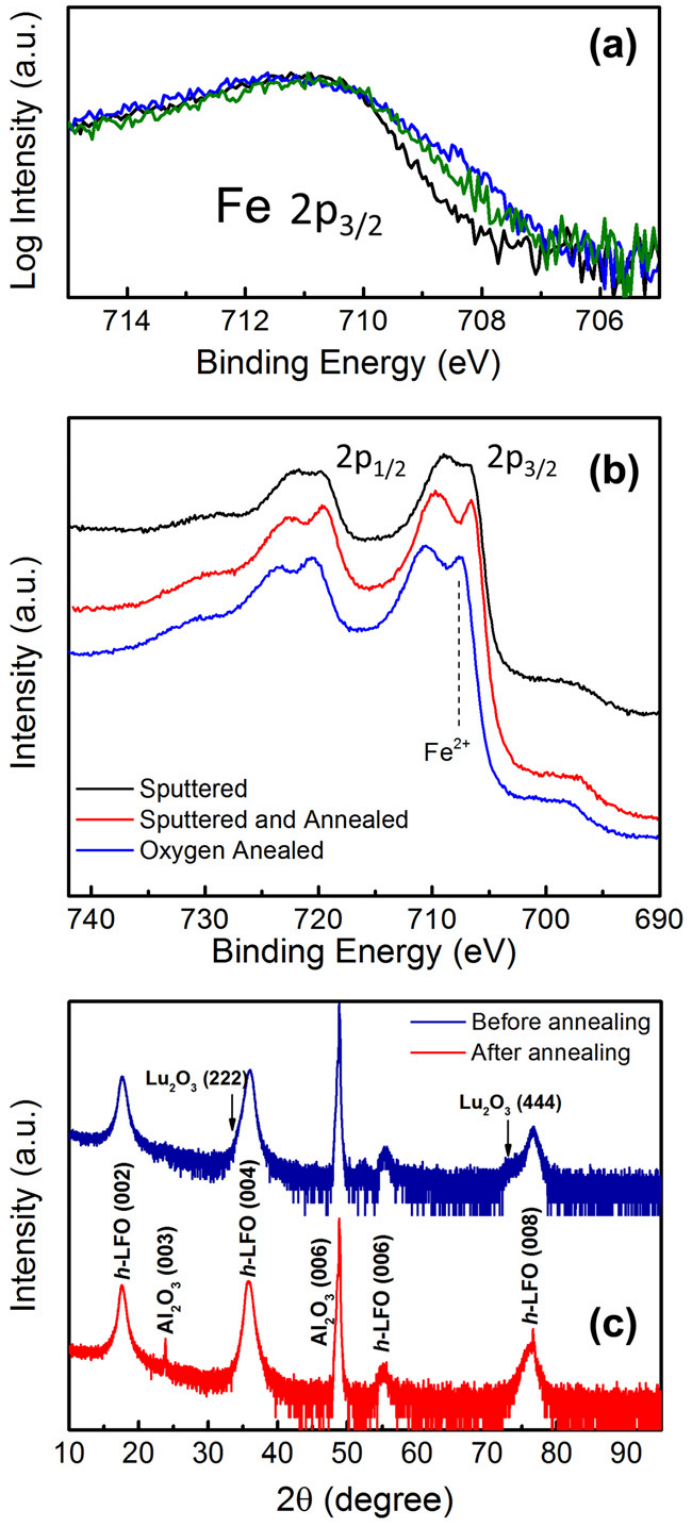

Figure 4.3: Comparisons of XPS Fe $2p_{3/2}$ spectra for pristine h-$LuFeO_3$ sample taken at 0° (black line), 60° (green line) take-off angles with respect to the surface normal and sputtered and annealed sample taken at 0° with respect to the surface normal (blue line) illustrating the broadening at around 709 eV where the signature of Fe^{2+} may exist in the spectra. (b) The shape and peak intensity changes in the Fe 2p spectra after intensive sputtering and annealing cycles, from top to bottom but followed by annealing in oxygen (bottom), with the spectra were taken at room temperature. The dashed line Fe^{2+} shows the Fe^{2+} components. (c) Recovery of the hexagonal phase indicated by XRD in the UHV treated sample after annealing in 1 atmosphere oxygen. The arrow indicates an impurity peak. Binding energies are in terms of $E_F - E$.

acteristic signatures of Fe^{2+}, in core level photoemission, decreases after the annealing in 1×108 Torr O_2 environment, as shown in figure 4.3 (b). The fragile nature of the h-$LuFeO_3$ stoichiometry is also evident in XRD, as shown in figure 4.3 (c). After multiple cycles of argon ion sputtering and UHV annealing, additional peaks appear in the XRD spectrum, indicating an impurity phases. The XRD spectrum obtained for a sample annealed in UHV treatment shows evidence of a minority phase (arrow in figure 4.3 (c)) other than h-$LuFeO_3$. This minority phase can be reduced or removed and converted back to the hexagonal phase after annealing in 1 atm O_2 at 600 °C (bottom of figure 4.3 (c)). The hexagonal phase, h-$LuFeO_3$, is stable as a thin film on $Al_2O_3(0001)$ substrates [1, 2], although the stable phase for bulk $LuFeO_3$ is orthorhombic, not hexagonal phase. The fact that the hexagonal phase can be recovered in the sputtered sample after annealing at high oxygen pressure (1 atm) at 600 C, is indicative that it is the hexagonal phase that is the stable phase of the epitaxial $LuFeO_3$ thin films on $Al_2O_3(0001)$ substrates and that the energy of the $Al_2O_3(0001)$/h-$LuFeO_3(0001)$ interface has lower energy than other possible interfaces [2].

4.1.2 Surface termination and possible reconstruction of h-$LuFeO_3$

Both DFT and angle-resolved X-ray photoemission (XPS) indicate that the $Fe-O$ surface termination is favored. As noted in the introduction, ARXPS may be used to estimate the surface composition of complex oxides by making use of the changes in the effective mean free path of the escaping photoelectron, which decreases with the increasing photoemission take-off angle. The variations in the photoemission Fe $2p_{3/2}$ to Lu 4f intensity ratio is plotted in figure 4.4. With the increasing take-off angle, the intensity ratio for pristine sample increases, indicating the Fe contribution is greater at the surface than Lu ions, suggesting that the surface is terminated by $Fe-O$ instead of $Lu-O_2$. As the sample is crystalline, forward scattering must be anticipated. This forward scattering in angle-resolved XPS contributes to the sharp rise in the Fe/Lu ratio at about $11^\circ-20^\circ$ off normal (forward scattering

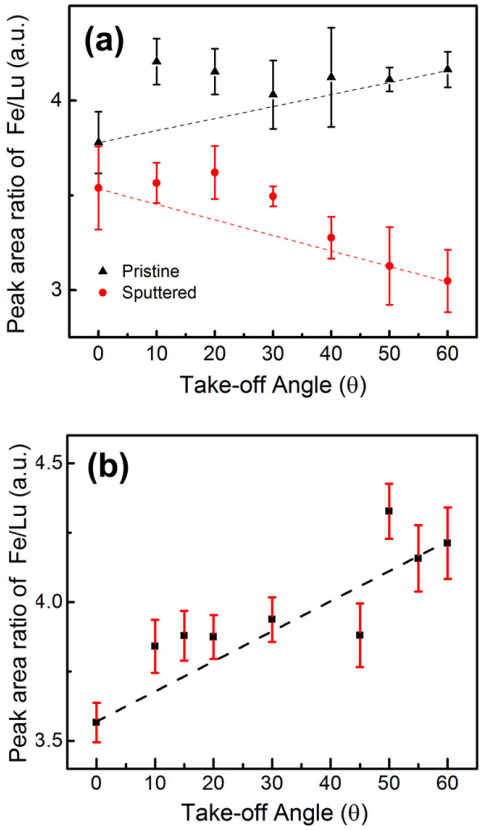

Figure 4.4: The XPS intensity (peak area) ratio of Fe $2p_{3/2}$ core level relative to the Lu 4f (the latter containing both $4f_{7/2}$ and $4f_{5/2}$ components), as a function of photoemission take-off angle with respect to the surface normal. The dashed lines are just meant as guide lines. (a) The (black) triangle and (red) spot shows the variation of the peak area ratios with take-off angle indicating Fe−O and Lu−O_2 surface termination for a pristine and sputtered surface respectively. (b) The XPS intensity (peak area) ratio of Fe $2p_{3/2}$ core level relative to the Lu 4f, an indication of a Fe−O termination for a separate sample.

is expected at about 16°).

After moderate argon ion sputtering, the rich Fe−O surface layer is removed and the underlayer exposed leading a Lu−O_2 termination of the surface of h-$LuFeO_3$. This is evident in the angle-resolved XPS data as a reduction of the Fe $2p_{3/2}$ to Lu 4f intensity ratio with increasing emission angle away from the surface normal, as clearly seen in figure 4.4. We find there is the relationship between the surface termination and the shape of the Lu 4f core level features. For the pristine sample (Fe−O terminated as discussed above), the Lu 4f is split in the photoemission spectra into the $4f_{7/2}$ and $4f_{5/2}$ spinorbit components, as shown in figure 4.2 (b). When the termination of the surface of h-$LuFeO_3$ is Lu−O_2, as

a result of argon ion sputtering, the shape of Lu 4f feature changes and the separation of the $4f_{7/2}$ and $4f_{5/2}$ components is almost not resolvable (figure 4.2 (b)). While the valency of the Lu 4f may not change, the local environment of Lu does, leading to a surface and bulk component for both the $4f_{7/2}$ and $4f_{5/2}$ [17]. There are the complications as while the electronic structure of a rare earth 4f state is generally regarded as a core level, and often thought not affected by the valence electron and/or crystal field, the rare earth 4f peaks lie close to Fermi level and seen to be part of the valence band [17] thus strongly influenced by the valence band and changes of crystal field. The changes to the Lu $4f_{7/2}$ (8.5 eV) and $4f_{5/2}$ (7.1 eV) XPS shallow core levels, in this latter context, are not surprising at all and consistent with prior work [17]. The Fe$-$O surface termination evident in angle-resolved photoemission is consistent with the predictions of our DFT calculations.

To investigate the surface composition, we calculated the surface grand potential for symmetric Lu$-O_2$ and Fe$-$O terminated slabs. We determined the region of the chemical potentials where $LuFeO_3$ is stable. This is displayed in figure 4.5 (b), where the shaded area of stable $LuFeO_3$ is bounded by formation of Fe_2O_3 and Lu_2O_3. At each point inside this region of stable $LuFeO_3$, we calculated the surface grand potential for the Lu$-O_2$ and Fe$-$O surfaces. The regions where the Lu$-O_2$ and Fe$-$O surface terminations have the lowest grand potential are shaded in red and blue respectively in figure 4.5 (a).

It can be seen from figure 4.5 (a) that except for lower oxidizing conditions, the Fe$-$O surface is unstable. The above consideration, however, does not take into account the tendency for the polar surfaces to reconstruct. The fact that both Lu$-O_2$ and Fe$-$O pristine surface terminations are charged means that they are unstable and thus highly susceptible to surface reconstructions. Theoretically, we consider a simple surface reconstruction that leads to a charge neutral surface. The (2×1) Fe$-$O surface with one iron vacancy ((2×1) Fe$-$O+V(1Fe)), and the (2×2) Lu$-O_2$ surface with three oxygen vacancies (2×2 Lu$-O_2$+V(3O)) are expected to be neutral based on their polar charges. Following the

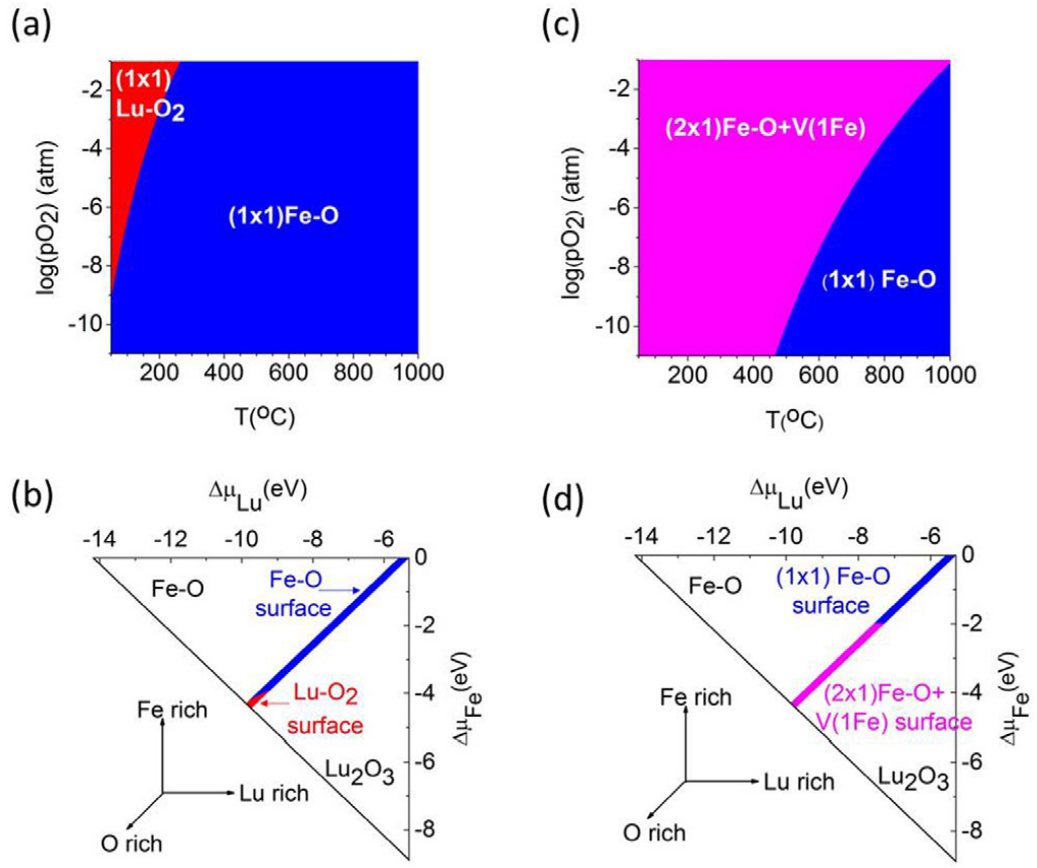

Figure 4.5: Results of theoretical calculations of the h-$LuFeO_3(0001)$ surface phase stability. Partial pressure (pO_2) temperature plot showing the stability conditions for the unreconstructed (1×1) Lu−O_2 and (1×1) Fe−O polar surfaces (a) and the reconstructed (2×1) Fe−O+V(1Fe) and (1×1) Fe−O non-polar surfaces (c); and their chemical potential representation of plot in (b) and (d), respectively. Figure courtesy of Dr. Tula Paudel of Dr. Evgeny Tsymbal's group.

method described above we calculated the grand potential for the reconstructed surfaces and plotted the surface phase stability diagrams in figure 4.5(c) and (d). It is evident that contrary to the results for the unreconstructed pristine surface, the Fe−O surface termination is stable over a broad range of temperatures and oxygen partial pressures (figure 4.5 (c)). In oxidizing/Fe poor conditions, formation of Fe vacancies is facile and a defective Fe−O surface is stable, whereas in reducing/Fe rich conditions Fe vacancy formation is energetically unfavorable and the unreconstructed Fe−O surface is stable. This means that the energy gain by polarity reduction in this case is smaller than that required to form Fe vacancy. The grand potential of (2×2) Lu−O_2+V(3O) is higher than (1×1) Fe−O even in

O poor area, and hence (1×1) Fe$-$O surface remains more stable. Thus, overall stability phase diagram now is covered by Fe$-$O surfaces(2×1) Fe O+V(1Fe) in the Fe poor/O rich conditions and (1×1) Fe$-$O surface in Fe rich/O poor conditions.

We find in all our experimental studies that the h-$LuFeO_3$(0001) basal face surface terminates in FeO, consistent with density functional theory calculations. The polar FeO surface is seen to be susceptible to reconstructions and vacancy formation, again in both experiment and theory, and this effect is much more dramatic under high temperature and ultra-high vacuum (UHV).

4.2 On the structural origin of the single-ion magnetic anisotropy in $LuFeO_3$

4.2.1 Introduction

In this section, we are concerned with the effect of the crystal structure on the magnetic anisotropy in antiferromagnetic $LuFeO_3$ in both hexagonal and orthorhombic phases. We attempt to understand the single-ion magnetic anisotropy in $LuFeO_3$, by studying the effect of the crystal structure on the orbital states, and the consequential effect on the spin states according to the spin-orbit coupling. To investigate the orbital states of Fe, we measured the electronic structures of $LuFeO_3$ using X-ray absorption spectroscopy (XAS); the results are consistent with the D_{3h} and O_h local symmetry of Fe sites in the hexagonal and orthorhombic $LuFeO_3$ respectively. More details of the orbital states were calculated according to the low temperature structure of $LuFeO_3$ (C_S and D_{2h} local symmetry for Fe sites in the hexagonal and orthorhombic structures respectively) using the multiplets theory [18]. The low temperature structure of h-$LuFeO_3$ was measured in this work using single-crystal X-ray diffractions, since it has not been reported. We found that the low local symmetry split the orbital states, generating preferred spin orientations of these states via spinorbit coupling. The magnetic anisotropy for the whole Fe^{3+} ion is then caused by the non-zero and uneven

occupancies of the spin-minority states due to the uneven hybridizations of these states to O 2p states. For orthorhombic $LuFeO_3$, the predicted easy axis for the spins is the shortest axis (a axis) after the D_{2h} distortion. For hexagonal $LuFeO_3$, the preferred spin orientation are in the intersection between the basal plane and the mirror plane of the C_S symmetry. Both predictions are consistent with the experimental observations [1].

4.2.2 Energy and spatial distribution of the orbital states measured using XAS

As the first step, we investigated the effects of the crystal structure on the orbital states of the metal ions (Fe and Lu), because the crystal structure affect the spin states of the magnetic ions by first changing their orbital states. XAS was employed to study the unoccupied orbital states (conduction band). The measured energy distribution (spectra shape) and spatial distribution (linear dichroism) of these orbital states are compared with the crystal field splitting and hybridization (with O 2p states) analyzed according to the crystal structure. The crystal structures and O K edge electronic structures are shown in figure 4.6

The absorption spectra as a function of X-ray energy with linearly polarized X-ray have been collected in the energy range 525 eV to 560 eV, as shown in figure 4.7. The energy range corresponds to the excitation of O 1s orbital to O 2p orbital (O K edge). The fact that the O 1s $\rightarrow$ O 2p excitations are clearly observed indicates significant hybridization between the metal (Fe and Lu) states and the oxygen states, making the effective occupation of the O 2p orbital different from the full $2p^6$ occupation. The presence of the O 1s $\rightarrow$ O 2p excitations also means that the electronic occupancy for the metal (Fe and Lu) sites is more complex than suggested by their nominal valence. Hence, the energies of the unoccupied oxygen orbitals actually correspond to the energies of the metal (Fe and Lu) states, as illustrated in figure 4.6 (c). Therefore, using the O K edge absorption spectra, one can infer the properties of the states that include metal (Fe and Lu) atomic contributions through hybridization [19]. In the case of $LuFeO_3$, the conduction (unoccupied) states

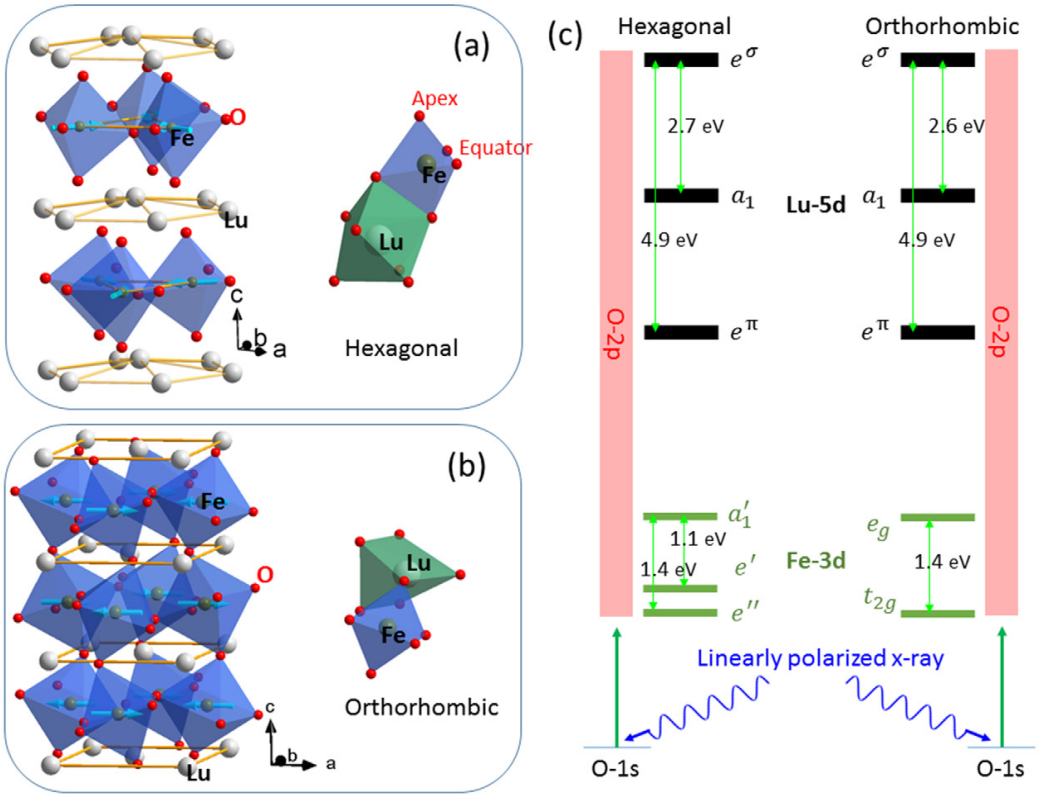

Figure 4.6: Lattice structures of hexagonal (a) and orthorhombic (b) $LuFeO_3$ as well as the local environments of the Lu and Fe sites. The thick arrows in (a) and (b) indicate the orientations of the spins. (c) Schematics of the O K edge excitation in $LuFeO_3$. The crystal-fieldsplitting energies are measured from the XAS spectra (see text). Figure courtesy of Dr. Xiaoshan Xu

include Fe 3d, Fe 4s, Lu 6s and Lu 5d. Among these states, Fe 3d and Lu 5d are expected to be more localized and the energy distributions are narrow enough to be resolved in the X-ray absorption spectra.

By comparing the observed spectra in this work to the previous studies on $YMnO_3$ and $LuFe_2O_4$ [19, 20] one can divide the absorption spectra into two parts that correspond to the contribution from Fe 3d and Lu 5d respectively, as shown in figure 4.7. For the spectra related to Fe 3d unoccupied states (conduction band), the differences between h-$LuFeO_3$ and o-$LuFeO_3$ are huge, not only in the spectra shape, but also in the dichroism. These differences appear to be correlated with the local environments of the Fe centers. As shown in figure 4.6 (b), in o-$LuFeO_3$, the local environment of the Fe centers are the

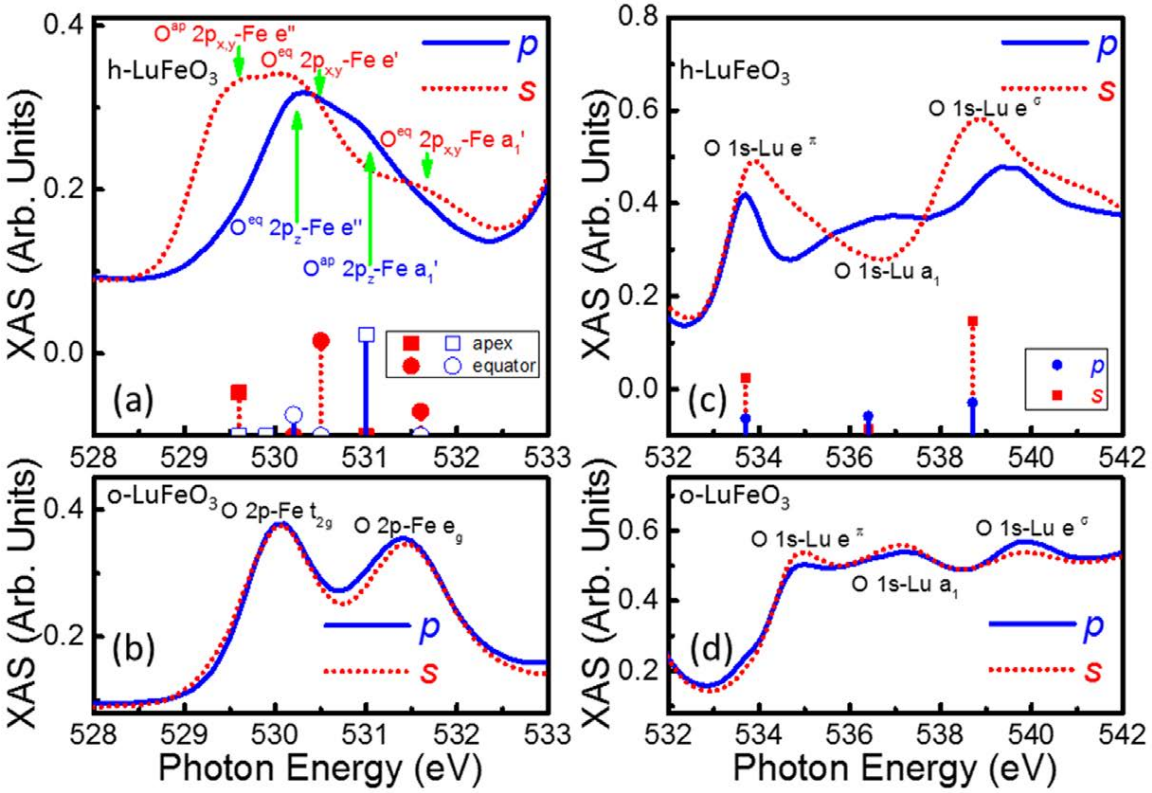

Figure 4.7: Absorption spectra corresponding to the O K edge with linearly polarized (*s*: in plane, *p*: out of plane) X-ray of $LuFeO_3$. The spectra corresponding to hybridization of the Fe 3d-O 2p are displayed for hexagonal (a) and orthorhombic (b) $LuFeO_3$. The spectra corresponding to hybridization of the Lu 5d-O 2p are displayed for hexagonal (c) and orthorhombic (d) $LuFeO_3$. The vertical lines (solid: p polarization, dashed: s polarization) in (a) and (c) are the results from the calculation of hybridization using the Harrisons method (see text). The arrows in (a) point to the energies of the excitations corresponding to the 5 hybridized states in figure 4. In (b)(d), the various hybridization components corresponding to the excitation peaks are labelled.

FeO_6 octahedra; no strong anisotropy or optical dichroism is expected due to the O_h local symmetry of the Fe-site. In contrast, as shown in figure 4.6 (a), the local environment of the Fe centers in h-$LuFeO_3$ is the FeO_5 trigonal bipyramid; the D_{3h} local symmetry suggests strong anisotropy and optical dichroism between the $a-b$ plane and the c axis. Below, we try to understand the spectra shape (energy distribution) in terms of the crystal field splitting, and to understand the dichroism (spatial distribution) in terms of the hybridization between the Fe 3d and O 2p states.

In h-$LuFeO_3$, the degeneracy of the Fe 3d states are broken by the crystal field from the 5 neighboring oxygen sites in the trigonal bipyramid FeO_5. Applying group theory

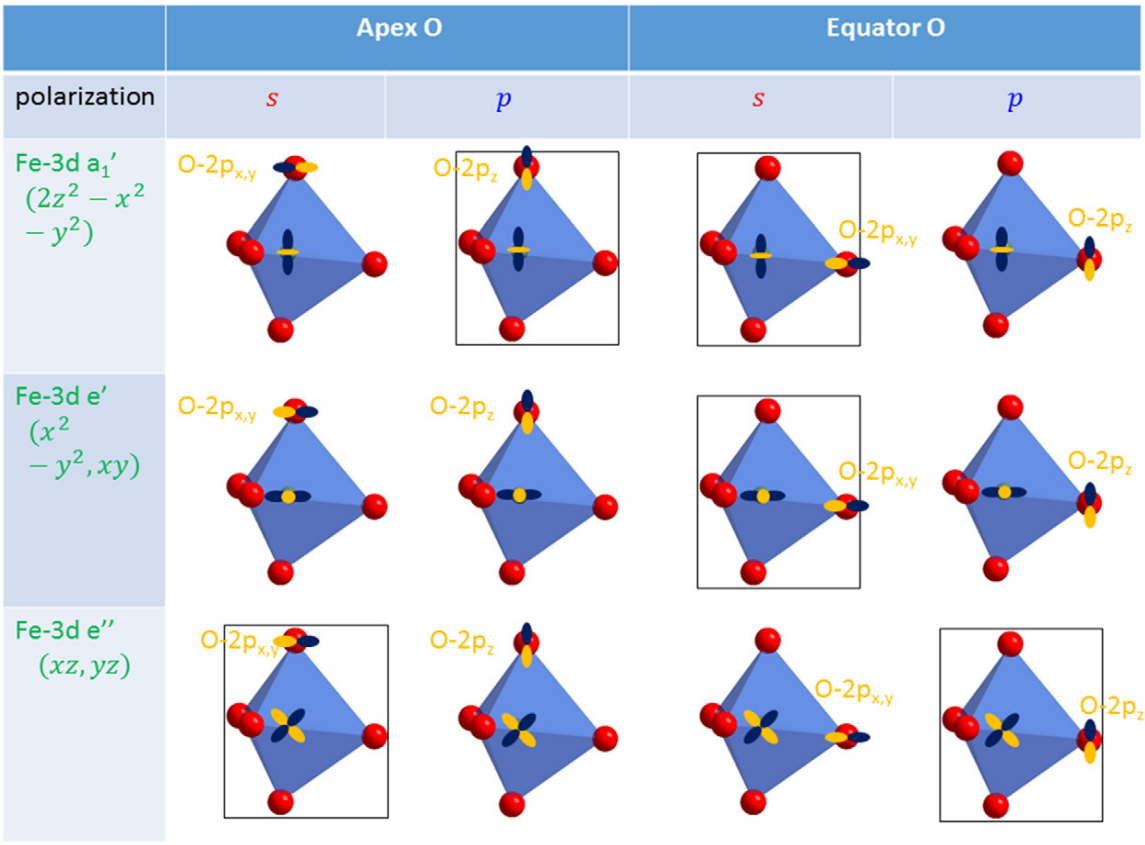

Figure 4.8: Model of hybridization between Fe 3d and O 2p illustrated using the relative position between the wave functions at different configurations. The configurations that correspond to significant hybridizations are boxed. Figure courtesy of Dr. Xiaoshan Xu

analysis, the D_{3h} local symmetry splits the 5 Fe 3d states into $a_1'(2z^2-x^2-y^2)$, $e'(x^2-y^2,xy)$, and $e''(xz,yz)$; the z direction is approximately parallel to the three fold rotational axis of FeO_5 and the c axis of the h-$LuFeO_3$ unit cell. Analysis using the multiplets model [18] provides the order of these states in energy as $E_{a_1'} > E_{e'} > E_{e''}$.

Due to the different spatial distribution of these crystal field states, their hybridization with O 2p orbitals are different, which is schematically shown in figure 4.8. For h-$LuFeO_3$, one needs to consider two inequivalent O sites: the apex O and the equator O, as shown in figure 4.6(a). The O 2p states are divided into p (along the c axis) and s (in the $a-b$ plane) to match the linearly polarized X-ray. By calculating the hybridization using Harrisons method [21], five non-zero scenarios can be identified, as depicted in figure 4.8 using

boxes. The hybridization can be appreciated by looking at the overlap of the wave function between the Fe 3d and O 2p orbitals. With linearly s (in plane) and p (out of plane) polarized incident X-rays, the excitation from O 1s to s and p branches of the O 2p states can be chosen respectively using their spatial distribution according to the optical selection rules. As shown in figure 4.8, one expects two peaks in the XAS with p polarization and three peaks in the XAS with s polarization, which matches the experimental observation in figure 4.7 (a) closely. The calculated hybridization strength, using the Harrisons method, is also displayed in figure 4.7 (a), which qualitatively agrees with the observed spectra intensity [6].

The analysis is more straightforward in o-$LuFeO_3$. The Fe 3d states are split into the well-known t_{2g} and e_g states. From the spectra in figure 4.7 (b), one finds that $E_{e_g} - E_{t_{2g}} = 1.4\ eV$ Again, no dichroism is expected due to the O_h local symmetry. Additionally, we found that presence of core hole does not change the ordering of the states. The electronic structure of the Lu 5d states may also be inferred from the corresponding spectra. Figures 4.7(c) and (d) display the XAS related to the Lu 5d states in h-$LuFeO_3$ and o-$LuFeO_3$. The local environments of Lu correspond to C_{3v} symmetry in both h-$LuFeO_3$ and o-$LuFeO_3$.

In h-$LuFeO_3$, the three-fold rotational axis of the LuO_7 local environment is aligned with the crystalline c axis, which is also the out-of-plane direction for the film samples. This definitive alignment between the high symmetric axis and the polarization of the X-ray generates dichroism, as observed in figure 4.7 (c). For the a_1 state, since the probability density of the wave function is mostly along the z axis, its hybridization with the equator O $2p_z$ is expected to be the largest, which corresponds to an enhancement with the p polarization in the XAS. In contrast, there is no overall alignment between the rotation axis of the LuO_6 moieties and the crystal axis, which greatlyreduces the dichroism effects, because of the averaging over various orientations. Nevertheless, the crystal field splitting feature does not vanish, as observed in the spectra in figure 4.7 (d).

Therefore, the energy and spatial distributions of the metal states (Fe and Lu) measured using XAS are consistent with the crystal field splitting and hybridization analyzed according to the crystal structural. Another key result from these XAS studies is the significant Fe 3d-O 2p hybridization. In $LuFeO_3$, the Fe 3d is nominally half-filled, corresponding full spin majority states and empty spin minority states. On the other hand, the significant Fe 3d-O 2p hybridization makes the effective occupancy of the spin minority states non-zero and uneven; this turns out to be critical for the single-ion magnetic anisotropy in $LuFeO_3$.

4.3 Phase separation in $LuFeO_3$ films

4.3.1 The observation of phase coexistence in $LuFeO_3$ films

In previous sections, section 4.1 and section 4.2, we systemically study the stability of hexagonal phase of $LuFeO_3$ films and both the electronic structure of hexagonal and orthorhombic phases have been investigated. In this section, we study the transition from the hexagonal to orthorhombic phase in h-$LuFeO_3$ films, grown on Al_2O_3 (0001) substrates. We found that in h-$LuFeO_3$ films, the transition occurs at around 1000 °C, with a coexistence of the two structural phases. The structural phase separation was observed on the micrometer scale; the boundaries between the two phases are aligned with the crystal planes of the h-$LuFeO_3$ phase. These findings suggest a minimal stability problem of h-$LuFeO_3$ films for application, and a self-organization of the sharp hexagonal/orthorhombic interface that involves a strong magnetic order (o-$LuFeO_3$, $T_N = 620$ K) and a strong ferroelectric order (h-$LuFeO_3$, $T_C = 1050$ K).

By annealing the samples at higher temperatures, we found that the transition starts at about 1000 °C, with clear indications of phase coexistence. Figure 4.9 displays the XRD pattern of the h-$LuFeO_3$ film right after the growth (as-grown) and after being annealed at different temperatures (T_A). Here we use the pseudo cubic unit cell for indexing the o-

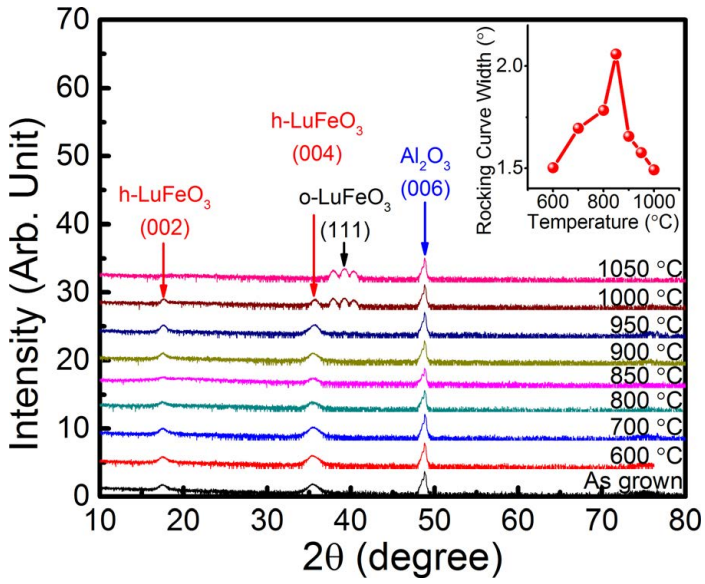

Figure 4.9: The2θ X-ray diffraction spectra for a 40 nm thick h-$LuFeO_3$ film grown on Al_2O_3, after being annealed at the stated temperatures. The inset is the rocking curve width of the h-$LuFeO_3$ (004) peak, as a functional of the annealing temperature TA. The o-$LuFeO_3$ (111) peaks are labeled using the pseudo cubic indices. In orthorhombic structure, the (111) peak is, in fact, split into three peaks. Figure courtesy of Kishan Sinha of Dr. Xiaoshan Xu's group

$LuFeO_3$ diffraction peaks. The film appears to be stable at least up to 700 °C, because the X-ray diffraction patterns are characteristic of the XRD for the as-grown h-$LuFeO_3$ film. This is consistent with our previous result that impurity phase generated at the surface by sputtering may be converted back to the h-$LuFeO_3$ phase, by annealing the sample at 600 °C. Upon increasing TA above 700 °C, the XRD intensity of the h-$LuFeO_3$ (002) and (004) peaks decreases, and reaches a minimum at $T_A = 850$ °C, but then increases until diminishing again in the region of 1000 °C, only to disappear at slightly higher temperature of $T_A = 1050$ °C. The characteristic XRD features of o-$LuFeO_3$ start to appear at $T_A = 1000\ ^\circ C$, at a temperature where the h-$LuFeO_3$ XRD peaks are still present. Because we use the pseudo cubic unit cell for indexing the o-$LuFeO_3$ diffraction peaks, the (111) peak actually corresponds to three different peaks in orthorhombic structure, as seen in figure 4.9

These results suggest the following scenario for the transition from the h-$LuFeO_3$ phase to the o-$LuFeO_3$ phase. At about 800 ° C, conversion to o-$LuFeO_3$ phase occurs locally, but only as structural fluctuations. We posit that in the region of 800 ° C, the interfacial

energy between the h-$LuFeO_3$ phase and the o-$LuFeO_3$ phase generates a large energy barrier to the nucleation of o-$LuFeO_3$ domains. Thus, no indication of o-$LuFeO_3$ phase can be clearly observed in the XRD of the $LuFeO_3$ thin films when quenched back to room temperature, although it is clear that defects and/or dislocations frozen into the h-$LuFeO_3$ thin film degrade the XRD peak intensities dramatically. At higher temperature (1000 $^\circ$ C), the thermal energy is large enough to overcome the energy barrier for nucleation of the o-$LuFeO_3$ phase; this leads to the separation of the two structural phases into large structural domains. The defects previously frozen into the h-$LuFeO_3$ thin film are now annealed out. As a result, the diffractions signatures of both the hexagonal and orthorhombic phases are now evident.

This scenario is also consistent with the dependence of the rocking curve width of the h-$LuFeO_3$ (004) peak on T_A. As shown in figure 4.9 inset, the rocking curve width reaches a maximum at $T_A = 850^\circ$C, indicating that the in-plane correlation of the atomic positions is at a minimum, which agrees with peak intensity minimum at $T_A = 850^\circ$C The coexistence of the h-$LuFeO_3$ phase and the o- $LuFeO_3$ phase indicates that the transition from the h-$LuFeO_3$ phase to the o-$LuFeO_3$ phase is first order, due to the difference between the densities of the two phases. To verify the existence of the phase separation in real space, and to probe the length scale of the phase separation, we employed atomic force microscopy and X-PEEM on another sample ($\sim$ 10 nm) rather than the sample of greater thickness (and thus more suitable for XRD).

Figure 4.10(a) presents the X-ray absorption spectra at Fe L_3 and L_2 edges for h-$LuFeO_3$ and o-$LuFeO_3$ using linearly polarized X-rays. In hexagonal structure, Fe 3d states split into three irreducible representations e'', e' and a_1' [6]. As shown in figure 4.10(a), for h-$LuFeO_3$, the XAS e' peak (at about 709.5 eV) will only be present with s polarization (i.e., with in-plane linearly polarized light), due to the applicable spectroscopic selection rules, as we discussed in section 4.2. For o-$LuFeO_3$, the absorption spectra always show two

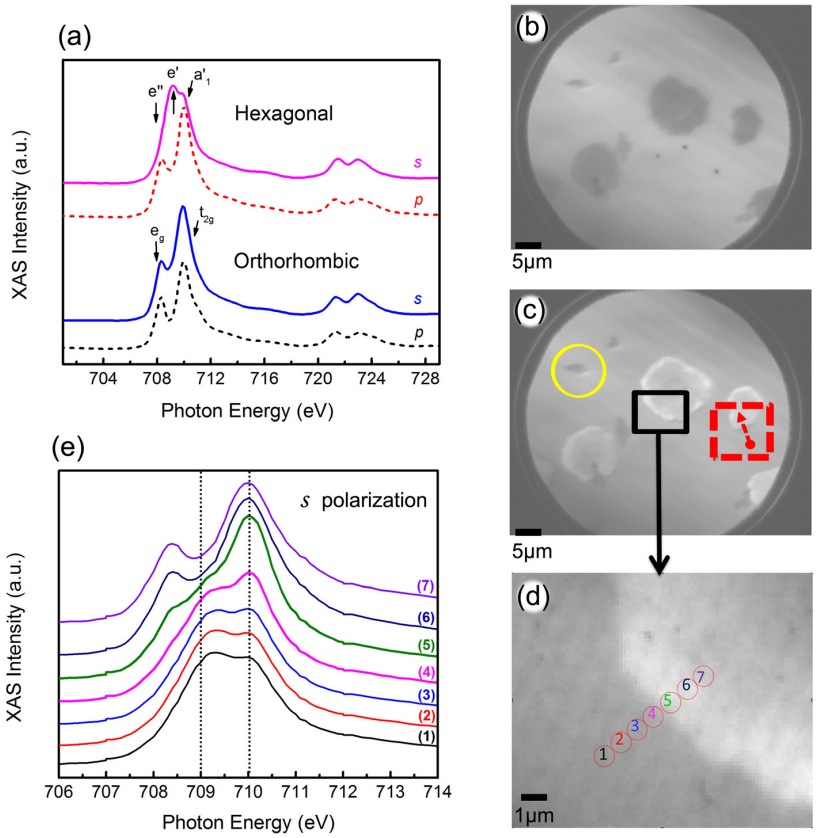

Figure 4.10: The X-ray absorption spectra at Fe L_3 and L_2 edges and the associated X-PEEM images for a $\sim$ 10 nm thick $LuFeO_3$ film grown on Al_2O_3. (a) The X-ray absorption spectra with s and p polarization for both h-$LuFeO_3$ and o-$LuFeO_3$. The PEEMimage in a 50 μm field-of-view at 709 eV (b) and 710 eV (c) taken using s-polarized X-rays. The (yellow) circled region shows the morphological defects in the h-$LuFeO_3$ film. The (red) dashed boxed region with arrow shows the starting point and direction of five oxygen K edge spectra illustrated in figure 4.11. The (black) boxed region in (c) was magnified into (d). (e) XAS obtained corresponding to the seven circled positions in (d); the dashed lines in (e) indicate the energy position of X-PEEM images taken at 709 eV (b) and 710 eV (c).

peaks, in the region of 708 to 712 eV, corresponding to the e_g and t_{2g} crystal field states, independent of polarization of X-ray[6]. Therefore, there is a clear correlation between lattice structure and X-ray absorption spectra in $LuFeO_3$. In particular, with *s*-polarized X-ray, the difference between the absorption spectra of h-$LuFeO_3$ and o-$LuFeO_3$ is significant, an aid for distinguishing the two structural phases.

We have used the large contrast, obtained in X-PEEM, to distinguishing the structural phases using their corresponding difference in electronic structures. Figure 4.10(b) shows an X-PEEM image, in a 50 μm field of view, taken at photon energy of 709 eV using

s-polarized X-rays. The contrast in the image can be identified as having an origin in the XAS spectroscopic differences of h-$LuFeO_3$ and o-$LuFeO_3$ (figure 4.10(a)). The h-$LuFeO_3$ phase is expected to have higher X-ray absorption at 709 eV with s-polarized X-ray, corresponding to a brighter color (the background) in figure 4.10(b). The dark island is the o-$LuFeO_3$ phase since the absorption is a local minimum. At 710 eV, the dark islands of the o- $LuFeO_3$ phase turn to bright as shown in figure 4.10(c) since the t_{2g} peak of the o-$LuFeO_3$ phase dominates at 710 eV. To better distinguish the structural phases of $LuFeO_3$, we plot the absorption spectra (figure 4.10 (e)), generated with s-polarized X-rays, along a sequence of positions, as shown in the X-PEEM image of figure 4.10(d). The spectra measured at position (7) are consistent with that of the o-$LuFeO_3$ phase, while the spectra measured at position (1) are consistent with that from the h-$LuFeO_3$ phase. A rapid change in the X-ray absorption spectra is observed between position (4) and (5), indicating a sharp structural interface.

The evidence of structural phase separation is also observed in the spectra that correspond to excitation from the O K edge. Figure 4.11 shows five X-ray absorption spectra at O K edge for both *s* and *p* polarization from sample region indicated in the dashed box in figure 4.10(c) (along the arrow of figure 4.10(c)). The spectra measured in the bright region in figure 4.10(c) indicate an o-$LuFeO_3$ electronic structure, while the spectra measured in the gray region indicate the h-$LuFeO_3$ electronic structure as discussed extensively in section 4.2 The transition between the two structural domains is illustrated by spectra (2)(4) in figure 4.11. This is the peak evolution observed at oxygen absorption edge.

In order to visualize more details of the h-$LuFeO_3$/ o-$LuFeO_3$ interface, we scanned the surface morphology using atomic force microscopy on the thin sample used for the XAS studies, as shown in figure 4.12. There appear to be at least two different regions in the film: one flat and higher (with the surface closer to the tip) and the other part more poorly defined, much rougher. The flatter regions are from the original h-$LuFeO_3$ phase

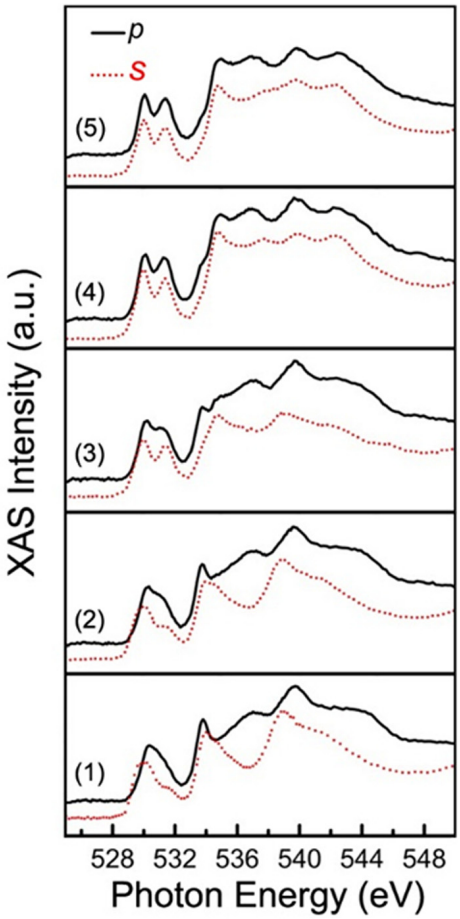

Figure 4.11: Five X-ray absorption spectra at O K edge starting from label (1) to (5) picked in the region indicated in figure 4.10 (c) as the (red) dashed box.

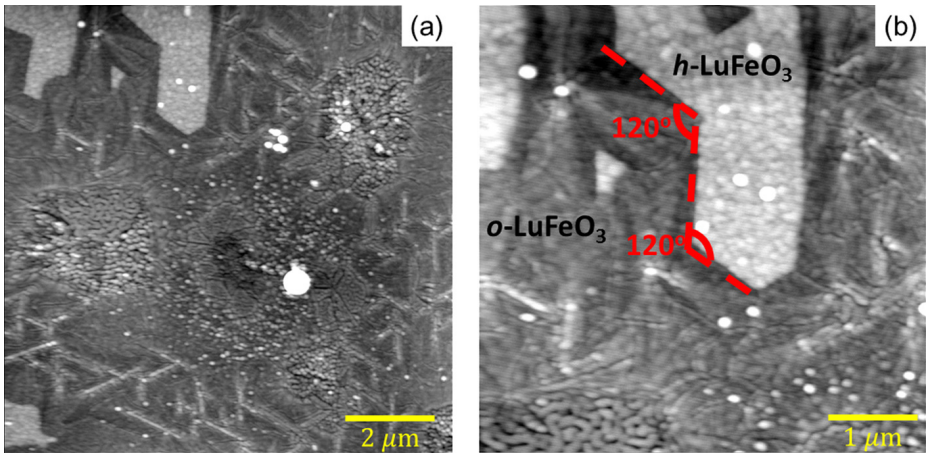

Figure 4.12: The atomic force microscopy (AFM) images illustrating the phase separation in a 10 nm thick $LuFeO_3$ film grown on Al_2O_3. (a) The AFM image of a 10μm $\times 10\mu$m sample area. (b) The image of a 5μm $\times 5\mu$m sample area. The dashed (red) line in (b) shows the angle of 120 degree at boundary between hexagonal and orthorhombic phases. Figure courtesy of Kishan Sinha of Dr. Xiaoshan Xu's group

film, while the rougher regions result from part of the film transformed into the o-$LuFeO_3$ phase. Figure 4.12(b) shows well-defined steps (boundaries) separating the h-$LuFeO_3$ and o-$LuFeO_3$ phases (10 nm high). The angles between these boundaries are about 120° (illustrated by the dashed line in figure 4.12(b)). The boundary between the two structural phases appears to have a tendency to align with the crystal planes of the h-$LuFeO_3$ phase. Our results indicate that the critical thickness for a stable h-$LuFeO_3$ phase on Al_2O_3 is actually smaller than 10 nm. The large interfacial energy at the boundary between the two $LuFeO_3$ phases appears the key to forming the large structural domains and the phase separation in $LuFeO_3$. The streaks visible in the images, in the region of o-$LuFeO_3$, are also about 10 nm in height; they occur at relative angles of 60° and are indicative of spatial movement of the structural domain wall, likely leaving defects in large number in specific locations to promote strain relief. We have shown that the h-$LuFeO_3$(001)/Al_2O_3(0001) film is metastable even for a film thickness of 10 nm. On the other hand, the irreversible, 1st order transition from the h-$LuFeO_3$ phase to the o-$LuFeO_3$ phase requires an annealing temperature as high as 1000 °C, due to the large energy barrier to form the h-$LuFeO_3$/o-$LuFeO_3$ interface, suggesting no practical instability problems to retaining h-$LuFeO_3$, once grown, under normal (ambient) conditions. An important implication is that the previously measured ferroelectric to paraelectric transition at about 1050 K [1] is not supposed to be affected by the instability significantly. Nevertheless, future investigations on the properties of h-$LuFeO_3$ films at elevated temperature need to be watchful of the emerging o-$LuFeO_3$ phase. The observation of the sharp, well-aligned boundaries between the hexagonal and orthorhombic phases, in a micrometer length scale, suggests the possibility of fabricating junctions between the two phases by self-organization, to better exploit this multiferroic h-$LuFeO_3$/o-$LuFeO_3$ (ferroelectric and antiferromagnetic) interface for nonvolatile magnetoelectric devices for spintronic applications.

4.4 Electronic structure in multiferroic hexagonal $YbFeO_3$

4.4.1 Introduction

In previous sections, we studied the lattice structures and electronic structures of hexagonal and orthorhombic $LuFeO_3$. Lu^{3+} is non magnetic in $LuFeO_3$, however, if we replace Lu atom with Yb in hexagonal phase, the Yb^{3+} is magnetic and it will introduce more interesting physics with respect to magnetism. Clearly, the structure of h-$YbFeO_3$ are almost the same to h-$LuFeO_3$.

In h-$YbFeO_3$, the Fe$-$Fe interaction is expected to dominate the framework of themagnetic ordering. However, the Yb-Fe interaction is weaker but sufficient enough to partially align the moment on Yb and contribute to the total magnetization. Indeed, an enhancement of magnetization of h-$YbFeO_3$, compared with that in h-$LuFeO_3$ has been observed previously [1, 8, 22, 23].

In this section, we study the magnetic interaction between rare-earth and transition-metal ions by measuring the magnetization of the rare-earth and transition-metal ions separately using an element-specific method in hexagonal $YbFeO_3$.

The Yb-Fe interaction could, in principle, align or antialign the moments of Fe and Yb. At the compensation temperature, the magnetization of Fe and Yb cancel, and an indication of this was observed previously at about 80 K [23]. On the other hand, direct observation of antialignment between the Fe and Yb magnetization is still lacking. In addition, the previously reported large magnetization (about 3 μB/f.u.) [23] at low temperature is more consistent with a free Yb^{3+}, but unexpected when considering the effect of the crystal field generated by the local environment. The crystal field could significantly change the effective magnetic moment and the magnetic anisotropy at low temperature.

To elucidate the Yb-Fe interaction and the magnetic moment of Yb, we have studied the electronic structure of h-$YbFeO_3$ using X-ray absorption spectroscopy (XAS) and X-

ray photoemission spectroscopy (XPS), and we measured the magnetization of Fe and Yb separately using X-ray magnetic circular dichroism (XMCD). We have found a large exchange field (17 kOe) on Yb, while the magnetic moment of Yb is significantly reduced from the value of a free ion. The mixed valence of Yb was investigated and found only at the surface of samples grown in a reducing environment, suggesting a minimal effect on the magnetism of h-$YbFeO_3$.

4.4.2 Crystal structure and local environment of Fe

To verify the structure and phases of the epitaxial films, we carried out X-ray diffraction, electron diffraction, and X-ray spectroscopy measurements. Figure 4.13(a) shows the X-ray diffraction (θ - 2θ scan) of h-$YbFeO_3$/YSZ films. No additional peak other than those expected for h-$YbFeO_3$ and the substrate is visible in this large-range scan, indicating no impurity phases. As shown in figure 4.13(b), RHEED images show diffraction streaks consistent with a flat surface and the structure of h-$YbFeO_3$ [1].

The X-ray absorption spectra provided further confirmation of the local structure of Fe, from the Fe L edge spectra taken with a linearly polarized X-ray. The local environment of Fe in h-$YbFeO_3$ is a trigonal bipyramid, with two apex O atoms (top and bottom) and three equator O atoms (in the Fe layer) as shown in figure 4.14(a) inset. This structure makes the out-of-plane direction (along the c axis) and the in-plane direction (in the $a-b$ plane) two distinct crystalline directions. Using a linearly polarized X-ray, we measured the absorption spectra at the Fe L edge, as illustrated in figure 4.14(b). As shown in figure 4.14(a), the spectrum with an s-polarized X-ray (E vector in the $a-b$ plane) and that with a p-polarized X-ray (E vector along the c axis) show an obvious contrast, consistent with the large structural anisotropy. The spectra and linear dichroism in figure 4.14(a) match those observed previously for h-$LuFeO_3$ as we discussed in section 4.2, confirming that the local environments of the FeO_5 moiety in the two materials are almost identical.

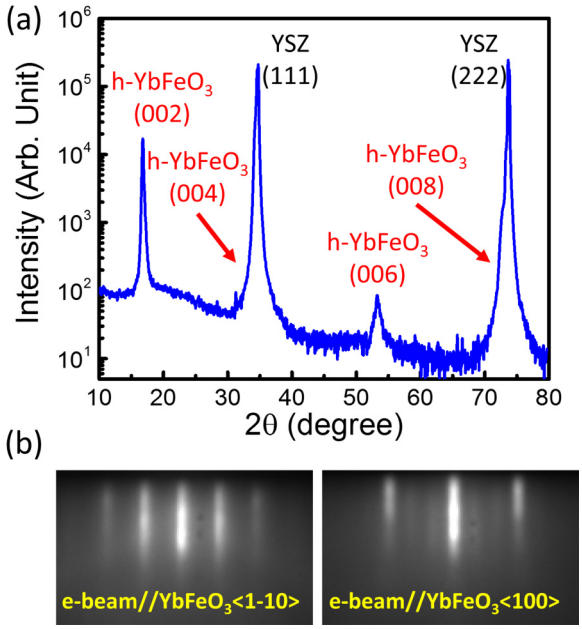

Figure 4.13: (a) -2 X-ray diffraction measurement of an h-$YbFeO_3$ film grown on yttrium-stabilized zirconia (YSZ). (b) RHEED patterns of an h-$YbFeO_3$ film with electron beam along the 1-10 and 100 directions. Figure courtesy of Dr. Xiaoshan Xu's group

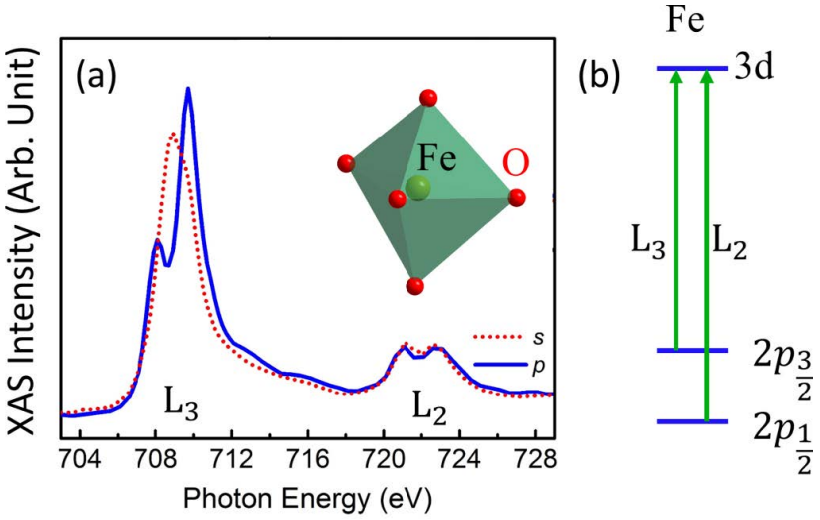

Figure 4.14: (a) X-ray absorption spectra at the Fe L edge, measured using a linearly polarized X-ray. Inset: the FeO_5 local environment. (b) Schematic illustration of the L2 and L3 excitation.

4.4.3 The electronic structure of Yb

While the electronic structure of Fe in h-$LuFeO_3$ and h-$YbFeO_3$ are superficially similar, the electronic structure of Yb^{3+} is expected to be different from that of Lu^{3+} by the presence of one fewer 4f electron. To probe the unoccupied states of Yb, we measured the excitation of electrons from O 1s states to O 2p states (O K edge) using an X-ray. Nominally, O 2p states are fully occupied; the O 1s to O 2p excitation is forbidden by the Pauli exclusion principle. If, on the other hand, the O 2p states are hybridized with the Yb states, the O 2p states will be slightly unoccupied and give rise to observable O 1s to O 2p excitation; one can infer the energy of the unoccupied Yb states using the excitation energies. As shown in figure 4.15(a), with linearly polarized X-rays, several features can be observed in the absorption spectra. Previously, we carried out symmetry analysis of the absorption spectra measured on h-$LuFeO_3$ and identified the origin of these features mainly as the 5d orbitals, split in the crystal field: e^{π}, a^1, and e^{σ} [see figure 4.15(b)]. Compared with the X-ray absorption spectra of h-$LuFeO_3$, the spectra of h-$YbFeO_3$ showadditional density of states, as indicated in figure 4.15(a), which is expected to be the unoccupied 4f state that is hybridized with the O 2p states.

The $4f^{13}$ configuration of Yb can also be probed by measuring the excitation directly to the unoccupied 4f states (in the absence of $s-f$ hybridization, none exist with Lu^{3+}). As shown in figure 4.16(a), X-ray absorption spectra at the Yb M edge were measured at 18 K. Two peaks are observed in the absorption spectra at approximately 1513 and 1555 eV,which can be assigned to M_5 (initial state $3d_{5/2}$) and M_4 (initial state $3d_{3/2}$) excitations, respectively, according to the photon energy [24] [see figure 4.16(b)]. The M_5 transition in Yb, which is allowed by the angular-momentum selection rule, can be described using the one-electron (hole) picture, without many-body interactions, due to the simple initial (full $3d_{5/2}$, one hole in $4f_{7/2}$) and final (one hole in $3d_{5/2}$, full $4f_{7/2}$) states, consistent

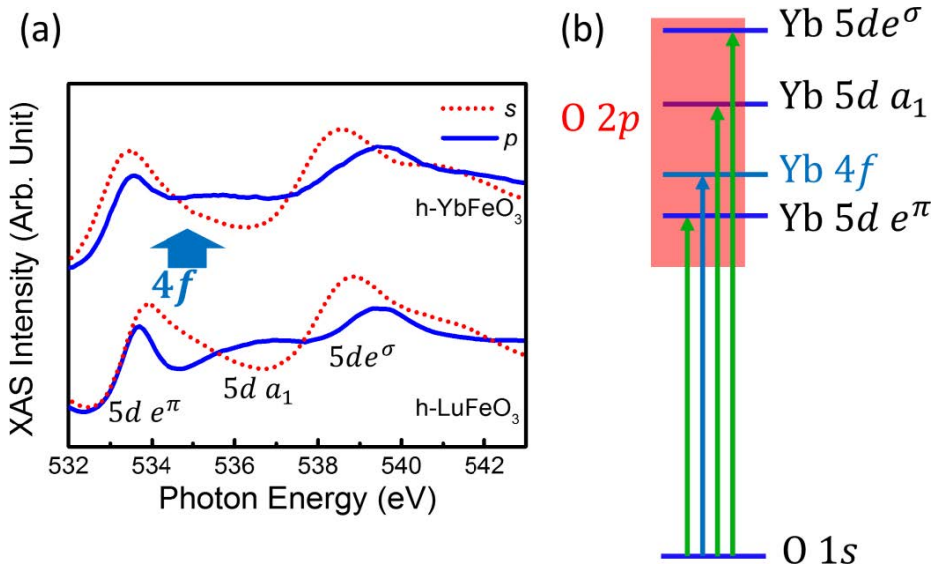

Figure 4.15: X-ray absorption spectra at the O K edge of h-$LuFeO_3$ and h-$YbFeO_3$, measured using linearly polarized X-rays. The arrow indicates the 4f state. (b) Schematic illustration of the O K edge excitation and the hybridization between the O and Yb states.

with the observed sharp, structureless peak in figure 4.16(a). The M_4 excitation ($3d_{3/2}$ to $4f_{7/2}$), on the other hand, is not allowed by the angular-momentum selection rule. The nonzero intensity of the M_4 peak suggests that the crystal-field splitting and the Yb 4f O 2p hybridization reduce the symmetry of the electronic states considerably, which is in line with the observed contribution to the O K edge excitation by the Yb 4f state shown in figure 4.15(a).

4.4.4 Magnetization of Yb and Fe

To study the magnetization of Yb, we carried out X-ray magnetic circular dichroism measurements by comparing the absorption spectra using a circularly polarized X-ray in opposite magnetic fields. As shown in figure 4.16(a), the X-ray absorption spectra measured in 19 kOe and -19 kOe magnetic fields along the z direction show a clear contrast. The XMCD contrast measured at H = 19 kOe, for various temperatures between 6.5 and 80 K, is displayed in figure 4.17(a). The value of the XMCD signal decreases rapidly at low temperature, inconsistent with typical ferromagnetic dependence, which typically follows

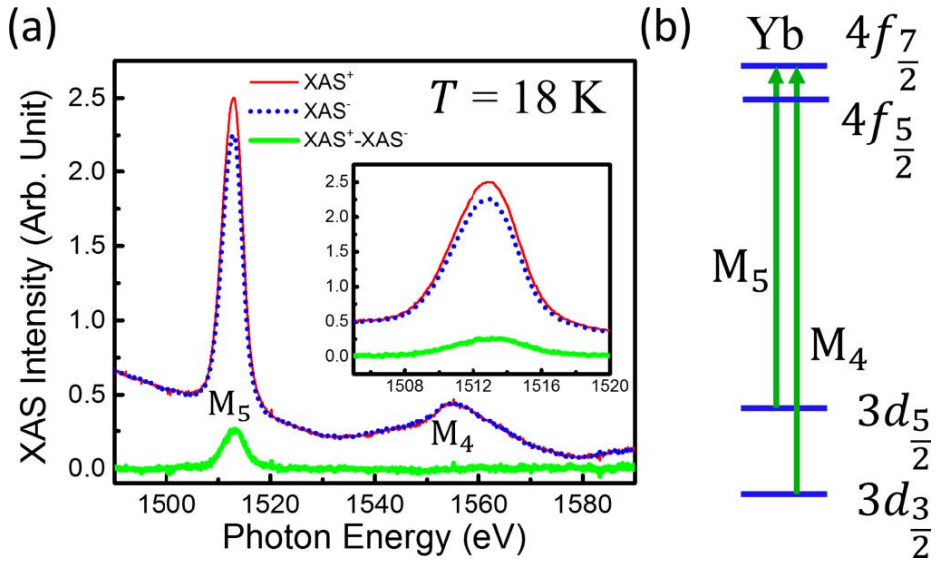

Figure 4.16: (a) X-ray absorption spectra at the Yb M edge, measured using an X-ray polarized counterclockwise. XAS^+ (XAS^-) is the spectrum measured in magnetic field along the $+z$ ($-z$) direction. (b) Schematic illustration of the Yb M edge excitation. The crystalline c axis of h-$YbFeO_3$ is along the z direction.

Blochs law (i.e., a slow decrease at low temperature but much faster close to the magnetic ordering temperature). Figure 4.17(b) shows the field dependence of the XMCD contrast of Yb at 18 K. A hysteresis is observed with a coercive field of approximately 3.5 kOe. The magnetization converted from the XMCD contrast is also displayed in figure 4.17.

Figure 4.18(a) shows the spectra of X-ray absorption of the Fe L edge measured in a circularly polarized X-ray in a 10 kOe magnetic field at 6.5 K. A clear difference is observed between the spectra measured using X-rays of different polarizations, which can be used to estimate the magnetization of Fe. Figure 4.18(b) shows the magnetic-field dependence of the Fe magnetization calculated from the XMCD contrast using the sum rule [25-27]. A hysteretic behavior is observed, with a coercive field of approximately 4 kOe, consistent with the value found in previous bulk magnetometry measurements [22, 23]. This coercive fields is also similar to that of Yb in figure 4.17(b), indicative of the exchange field on Yb generated by Fe. The saturation magnetization of Fe is 0.05 ± 0.01 μB/f.u., which corresponds to a small projection of the Fe moment along the c axis. From figure 4.17 and 4.18, we find that the magnetization of Fe is antiparallel to the magnetic field and to that of the

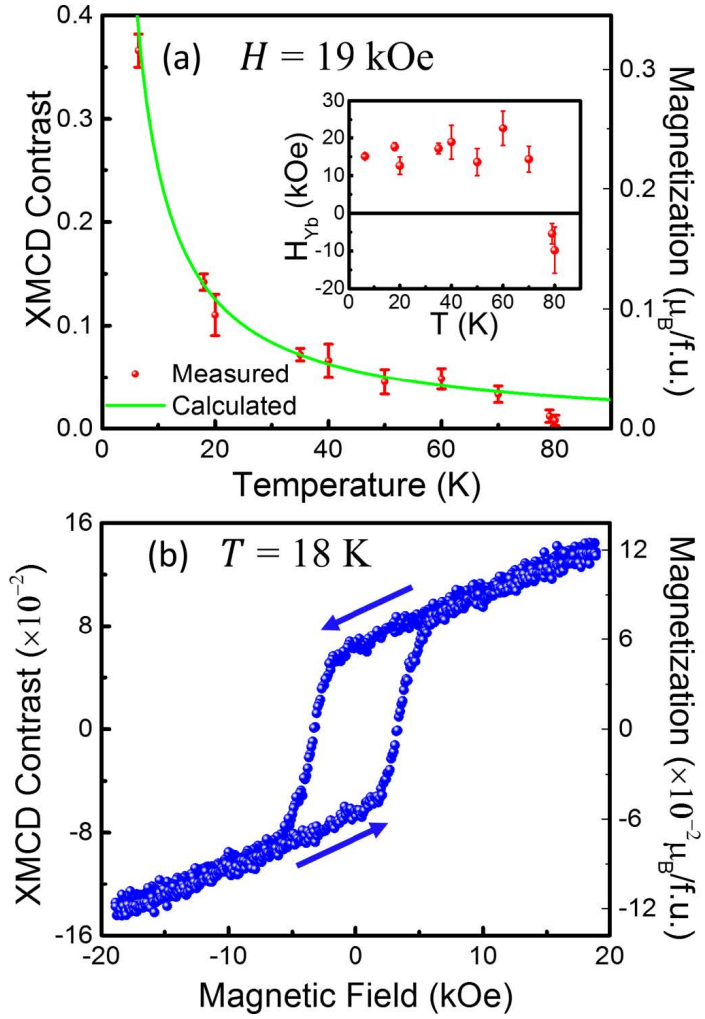

Figure 4.17: XMCD contrast at the Yb M_5 edge and the corresponding magnetization. (a) Temperature dependence measured in a 19 kOe magnetic field; the line is calculated using the parameters analyzed from (b). Inset: H_{Yb} extracted from the mean-field theory. (b) Magnetic-field dependence measured at 18 K. The magnetic field is along the *c* axis. Figure courtesy of Dr. Xiaoshan Xu's group.

Yb magnetization at low temperature. This provides a direct observation of ferrimagnetic order in h-$YbFeO_3$.

4.4.5 The possible mixed valence of Yb

A mixed valence (Yb^{3+} and Yb^{2+}) may play a role in the magnetism of h-$YbFeO_3$ as well as the determination of the magnetization on the Yb^{3+}. In principle, there is a tendency to form Yb^{2+} due to the stability of the $4f^{14}$ configuration. Although it will not affect

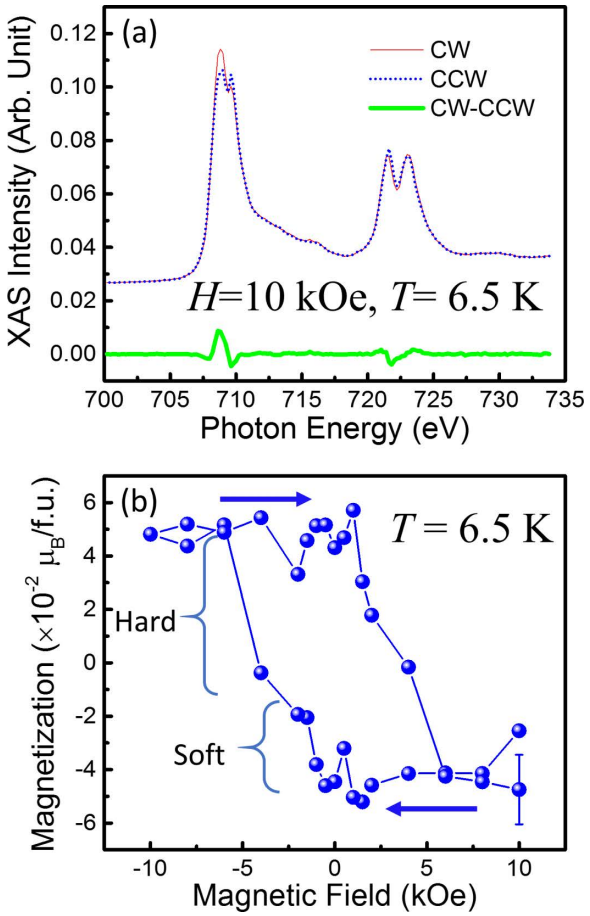

Figure 4.18: (a) Absorption spectra at the Fe L edge measured with circularly polarized X-rays in a 10 kOe field at 6.5 K. CW and CCW stand for clockwise and counterclockwise polarization of the X-rays, respectively. (b) Magnetic-field dependence of the magnetization of Fe at 6.5 K, which contains a soft and a hard component (see section 4.4.7). The magnetic field is along the *c* axis. Figure courtesy of Dr. Xiaoshan Xu's group.

the XMCD method discussed above since Yb^{2+} does not contribute to the Yb M_5 X-ray absorption in the first place (the excitations to the fully occupied 4f states are forbidden in Yb^{2+}), it will be important for bulk magnetometry. We investigated the possibility of a mixed valence in h-$YbFeO_3$ using ARXPS by probing the core-level electronic structure.

Figure 4.19(a) shows the Fe 2p X-ray photoemission spectra for both h-$LuFeO_3$ and h-$YbFeO_3$. The good match between the Fe $2p_{3/2}$ peaks of h-$LuFeO_3$ and h-$YbFeO_3$ in figure 4.19(a) indicates that Fe core-level electronic structures are similar in these two ferrites. Previously, we have studied the X-ray photoemission spectra of Fe 2p using the Gupta and Sen (GS) multiplet fitting of Fe$2p_{3/2}$ in h-$LuFeO_3$, and we concluded that the Fe

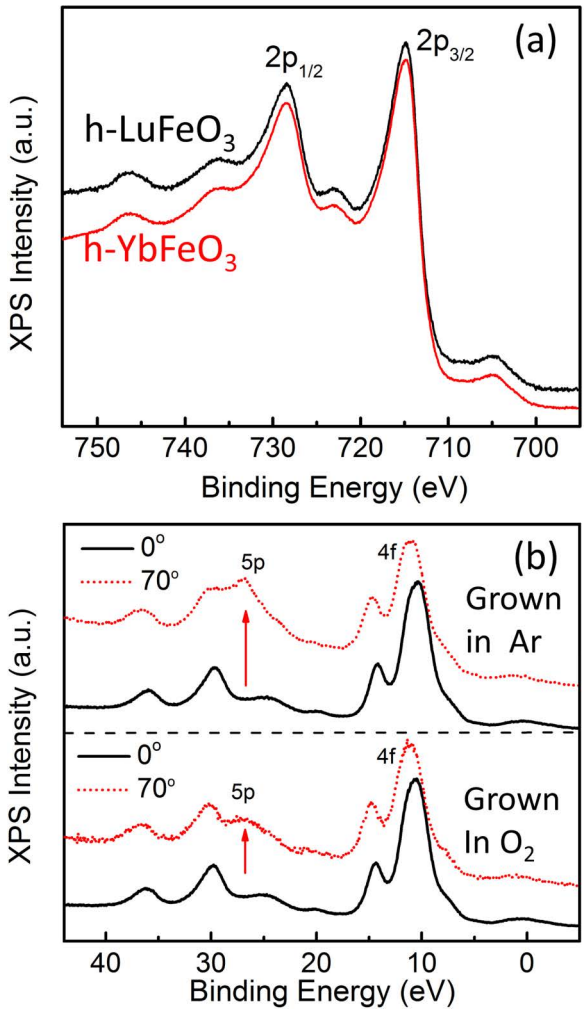

Figure 4.19: (a) X-ray photoelectron spectra around the Fe 2p core level for h-$YbFeO_3$ and h-$LuFeO_3$. (b) The X-ray photoelectron spectra around the Yb 5p edge of h-$YbFeO_3$ film samples grown in an Ar and an O_2 environment measured at 0° and 70° take-off angle, corresponding to 2 and 0.7 nm probing depth, respectively

2p and its satellite peaks are characteristic of a nominal Fe^{3+} valence as shown in section 4.1. The same analysis applies here in h-$YbFeO_3$ as well. These features also do not vary with emission angle (data not shown). As a result, both the surface and the bulk part of the h-$YbFeO_3$ are in the nominal Fe^{3+} valence state.

We also did not find any indication of Yb^{2+} in the film samples grown in an oxygen environment (used for X-ray-absorption spectroscopy and X-ray magnetic circular dichroism in figures 4.13-4.18). To investigate the possible appearance of Yb^{2+}, we studied ARXPS

on the h-$YbFeO_3$ films prepared in an argon environment. A comparison with two samples grown in oxygen and argon environments is displayed in figure 4.19(b). At the 0° takeoff angle (perpendicular to surface), the XPS spectra of Yb are identical for both h-$YbFeO_3$ samples. At the 70° takeoff angle, which probes mostly the surface [28, 29], the XPS spectra of the sample grown in an oxygen environment (lower panel) do not show a clear difference from that at 0°, and the surface appears to be slightly Yb-rich. In contrast, for the sample grown in the argon environment, the XPS spectra at the 70∘ takeoff angle exhibit additional intensity at the 5p peak, indicating a Yb^{2+} valence [30]. The correlation between the growth conditions indicates that the presence of oxygen vacancy promotes the reduction of Yb^{3+} at the surface. Although slightly YbO-rich, the mixed surface termination (both iron oxide and YbO appear present at the surface) differs from the FeO termination seen for $LuFeO_3$ as we discussed in section 4.1

4.4.6 Origin of reduced moment of Yb

The low-temperaturemagnetic moment of Yb is found to be 1.6 μB, a value significantly smaller than 4.5μB for a free Yb. In h-$YbFeO_3$, Yb is surrounded by seven oxygen atoms, approximately corresponding to C_{3v} symmetry. Analysis using double groups indicates that the $4f_{7/2}$ states are split by the crystal field into four levels: $3E_{1/2}$ + $E_{3/2}$, where $E_{1/2}$ and $E_{3/2}$ are both two-dimensional [31]. The energy scale of the crystal-field splitting is typically a few meV to a few tens meV, which cannot be resolved in the XAS spectra. This crystal-field splitting means that, at low temperature, only the low-lying level (ground state) is populated and contributes to the magnetization. The occupation of the low-lying level, in turn, leads to the reduced value of μ_{Yb}, and it is the reason for the temperature-dependent magnetic moments and magnetic anisotropy observed previously in rare-earth-containing oxides [32, 33].

4.4.7 Comparison between magnetic properties of h-$YbFeO_3$ and h-$LuFeO_3$

Hexagonal $LuFeO_3$ (h-$LuFeO_3$) is the most studied hexagonal rare-earth ferrite. Because Lu^{3+} is nonmagnetic, the magnetic properties of h-$LuFeO_3$ are less complex. By comparing h-$LuFeO_3$ and h-$YbFeO_3$, one may gain insight into the effect of the rare earth on the magnetism. One dramatic difference between h-$YbFeO_3$ and h-$LuFeO_3$ is in the coercive field of magnetization. For h-$YbFeO_3$ at 18 K, the coercive field is about 4 kOe, which is much smaller than the value 25 kOe for h-$LuFeO_3$ [8]. For both h-$LuFeO_3$ and h-$YbFeO_3$, the magnetization-field loops of Fe have a squared shape, suggesting that the magnetic coercive field is determined by the competition between the magnetic anisotropy energy and the Zeeman energy. Compared with h-$LuFeO_3$, h-$YbFeO_3$ has enhanced magnetization due to the contribution of Yb. Therefore, a much smaller magnetic field is needed in h-$YbFeO_3$ to overcome the magnetic anisotropy, corresponding to a much smaller coercive field. Another difference between h-$YbFeO_3$ and h-$LuFeO_3$ is in the saturation magnetization of Fe. According to figure 4.18, in h-$YbFeO_3$, $M_{Fe,S}$ = 0.05 $\pm$ 0.01 μB/f.u., larger than that in h-$LuFeO_3$ (0.03μB/f.u.) [8]. We note that previously it was observed in h-$LuFeO_3$ that the magnetization contains a soft component and a hard component, in which only the hard component (0.018 μB/f.u.) is believed to be intrinsic to the weak ferromagnetic ordering, because it disappears above the magnetic ordering temperature. In figure 4.18 there is also one soft (coercive field 1 kOe) and one hard component (coercive field 4 kOe). If we only treat the hard component to be intrinsic to the canting of the Fe moment, the weak ferromagnetic moment of Fe in h-$YbFeO_3$ is 0.03 $\pm$ 0.01 μB/Fe [figure 4.18(b)], to still larger compared with the value 0.018 μB/f.u. in h-$LuFeO_3$ [8]. Due to the size difference of Lu^{3+} and Yb^{3+} [2], the lattice constants of the basal plane of h-$LuFeO_3$ are smaller than that of h-$YbFeO_3$: a = 5.963 $\AA$ for h-$LuFeO_3$ and a = 6.021 $\AA$ for h-$YbFeO_3$ [33]. Our recentwork suggests that a compressive biaxial strain may reduce the canting of the Fe moments in

h-$YbFeO_3$ [34], which is in linewith the correlation between the lattice constant and the weak ferromagnetic moment on Fe observed here.

From the temperature and magnetic-field dependence of the Yb magnetization, we found that the low temperature Yb magnetic moment is significantly reduced compared with the value of free Yb^{3+} ions, indicating the effect of crystal field. The exchange field on Yb, generated by the Fe moments, tends to anti-align the magnetization of Fe and Yb at low temperature.

References

[1] Wang W, Zhao J, Wang W, Gai Z, Balke N, Chi M, Lee H N, Tian W, Zhu L, Cheng X, Keavney D J, Yi J, Ward T Z, Snijders P C, Christen H M, Wu W, Shen J and Xu X 2013 *Phys. Rev. Lett.* **110** 237601

[2] Xu X and Wang W B 2014 *Mod. Phys. Lett.* **B** 28 1430008

[3] Das H, Wysocki A L, Geng Y N, Wu W D and Fennie C J 2014 *Nature Commun.* **5** 2998

[4] Akbashev A R, Semisalova A S, Perov N S and Kaul A R 2011 *Appl. Phys. Lett.* **99** 122502

[5] Masuno A, Sakai S, Arai Y, Tomioka H, Otsubo F, Inoue H, Moriyoshi C, Kuroiwa Y and Yu J D 2009 *Ferroelectrics* **378** 169

[6] Wang W B et al 2012 *Appl. Phys. Lett.* **101** 241907

[7] Akbashev A R, Roddatis V V, Vasiliev A L, Lopatin S, Amelichev V A and Kaul A R 2012 *Sci. Rep.* **2** 672

[8] Moyer J A, Misra R, Mundy J A, Brooks C M, Heron J T, Muller D A, Schlom D G and Schiffer P 2014 *Appl. Phys. Lett. Mater.* **2** 012106

[9] Wang H W, Solovyev I V., Wang W, Wang X, Ryan P J, Keavney D J, Kim J-W, Ward T Z, Zhu L, Shen J, Cheng X M, He L, Xu X and Wu X 2014 *Phys. Rev. B* **90** 014436

[10] Pavlov V V, Akbashev A R, Kalashnikova A M, Rusakov V A, Kaul A R, Bayer M and Pisarev R V 2012 *J. Appl. Phys.* **111** 056105

[11] Grosvenor A P, Kobe B A, Biesinger M C and McIntyre N S 2004 *Surf. Interface Anal.* **36** 1564

[12] Coad J P and Cunningham J G 1974 *J. Electron Spectrosc. Relat. Phenom.* **3** 435

[13] Lin T C, Seshadri G and Kelber J A 1997 *Appl. Surf. Sci.* **119** 83

[14] Gupta R P and Sen S K 1974 *Phys. Rev. B* **10** 71

[15] Gupta R P and Sen S K 1975 *Phys. Rev. B* **12** 15

[16] Biesinger M C, Payne B P, Grosvenor A P, Lau L W M, Gerson A R and Smart R S 2011 *Appl. Surf. Sci.* **257** 2717

[17] Losovyj Ya B et al 2009 *J. Phys.: Condens. Matter* **21** 045602

[18] Pavarini E, Koch E, Anders F and Jarrell M 2012 *Correlated Electrons: From Models to Materials Lecture Notes of the Autumn School Correlated Electrons* (Julich: Forschungszentrum Jlich, Zentralbibliothek, Verl.)

[19] Cho D-Y et al 2007 *Phys. Rev. Lett.* **98** 217601

[20] Ko K-T, Noh H-J, Kim J-Y, Park B-G, Park J-H, Tanaka A, Kim S B, Zhang C L and Cheong S-W 2009 *Phys. Rev. Lett.* **103** 207202

[21] Harrison W A 1980 *Electronic Structure and the Properties of Solids: the Physics of the Chemical Bond* (San Francisco: Freeman)

[22] Iida H, Koizumi T, Uesu Y, Kohn K, Ikeda N, Mori S, Haumont R, Janolin P-E, Kiat J-M, Fukunaga M and Noda Y 2012 *Thin Films J. Phys. Soc. Japan* **81** 24719

[23] Jeong Y K, Lee J, Ahn S, Song S-W, Jang H M, Choi H and Scott J F 2012 *J. Am. Chem. Soc.* **134** 1450

[24] Bearden J A 1967 *Rev. Mod. Phys.* **39** 78

[25] Stohr J and Siegmann H C 2006 *Magnetism from fundamentals to nanoscale dynamics* (Berlin: Springer)

[26] Stohr J and Konig H 1995 *Phys. Rev. Lett.* **75** 374851

[27] Carra P, Thole B T, Altarelli M and Wang X 1993 *Phys. Rev. Lett.* **70** 694

[28] Tanuma S, Shiratori T, Kimura T, Goto K, Ichimura S and Powell C J 2005 *Surf. Interface Anal.* **37** 833

[29] Seah M P and Dench W A 1979 *Surf. Interface Anal.* **1** 2-11

[30] Ohno Y 2008 *J. Electron Spectros. Relat. Phenomena* **165** 1-4

[31] Dresselhaus M S, Dresselhaus G and Jorio A 2007 *Group theory application to the physics of condensed matter* (Berlin: Springer-Verlag)

[32] Xu X S, Brinzari T V., McGill S, Zhou H D, Wiebe C R and Musfeldt J L 2009 *Phys. Rev. Lett.* **103** 267402

[33] Zhang X, Yin Y, Yang S, Yang Z and Xu X 2017 *J. Phys. Condens. Matter* **29** 164001

[34] Sinha K, Zhang Y, Jiang X, Wang H, Wang X, Zhang X, Ryan P J, Kim J-W, Bowlan J, Yarotski D A, Li Y, DiChiara A D, Cheng X, Wu X and Xu X 2017 *Phys. Rev. B* **95** 94110

Selected Publications

1. **Shi Cao**, Zhiyong Xiao, Chun-Pui Kwan, Kai Zhang, Jonathan P. Bird, Lu Wang, Wai-Ning Mei, Xia Hong, and Peter A Dowben, "Moving towards the magnetoelectric graphene transistor", Accepted by *Applied Physics Letters* (2017)

2. **Shi Cao**, Mike Street, Junlei Wang, Jian Wang, Xiaozhe Zhang, Christian Binek and Peter A Dowben, "Magnetization at the interface of Cr_2O_3 and paramagnets with large stoner susceptibility", *Journal of Physics: Condensed Matter* **29** 10LT01 (2017)

3. **Shi Cao**, Kishan Sinha, Xin Zhang, Xiaozhe Zhang, Xiao Wang, Yuewei Yin, Alpha T. N'Diaye, Jian Wang, David J. Keavney, Tula R. Paudel, Yaohua Liu, Xuemei Cheng, Evgeny Y. Tsymbal, Peter A. Dowben, and Xiaoshan Xu, "Electronic structure and direct observation of ferrimagnetism in multiferroic hexagonal $YbFeO_3$", *Physical Review B* **95** 224428 (2017)

4. **Shi Cao**, Xiaozhe Zhang, Kishan Sinha, Wenbin Wang, Jian Wang, Peter A Dowben and Xiaoshan Xu, "Phase separation in $LuFeO_3$ films", *Applied Physics Letters* **108** 202903 (2016)

5. **Shi Cao**, Xiaozhe Zhang, Tula R Paudel, Kishan Sinha, Xiao Wang, Xuanyuan Jiang, Wenbin Wang, Stuart Brutsche, Jian Wang, Philip J Ryan, Jong-Woo Kim, Xuemei Cheng, Evgeny Y Tsymbal, Peter A Dowben and Xiaoshan Xu, "On the structural origin of the single-ion magnetic anisotropy in $LuFeO_3$", *Journal of Physics: Condensed Matter* **28** 156001 (2016)

6. **Shi Cao**, Xin Zhang, Takashi Komesu, Gong Chen, Andreas K Schmid, Lanping Yue, Iori Tanabe, William Echtenkamp, Yi Wang, Christian Binek and Peter A Dowben, "Low temperature growth of cobalt on Cr_2O_3(0001)", *Journal of Physics: Condensed Matter* **28** 046002 (2016)

7. **Shi Cao**, Ning Wu, William Echtenkamp, Valeria Lauter, Haile Ambaye, Takashi Komesu, Christian Binek and Peter A Dowben, "The surface stability of Cr_2O_3(0001)", *Journal of Physics: Condensed Matter* **27** 255003 (2015)

8. **Shi Cao**, Tula R Paudel, Kishan Sinha, Xuanyuan Jiang, Wenbin Wang, Evgeny Y Tsymbal, Xiaoshan Xu and Peter A Dowben, "The stability and surface termination of hexagonal $LuFeO_3$", *Journal of Physics: Condensed Matter* **27** 175004 (2015)

9. **Shi Cao**, Xin Zhang, Ning Wu, AT NDiaye, Gong Chen, Andreas K Schmid, Xumin Chen, W Echtenkamp, Axel Enders, Ch Binek and Peter A Dowben, "Spin polarization asymmetry at the surface of chromia", *New Journal of Physics* **16** 073021 (2014)

10. **Shi Cao**, Pan Liu, Jinke Tang, Haidong Lu, C-W Bark, Sangjin Ryu, Chang-Beom Eom, Alexei Gruverman and Peter A Dowben, "Magnetoelectric coupling at the EuO/$BaTiO_3$ interface" *Applied Physics Letters* **102** 172402 (2013)